CHALMERS
UNIVERSITY OF TECHNOLOGY

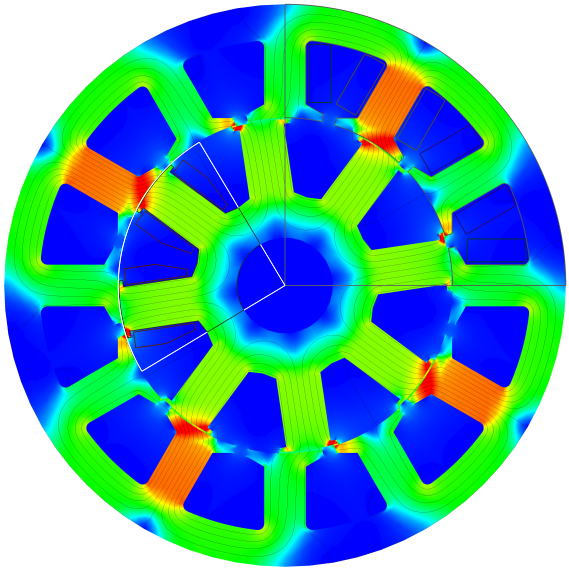

Design and Analysis of an Electrically Excited Synchronous Motor for a Compressor Application

A Performance and Cost Comparison of an Electrically Excited Synchronous Motor and a Permanent Magnet Synchronous Motor

Master's thesis in Sustainable electric power engineering and electromobility

Erik Olsson
Julia Björkman

DEPARTMENT OF ELECTRICAL ENGINEERING
CHALMERS UNIVERSITY OF TECHNOLOGY
Gothenburg, Sweden 2024
www.chalmers.se

Master's thesis 2024

Design and Analysis of an Electrically Excited Synchronous Motor for a Compressor Application

A Performance and Cost Comparison of an Electrically Excited Synchronous Motor and a Permanent Magnet Synchronous Motor

Erik Olsson
Julia Björkman

CHALMERS
UNIVERSITY OF TECHNOLOGY

Department of Electrical Engineering
Division of Electric Power Engineering
Chalmers University of Technology
Gothenburg, Sweden 2024

Design and Analysis of an Electrically Excited Synchronous Motor for a Compressor Application
A Performance and Cost Comparison of an Electrically Excited Synchronous Motor and a Permanent Magnet Synchronous Motor
ERIK OLSSON
JULIA BJÖRKMAN

Supervisor: David Deurell, Aros Electronics AB
Supervisor: Johan Åström, Aros Electronics AB
Examiner: Yujing Liu, Department of Electrical Engineering

Master's Thesis 2024
Department of Electrical Engineering
Division of Electric Power Engineering
Chalmers University of Technology
SE-412 96 Gothenburg
Telephone +46 31 772 1000

Cover: Magnetic flux density in the designed EESM at one time instant.

Typeset in LaTeX
Printed by Chalmers Reproservice
Gothenburg, Sweden 2024

Design and Analysis of an Electrically Excited Synchronous Motor for a Compressor Application
A Performance and Cost Comparison of an Electrically Excited Synchronous Motor and a Permanent Magnet Synchronous Motor
ERIK OLSSON
JULIA BJÖRKMAN
Department of Electrical Engineering
Chalmers University of Technology

Abstract

Permanent magnet synchronous motors (PMSMs) are commonly used motors. However, to reduce the usage of rare earth metals magnet-free motors are desirable. The electrically excited synchronous motor (EESM) utilizes field windings instead of magnets in the rotor and most research regarding EESMs has been focused on traction applications. This thesis investigates the possibility of using an EESM for an air compressor application that continuously operates in the constant torque region. The performance and cost of the designed EESM were compared to a reference PMSM.

A rotor for an EESM was designed and optimized to reach high continuous torque, using the finite element method to study electromagnetic and thermal properties. The stator used for the EESM was the same as for the reference PMSM. However, using only stator cooling the EESM had to be approximately 87 % longer than the reference PMSM to reach the nominal torque in continuous operation. It was shown that high continuous torque, without significant increases in stack length, requires more efficient rotor cooling techniques.

The currents in the EESM were optimized using a copper loss minimization algorithm. However, contrary to the reference PMSM, it was not possible to optimize the currents such that high continuous torque, maximum efficiency and high power factor were obtained simultaneously. Furthermore, the maximum efficiency of the long EESM during continuous operation in the nominal operating point was slightly more than 2.8 percentage points lower than for the reference PMSM. Regarding the material cost the price levels and the outer dimensions of the motors matter. However, it was shown that the eco cost is lower for an EESM than for a PMSM, even if it is substantially longer.

Overall, it was concluded that it is not feasible to use an EESM if the cooling method and outer dimensions have to be the same as for the reference PMSM. However, if the motor can be made a little longer, a slightly lower efficiency can be accepted and more efficient rotor cooling is implemented an EESM may be used as a more sustainable alternative to a PMSM for the investigated application.

Keywords: electrically excited synchronous motor, finite element method, copper loss minimization, electric machine design, constant torque region

Acknowledgements

We want to thank Aros Electronics for the opportunity to conduct this project and for the warm welcome we have received. We are especially grateful to our supervisors David Deurell and Johan Åström for supporting us throughout the project and always answering our questions.

We also want to thank Junfei Tang for taking the time to explain his work about EESMs. With his help, we implemented and used a version of the copper loss minimization algorithm he had developed in his work.

Finally, we would like to thank our examiner Yujing Liu for sharing his expertise about electric motors and guiding us through the project.

Erik Olsson and Julia Björkman, Gothenburg, May 2024

List of Abbrevations

DQ	Direct Quadrature
EESM	Electrically Excited Synchronous Motor
EMF	Electromotive Force
FEM	Finite Element Method
FSCW	Fractional Slot Concentrated Winding
GHG	Greenhouse Gas
GWP	Global Warming Potential
IM	Induction Motor
IPMSM	Interior mounted Permanent Magnet Synchronous Motor
LCM	Least Common Multiplier
LME	London Metal Exchange
MMF	Magnetomotive Force
MTPA	Maximum Torque Per Ampere
PF	Power Factor
PMSM	Permanent Magnet Synchronous Motor
REE	Rare Earth Elements
RMS	Root Mean Square
RPM	Revolutions Per Minute
SM	Synchronous Motor
SMM	Shanghai Metal Market
SPMSM	Surface mounted Permanent Magnet Synchronous Motor
synRM	Synchronous Reluctance Motor
THD	Total Harmonic Distortion

Nomenclature

A	Area
B	Magnetic flux density
$\mathcal{E}$	Electromotive Force
d	Direct-axis (d-axis)
f	Frequency
F	Magnetomotive Force
H	Magnetic field
I, i	Current
J	Inertia
k	Thermal conductivity, Fill factor, Range parameter in iterative algorithm
L	Inductance, Length
m	Number of phases
N	Number of turns in a coil
p	Active power, Number of pole pairs
q	Reactive power, Number of slots per pole per phase, Quadrature-axis (q-axis)
Q	Number of stator slots
R	Resistance
$\mathcal{R}$	Reluctance
s	Apparent power
T	Torque, Temperature
U, u	Voltage
α	Temperature coefficient
ϵ	Error in iterative algorithm
ρ	Resistivity
η	Efficiency

θ	Electrical degree, Current angle
Θ	Mechanical degree
Φ	Magnetic flux
Ψ	Magnetic flux linkage
ω	Electrical speed
Ω	Mechanical speed

Contents

1

Introduction

In today's electrified society, electrical machines are found almost everywhere. In electric vehicles there are several different kinds of electric motors; the main traction motor that drives the car and several auxiliary electric motors that power secondary systems of the vehicle such as water cooling pumps, air compressors and steering servos. Commonly, much research is conducted on traction motors. However, to ensure an environmentally sustainable and cost-effective production and usage of electric vehicles it is of importance to also investigate different alternatives for the auxiliary motors.

To achieve high efficiency, high power density, high torque to current ratio and low noise emissions permanent magnet synchronous motors (PMSMs) are commonly used [1]. However, high power density PMSMs have permanent magnets in the rotor that contain rare earth elements (REE). The production of electric motors would be more environmentally sustainable, cheaper and supply security could be achieved if REEs could be avoided. Hence, in this thesis the possibility to introduce an alternative auxiliary electric motor without permanent magnets will be investigated.

1.1 Background

The permanent magnets in a PMSM can either be placed inside the rotor core, called an interior mounted PMSM (IPMSM), or on the surface of the rotor, called surface mounted PMSM (SPMSM). These magnets create a constant magnetic field which is an important part of creating the torque. To achieve a high power density REEs, especially Neodymium Iron Boron (NdFeB), are often used in the permanent magnets [2], [3], [4]. However, even though REEs may offer some advantages when it comes to performance there are several downsides with using them in an electric machine. High cost is one disadvantage, NdFeB magnets account for approximately 70 % of the material cost in a PMSM [5]. Moreover, the production of REEs is highly concentrated to one country, China, which was responsible for 90 % of the global production of rare earth metals in 2019 [6]. This results in that the prices of permanent magnets are strongly affected by market fluctuations and policy changes in China [6]. REEs also impact the environment negatively. The NdFeB magnets account for approximately 5 % of the mass of the motor, yet they contribute to approximately 25 % of the greenhouse gas emissions that are related to the materials in a PMSM [3]. A large quantity of waste is also produced. According to [7] 2000

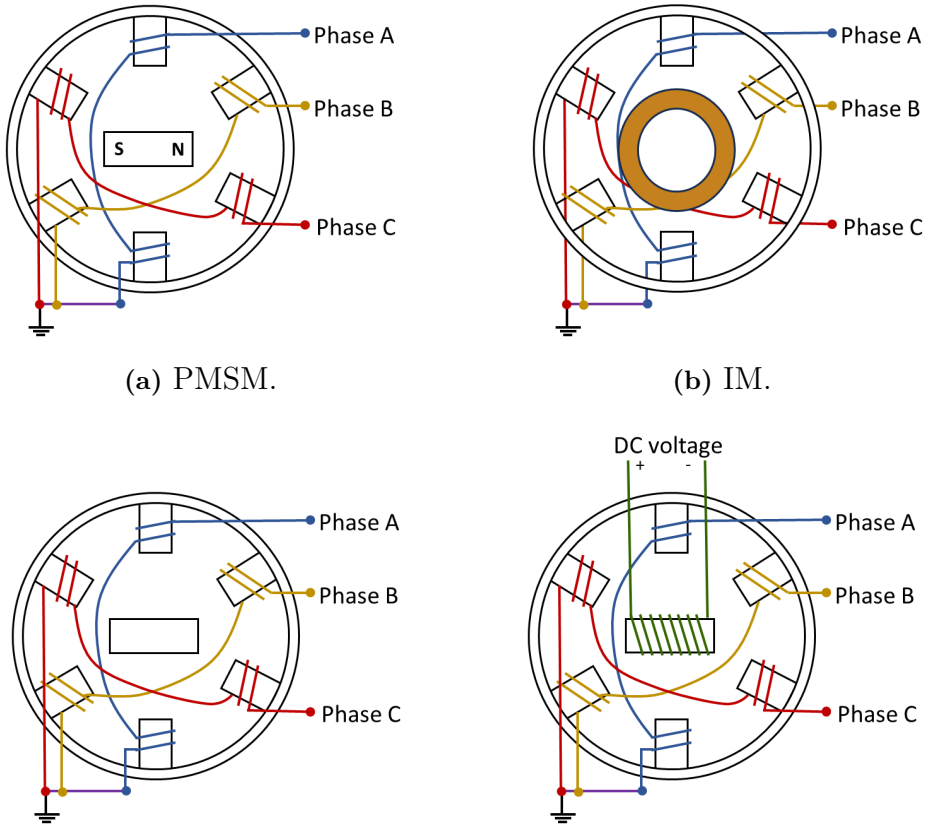

(a) PMSM. **(b)** IM.

(c) synRM. **(d)** EESM.

Figure 1.1: Illustration of PMSM, IM, synRM and EESM.

tonnes of solid waste are produced in order to get 1 tonne of rare earth metals.

To improve the environmental impact, the cost and the supply security there has been a trend to develop electric motors without any REEs [2]. Common magnet-free motors are the induction motor (IM), the synchronous reluctance motor (synRM) and the electrically excited synchronous motor (EESM) [3], illustrated together with the PMSM in Figure 1.1.

An IM has a cage consisting of aluminum or copper in the rotor [8]. The rotating magnetic field from the stator induces a current in the cage and the interaction between the two magnetic fields creates a torque [3], [8]. IMs are simple, cheap and robust motors [8]. However, there are also a few disadvantages, such as low efficiency, difficulty in controlling at low speeds and low power factor when the load is light [8]. SynRM is a synchronous motor with a salient rotor [3]. However, drawbacks of synRMs are that they have lower torque density, lower efficiency and lower power factor compared to a PMSM [8]. Hence, neither IMs nor synRMs are considered suitable REE-free alternatives to a PMSM.

EESM has field windings in the rotor that are powered with DC current [2], [4].

There are several ways to transfer energy to the windings in the rotor. One option is to utilize mechanical slip rings, which use carbon brushes to conduct current to the rotor field windings [9]. However, the slip rings result in friction losses and they require some maintenance and this technique is therefore not ideal [2], [9]. To eliminate the need for slip rings inductive transfer or capacitive transfer can be used [2], [9]. Out of these two, inductive transfer has received more research attention, and several studies have confirmed that inductive transfer is feasible to use in EESMs [2], [10], [11]. The possibility of avoiding slip rings makes EESMs more attractive [12].

EESMs also have the advantage of an additional operation freedom since it is possible to control the rotor flux by changing the field current [2], [4], [12]. By injecting a high field current for a short period of time a high peak torque can be reached [12]. The field current can also be tuned to achieve a high power factor, which results in a higher efficiency of the stator inverter [2], [4], [12]. Moreover, core losses can be minimized for low torques by reducing the magnetization [13]. Compared to PMSMs, EESMs are also better at handling fault conditions since it is possible to remove the induced electromotive force in the stator by turning off the field current [2]. Thus, overvoltages that are harmful to the inverter and insulation can be avoided. Furthermore, for motors operating in the field weakening region, such as traction motors, it is possible to achieve higher efficiency with an EESM compared to a PMSM at high speeds [4]

However, there are also a few challenges with using EESMs. One is that the copper windings may take up more space compared to NdFeB magnets. If the current density is assumed to be $10\,\mathrm{A/mm^2}$ a coil may have approximately five times larger cross-sectional area compared to an equivalent NdFeB magnet [3]. Another challenge is the copper losses in the rotor. This may affect the efficiency negatively in operating points where the field current is high compared to the output power [14]. Moreover, heat will be generated in the copper windings and cooling might be a problem [2], [4], [12].

The characteristics of an EESM make it suitable for traction applications and this has been the focus of much research about EESMs [2], [4], [12], [13], [14]. However, few investigations have been done on using EESMs as auxiliary motors that mostly operate in the constant torque region. In this thesis, the potential of using an EESM for the application of an air compressor used in buses will be investigated. The motor operates in the constant torque region and it should be designed for continuous operation.

1.2 Aim and Research Questions

This study aims to investigate the possibility of using an EESM for an air compressor application. To carry out this investigation a rotor for the EESM will be designed and the characteristics and the performance in the constant torque region will be evaluated using the finite element method (FEM). Both electromagnetic and thermal properties will be studied through these simulations. A reference IPMSM will be

used for comparison.

To find the advantages and challenges of using an EESM instead of a PMSM for an application that operates continuously in the constant torque region this thesis aims to study the following questions:

- How does the geometry of the rotor of an EESM affect the continuous torque? Can the EESM achieve the same continuous torque density as the PMSM using the same cooling method?
- How do the characteristics and the performance of an EESM compare to those of a PMSM in the constant torque region? Is it possible to achieve comparable efficiency and power factor with an EESM and a PMSM? Is it possible to achieve a lower torque ripple with an EESM?
- How do the material and environmental costs of an EESM compare to those of a PMSM?
- What cooling methods should preferably be used for an EESM?

1.3 Limitations

Due to limited time and resources a few limitations had to be set. The limitations are listed below.

- Not all parts of the EESM will be investigated. Energy transfer to the field windings and the corresponding power electronics will not be investigated. Neither will machine control be included in the study. It is considered more important to first develop the rotor; without a rotor, there is no use for an energy transfer system or a control algorithm.
- The results of the study will be limited to the results from the FEM simulations, no real machine will be built. Contrary to simulations, building a new rotor will take quite a lot of time and resources. Since this is a pilot study, it is considered more informative to use simulations.
- No new stator will be designed for the EESM, instead the same stator that is used for the PMSM will be utilized. The reason is that it is too time-consuming to design a completely new stator for the EESM.
- The stator currents used for the electromagnetic FEM simulation will be pure sinusoidal and the field current will be pure DC. Thus, there will be less harmonics in the currents compared to a real motor. When calculating core losses and performing thermal simulations this will be compensated for. However, there will be no compensation for other quantities. This simplification is made for both the EESM and the PMSM. Hence, the comparison of the two motors is rather fair.

2

Theory for EESMs and PMSMs

In this chapter theory about EESMs and PMSMs is described. To begin with, some fundamental electromagnetic theory and the working principle of EESMs and PMSMs are explained. Then mathematical models for the two motors are presented. Finally, information about the operating region, winding arrangements, losses and thermal modeling is presented.

2.1 Electromagnetic Theory

To understand the working principle of an electric motor some fundamental electromagnetic theory needs to be described. The generation of magnetic fields is essential. Amperes law in integral form in equation (2.1) describes how an electric current I in a winding with N turns will generate a magnetic field $\boldsymbol{H}$ in a closed path C around the winding [15]. The parameter F is the generated magnetomotive force (MMF).

$$\oint_{\mathrm{C}} \boldsymbol{H}\, dl = NI = F \tag{2.1}$$

Furthermore, the magnetic field $\boldsymbol{H}$ is related to the magnetic flux density $\boldsymbol{B}$ by $\boldsymbol{B} = \mu_0\mu_{\mathrm{r}}\boldsymbol{H} = \mu\boldsymbol{H}$ [15]. Here, μ_0 is the permeability in vacuum and μ_{r} is the relative permeability. Different types of materials have different values of μ_{r} and a high value indicates that the material has a higher tendency to align its magnetic dipole moments with an externally applied magnetic field [15]. Ferromagnetic materials, such as iron, have $\mu_{\mathrm{r}} \gg 1$ and the value is not a constant; it depends on the magnitude of $\boldsymbol{H}$ as well as the history of the material's magnetization [15]. This will be described further in section 2.7.2.1. The total magnetic flux Φ through a surface S can be calculated from equation (2.2) [15].

$$\Phi = \int_{\mathrm{S}} \boldsymbol{B} \cdot d\boldsymbol{s} \tag{2.2}$$

In a magnetic circuit the relation between MMF and flux is described in equation (2.3), where $\mathcal{R}$ is the reluctance [15]. Reluctance in a magnetic circuit is equivalent to resistance in an electric circuit.

$$F = \Phi\mathcal{R}, \tag{2.3}$$

A varying magnetic flux induces an electromotive force (EMF) $\mathcal{E}$ in a coil with N turns according to Faraday's law of electromagnetic induction in equation (2.4) [15], [16], [17], [18]. Here, $\Psi = N\Phi$ is the flux linkage. A negative sign is used since the current corresponding to the induced EMF produces a magnetic field in the opposite direction of the initial field [17]. Because of that the induced EMF is sometimes called back EMF [18].

$$\mathcal{E} = -N\frac{d\Phi}{dt} = -\frac{d\Psi}{dt} \tag{2.4}$$

Flux linkage and current are used to calculate the apparent inductance L according to equation (2.5) [16], [17]. There is a difference between self inductance and mutual inductance. The inductance caused by flux that the coil has produced itself is the self inductance [16]. If the flux is created by another coil the inductance is a mutual inductance [16].

$$L = \frac{\Psi}{I} \tag{2.5}$$

2.2 Working Principle of EESMs and PMSMs

Both EESMs and PMSMs are synchronous machines (SMs), meaning that the rotor rotates with the same speed as the rotating magnetic field caused by the currents in the stator windings. This principle will be further described in this section.

An SM can have one or more pair of poles p [16]. For electromagnetic calculations of an SM electrical angles, which describe the electrical position, are often used instead of mechanical angles, which describe the rotation of the shaft [16]. For a machine with p pole pairs the relation between electrical degrees θ_{elec} and mechanical degrees Θ_{mech} is $\theta_{\text{elec}} = p\Theta_{\text{mech}}$ [16].

The stator windings are supplied with three-phase currents that can be described as in equation (2.6) [16], [19]. Here, $i_{\text{a}}(t)$, $i_{\text{b}}(t)$ and $i_{\text{c}}(t)$ are the phase currents and during normal operation they have approximately the same amplitude [19]. The electrical frequency of the phase currents is $f_1 = \omega_1/2\pi$.

$$\begin{aligned} i_{\text{a}}(t) &= I_{\text{a}}\cos(\omega_1 t) \\ i_{\text{b}}(t) &= I_{\text{b}}\cos(\omega_1 t - 2\pi/3) \\ i_{\text{c}}(t) &= I_{\text{c}}\cos(\omega_1 t - 4\pi/3) \end{aligned} \tag{2.6}$$

Just as the phase currents, the produced MMF of each phase will also have approximately the same amplitude and be shifted 120° in time with respect to each other [16]. Moreover, the windings for the three phases are separated 120° electrical degrees in space [16]. The resulting expressions for the phase MMFs are shown in equation 2.7. Here F_{m} is the amplitude of the phase MMF and phase A is shifted from a reference axis by an angle ϕ [16].

$$\begin{aligned} F_{\mathrm{a}}(t,\phi) &= F_{\mathrm{m}}\cos(\omega_1 t)\cos(\phi) \\ F_{\mathrm{b}}(t,\phi) &= F_{\mathrm{m}}\cos(\omega_1 t - 2\pi/3)\cos(\phi - 2\pi/3) \\ F_{\mathrm{c}}(t,\phi) &= F_{\mathrm{m}}\cos(\omega_1 t - 4\pi/3)\cos(\phi - 4\pi/3) \end{aligned} \tag{2.7}$$

The total MMF can then be expressed as in equation (2.8) [16]. It is clear that the resulting MMF will rotate with a constant angular speed ω_1 electrical rad/s and has a sinusoidal spatial distribution [16]. However, it should be noted that harmonics have been ignored in this derivation.

$$F_{\mathrm{tot}}(t,\phi) = F_{\mathrm{a}}(t,\phi) + F_{\mathrm{b}}(t,\phi) + F_{\mathrm{c}}(t,\phi) = \frac{3}{2}F_{\mathrm{m}}\cos(\omega_1 t - \phi) \tag{2.8}$$

From the rotating MMF a rotating flux will be generated according to equation (2.3). During the operation of an EESM or a PMSM the poles in the rotor will lock in with the rotating magnetic field and the rotor will rotate along with it with an electrical angular speed of ω_{r}. For synchronous operation $\omega_{\mathrm{r}} = \omega_1$ [16]. If the stator quantities have the frequency $f = \omega_1/2\pi$ the mechanical speed of the rotor can be calculated as in equation (2.9) [16]. The unit of Ω_{mech} is revolutions per minute (rpm) if f is measured in Hertz (Hz).

$$\Omega_{\mathrm{mech}} = \frac{60f}{p} \tag{2.9}$$

2.3 Mathematical Models

2.3.1 DQ Coordinate System

To describe the electrical performance of SMs it is common to use the dq0 coordinates, with two rotating coordinate axes. These rotating coordinate axes are the d-axis and the q-axis, where the q-axis is leading the d-axis with 90 electrical degrees [16]. In this thesis the dq-frame rotates along with the rotor with a speed of ω_{r}. Furthermore, for analysis of electric machines it is common to set the d-axis such that it aligns with the main rotor flux [16], [19], this is also implemented in this thesis. The transformation from the abc-system to the dq0-system for the stator currents is shown in equation (2.10) and the inverse transformation is shown in equation (2.11) [16], [20], [21]. In this thesis the constant K is set to 2/3 to get amplitude-invariant scaling, meaning that the peak value of i_{d} and i_{q} are equal to the peak value of the stator currents [16]. The zero sequence current i_0 is connected to the symmetry of the three phases. For balanced conditions i_0 will be equal to 0 A since $i_{\mathrm{a}} + i_{\mathrm{b}} + i_{\mathrm{c}} = 0\,\mathrm{A}$ [16]. Furthermore, the angle θ_{r} is the time integral of the angular velocity ω_{r}. The transformations shown in equations (2.10) and (2.11) also apply to stator flux linkages and voltages.

$$\begin{bmatrix} i_\mathrm{d} \\ i_\mathrm{q} \\ i_0 \end{bmatrix} = K \begin{bmatrix} \cos(\theta_\mathrm{r}) & \cos(\theta_\mathrm{r} - \frac{2\pi}{3}) & \cos(\theta_\mathrm{r} - \frac{4\pi}{3}) \\ -\sin(\theta_\mathrm{r}) & -\sin(\theta_\mathrm{r} - \frac{2\pi}{3}) & -\sin(\theta_\mathrm{r} - \frac{4\pi}{3}) \\ \frac{1}{2} & \frac{1}{2} & \frac{1}{2} \end{bmatrix} \begin{bmatrix} i_\mathrm{a} \\ i_\mathrm{b} \\ i_\mathrm{c} \end{bmatrix} = T_{\mathrm{abc}\to\mathrm{dq0}} \begin{bmatrix} i_\mathrm{a} \\ i_\mathrm{b} \\ i_\mathrm{c} \end{bmatrix} \tag{2.10}$$

$$\begin{bmatrix} i_\mathrm{a} \\ i_\mathrm{b} \\ i_\mathrm{c} \end{bmatrix} = \frac{2}{3K} \begin{bmatrix} \cos(\theta_\mathrm{r}) & -\sin(\theta_\mathrm{r}) & 1 \\ \cos(\theta_\mathrm{r} - \frac{2\pi}{3}) & -\sin(\theta_\mathrm{r} - \frac{2\pi}{3}) & 1 \\ \cos(\theta_\mathrm{r} - \frac{4\pi}{3}) & -\sin(\theta_\mathrm{r} - \frac{4\pi}{3}) & 1 \end{bmatrix} \begin{bmatrix} i_\mathrm{d} \\ i_\mathrm{q} \\ i_0 \end{bmatrix} = T_{\mathrm{dq0}\to\mathrm{abc}} \begin{bmatrix} i_\mathrm{d} \\ i_\mathrm{q} \\ i_0 \end{bmatrix} \tag{2.11}$$

For synchronous operation ($\omega_\mathrm{r} = \omega_1$) in steady state i_d and i_q are constant and can be expressed in terms of the stator current amplitude I_s using the current angle θ as shown in equation (2.12) [16]. Also other quantities, such as inductances, are constant in the dq-frame.

$$\begin{aligned} i_\mathrm{d} &= I_\mathrm{s}\cos\theta \\ i_\mathrm{q} &= I_\mathrm{s}\sin\theta \end{aligned} \tag{2.12}$$

2.3.2 Mathematical Machine Model

To understand and analyze the performance of the EESM a mathematical model is needed. In this mathematical model the core losses are neglected and how to account for those will be described in Section 2.7.2. Furthermore, it should be noted that in the mathematical description of the motors lower-case letters i, u etc. are for instantaneous quantities and upper-case letters I, U etc. describe quantities in steady state. The DQ coordinate system is used for the mathematical model. As suggested in [2] a third axis, the f-axis, is introduced for the mathematical modeling of the EESM to take the quantities associated with the field windings in the rotor into account.

Important quantities for an EESM are the terminal voltages $\boldsymbol{u}$, the currents $\boldsymbol{i}$ and the flux linkages $\boldsymbol{\Psi}$, these are shown in equation (2.13) [2], [22]. These vectors contain information about the d-axis, q-axis and f-axis quantities. The direction of the d- and q-axes and the corresponding flux paths for an EESM are shown in Figure 2.1.

$$\boldsymbol{u} = \begin{bmatrix} u_\mathrm{d} \\ u_\mathrm{q} \\ u_\mathrm{f} \end{bmatrix}, \qquad \boldsymbol{i} = \begin{bmatrix} i_\mathrm{d} \\ i_\mathrm{q} \\ i_\mathrm{f} \end{bmatrix}, \qquad \boldsymbol{\Psi} = \begin{bmatrix} \Psi_\mathrm{d} \\ \Psi_\mathrm{q} \\ \Psi_\mathrm{f} \end{bmatrix} \tag{2.13}$$

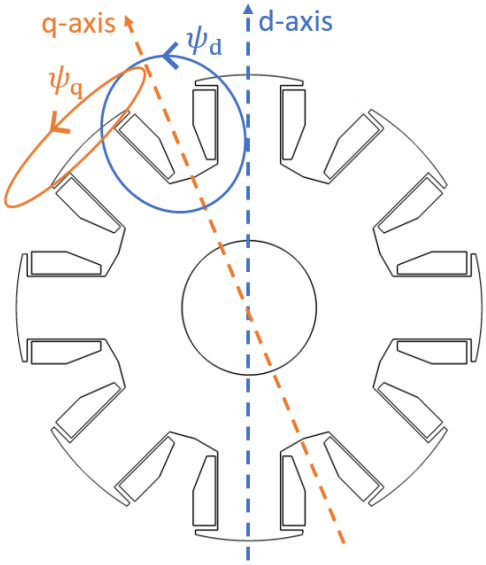

Figure 2.1: Direction of d-axis and q-axis and the corresponding flux paths for an EESM.

The terminal voltages can be calculated from equation (2.14) [2], [22].

$$\boldsymbol{u} = \boldsymbol{R}\boldsymbol{i} + \boldsymbol{\omega}\boldsymbol{\Psi} + \frac{d\boldsymbol{\Psi}}{dt} \tag{2.14}$$

The matrix $\boldsymbol{R}$ contains the per phase resistance of the stator windings R_s and the resistance of the field windings R_f. The resistance matrix is shown together with the speed matrix $\boldsymbol{\omega}$ in equation (2.15) [2], [22]. In the speed matrix ω_r is the angular velocity of the rotor [2].

$$\boldsymbol{R} = \begin{bmatrix} R_\mathrm{s} & 0 & 0 \\ 0 & R_\mathrm{s} & 0 \\ 0 & 0 & R_\mathrm{f} \end{bmatrix}, \qquad \boldsymbol{\omega} = \begin{bmatrix} 0 & -\omega_\mathrm{r} & 0 \\ \omega_\mathrm{r} & 0 & 0 \\ 0 & 0 & 0 \end{bmatrix} \tag{2.15}$$

In steady state the term $\dfrac{d\boldsymbol{\Psi}}{dt}$ is equal to zero and the terminal voltages can be calculated as in equation (2.16) [2].

$$\boldsymbol{U} = \begin{bmatrix} U_\mathrm{d} \\ U_\mathrm{q} \\ U_\mathrm{f} \end{bmatrix} = \begin{bmatrix} R_\mathrm{s} I_\mathrm{d} - \omega_\mathrm{r} \Psi_\mathrm{q} \\ R_\mathrm{s} I_\mathrm{q} + \omega_\mathrm{r} \Psi_\mathrm{d} \\ R_\mathrm{f} I_\mathrm{f} \end{bmatrix} \tag{2.16}$$

According to equation (2.5) the flux linkages can be calculated from the apparent inductances as $\boldsymbol{\Psi} = \boldsymbol{L}\boldsymbol{I}$. The inductance matrix $\boldsymbol{L}$ is shown in equation (2.17) and it contains the self inductances L_dd, L_qq and L_ff and the mutual inductances [2].

$$\boldsymbol{L} = \begin{bmatrix} L_{\mathrm{dd}} & L_{\mathrm{dq}} & L_{\mathrm{df}} \\ L_{\mathrm{qd}} & L_{\mathrm{qq}} & L_{\mathrm{qf}} \\ L_{\mathrm{fd}} & L_{\mathrm{fq}} & L_{\mathrm{ff}} \end{bmatrix} \tag{2.17}$$

Commonly, the mutual inductances between the d-axis and the q-axis are small compared to the other inductances; thus, these mutual inductances may be neglected and equation (2.18) can be obtained [2]. Here, the self inductances are renamed as L_{d}, L_{q} and L_{f} and the mutual inductances between the d-axis and the field winding are expressed in terms of a mutual inductance L_{m}. The factor 3/2 in $L_{\mathrm{fd}} = 3/2 L_{\mathrm{m}}$ comes from the amplitude-invariant dq0 transformation [2].

$$\boldsymbol{L} \approx \begin{bmatrix} L_{\mathrm{dd}} & 0 & L_{\mathrm{df}} \\ 0 & L_{\mathrm{qq}} & 0 \\ L_{\mathrm{fd}} & 0 & L_{\mathrm{ff}} \end{bmatrix} = \begin{bmatrix} L_{\mathrm{d}} & 0 & L_{\mathrm{m}} \\ 0 & L_{\mathrm{q}} & 0 \\ \frac{3}{2}L_{\mathrm{m}} & 0 & L_{\mathrm{f}} \end{bmatrix} \tag{2.18}$$

Equation (2.16) can then be rewritten as

$$\boldsymbol{U} = \begin{bmatrix} U_{\mathrm{d}} \\ U_{\mathrm{q}} \\ U_{\mathrm{f}} \end{bmatrix} = \begin{bmatrix} R_{\mathrm{s}} I_{\mathrm{d}} - \omega_{\mathrm{r}} L_{\mathrm{q}} I_{\mathrm{q}} \\ R_{\mathrm{s}} I_{\mathrm{q}} + \omega_{\mathrm{r}} L_{\mathrm{d}} I_{\mathrm{d}} + \omega_{\mathrm{r}} L_{\mathrm{m}} I_{\mathrm{f}} \\ R_{\mathrm{f}} I_{\mathrm{f}} \end{bmatrix} = \begin{bmatrix} R_{\mathrm{s}} I_{\mathrm{d}} - \omega_{\mathrm{r}} L_{\mathrm{q}} I_{\mathrm{q}} \\ R_{\mathrm{s}} I_{\mathrm{q}} + \omega_{\mathrm{r}} L_{\mathrm{d}} I_{\mathrm{d}} + \omega_{\mathrm{r}} \Psi_{\mathrm{RM}} \\ R_{\mathrm{f}} I_{\mathrm{f}} \end{bmatrix}. \tag{2.19}$$

Here, Ψ_{RM} is the part of the rotor flux that passes through the air gap [18]. For a PMSM Ψ_{RM} is the part of the flux from the permanent magnets that pass through the air gap [18]. Moreover, for a PMSM there is no field winding, then only the terminal voltages U_{d} and U_{q} are of interest.

2.3.3 Instantaneous Power and Electromagnetic Torque

The complex instantaneous apparent power $\boldsymbol{s}$ is calculated by multiplying the instantaneous voltage vector with the conjugate of the instantaneous current vector [23]. The real part of the apparent power is then the active power p and the imaginary part is the reactive power q [23]. The instantaneous stator apparent power $\boldsymbol{s_s}$ can be calculated as

$$\boldsymbol{s}_{\mathrm{s}} = \boldsymbol{u}_{\mathrm{s}} \cdot \boldsymbol{i}_{\mathrm{s}}{}^{*} = \frac{3}{2}(u_{\mathrm{d}} + j u_{\mathrm{q}})(i_{\mathrm{d}} - j i_{\mathrm{q}}) = \frac{3}{2}(u_{\mathrm{d}} i_{\mathrm{d}} + u_{\mathrm{q}} i_{\mathrm{q}}) + j\frac{3}{2}(u_{\mathrm{q}} i_{\mathrm{d}} - u_{\mathrm{d}} i_{\mathrm{q}}) = p_{\mathrm{s}} + j q_{\mathrm{s}}, \tag{2.20}$$

where the factor $\frac{3}{2}$ comes from the amplitude-invariant transformation [20]. Using equation (2.14) the active stator power can further be expressed as in equation (2.21) [18].

$$p_{\mathrm{s}} = \frac{3}{2} R_{\mathrm{s}}(i_{\mathrm{d}}^2 + i_{\mathrm{q}}^2) + \frac{3}{2}\left(i_{\mathrm{d}} \frac{d\Psi_{\mathrm{d}}}{dt} + i_{\mathrm{q}} \frac{d\Psi_{\mathrm{q}}}{dt}\right) + \frac{3}{2}\omega_{\mathrm{r}}(\Psi_{\mathrm{d}} i_{\mathrm{q}} - \Psi_{\mathrm{q}} i_{\mathrm{d}}) \tag{2.21}$$

The first term is the copper losses in the stator windings and these will be further explained in section 2.7.1 [18]. The second term accounts for the rate of change of the stored energy in the inductive coupling and it is equal to zero in steady state operation [18]. The third term is the power transferred across the air gap, caused by the interaction between stator currents and the induced EMFs in the stator windings [2], [18]. This power is called the electromagnetic power p_{em}. The electromagnetic torque is obtained by dividing the electromagnetic power with the mechanical speed Ω_{mech}: $T_{\mathrm{em}} = p_{\mathrm{em}}/\Omega_{\mathrm{mech}}$ [18]. Since the mechanical speed is equal to $\Omega_{\mathrm{mech}} = \omega_{\mathrm{r}}/p$ the torque can be expressed as in equation (2.22) [18].

$$T_{\mathrm{em}} = \frac{3p}{2}(\Psi_{\mathrm{d}} i_{\mathrm{q}} - \Psi_{\mathrm{q}} i_{\mathrm{d}}) \tag{2.22}$$

Using that $\Psi_{\mathrm{d}} = L_{\mathrm{d}} I_{\mathrm{d}} + \Psi_{\mathrm{RM}}$ and $\Psi_{\mathrm{q}} = L_{\mathrm{q}} I_{\mathrm{q}}$ the electromagnetic torque can be calculated as shown in equation (2.23).

$$T_{\mathrm{em}} = \frac{3p}{2}(\Psi_{\mathrm{RM}} i_{\mathrm{q}} + (L_{\mathrm{d}} - L_{\mathrm{q}}) i_{\mathrm{d}} i_{\mathrm{q}}) \tag{2.23}$$

Here, the flux generated in the rotor creates the part of the torque that contains the term Ψ_{RM}. Differences in the reluctance of the d-axis and q-axis will generate a reluctance torque, which is the part of the torque that contains the term $L_{\mathrm{d}} - L_{\mathrm{q}}$ [19].

The relation between the electromagnetic torque T_{em} and the mechanical torque T_{m} can be described using the swing equation, shown in equation (2.24) [16]. Here, J is the moment of inertia and Ω_{mech} is the mechanical angular velocity of the rotor as before. For motor operation negative values for T_{em} and T_{m} should be used [16].

$$J\frac{d\Omega_{\mathrm{mech}}}{dt} = T_{\mathrm{m}} - T_{\mathrm{em}} \tag{2.24}$$

2.4 Operating Region

Electric motors that have different applications also have different operating points. However, in this section the entire operating region for an EESM and a PMSM will be described to get a clear picture of how the motors operate. In Section 3.1 the operating region of the designed motor will be explained further.

2.4.1 Current and Voltage Limits

The torque and power output of an EESM and a PMSM is limited by the maximum stator current amplitude $I_{\mathrm{s,max}}$ and the maximum stator voltage amplitude $U_{\mathrm{s,max}}$. The current limit can be described as

$$i_{\mathrm{d}}^2 + i_{\mathrm{q}}^2 \leq I_{\mathrm{s,max}}^2, \tag{2.25}$$

which is equivalent to a circle with radius $I_{\mathrm{s,max}}$ in the dq-plane [2], [24].

The voltage limit is

$$u_{\mathrm{d}}^2 + u_{\mathrm{q}}^2 \leq U_{\mathrm{s,max}}^2. \tag{2.26}$$

For steady state operation, the voltage limit is equivalent to equation (2.27) if the resistive voltage drops are neglected [2], [24].

$$(\omega_{\mathrm{r}} L_{\mathrm{q}} I_{\mathrm{q}})^2 + (\omega_{\mathrm{r}} L_{\mathrm{d}} I_{\mathrm{d}} + \omega_{\mathrm{r}} \Psi_{\mathrm{RM}})^2 \leq U_{\mathrm{s,max}}^2 \tag{2.27}$$

The voltage limit is an ellipse in the dq-plane the corresponding equation is shown in equation (2.28) [2]. The center of the ellipse is at $I_{\mathrm{d}} = I_{\mathrm{center}}$ and $I_{\mathrm{q}} = 0$. The semi-axes are a and b.

$$\frac{(I_{\mathrm{d}} - I_{\mathrm{center}})^2}{a^2} + \frac{I_{\mathrm{q}}^2}{b^2} \leq 1, \qquad I_{\mathrm{center}} = -\frac{\Psi_{\mathrm{RM}}}{L_{\mathrm{d}}}, \qquad a = \frac{U_{\mathrm{s,max}}}{\omega_{\mathrm{r}} L_{\mathrm{d}}}, \qquad b = \frac{U_{\mathrm{s,max}}}{\omega_{\mathrm{r}} L_{\mathrm{q}}} \tag{2.28}$$

The current limit circle and the voltage limit ellipse for an EESM are shown in Figure 2.2. Note that the radius of the circle is equal to the maximum stator current $I_{\mathrm{s,max}}$. The voltage limit ellipse will move towards the left when the field current increases and it will shrink towards the center when the speed increases [2]. This voltage limit ellipse is plotted for $L_{\mathrm{d}} > L_{\mathrm{q}}$, for $L_{\mathrm{q}} > L_{\mathrm{d}}$ the ellipse would have the d-axis as the major axis.

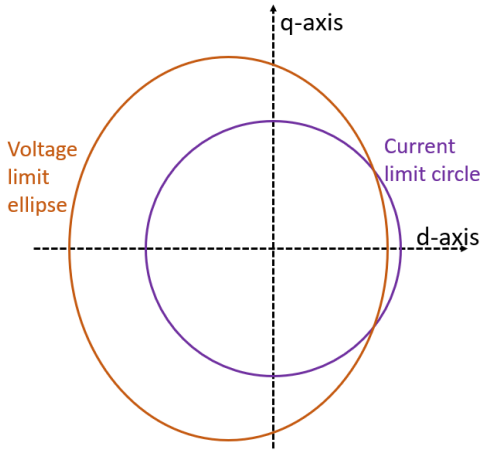

Figure 2.2: Current limit circle and voltage limit ellipse in the dq-plane for an EESM with $L_{\mathrm{d}} > L_{\mathrm{q}}$.

2.4.2 Torque-Speed Curve

Figure 2.3 shows the entire operating region of an EESM or a PMSM. Often the operating region is divided into two speed regions; below the base speed ω_{base} is the constant torque region and above ω_{base} is the flux-weakening region [24].

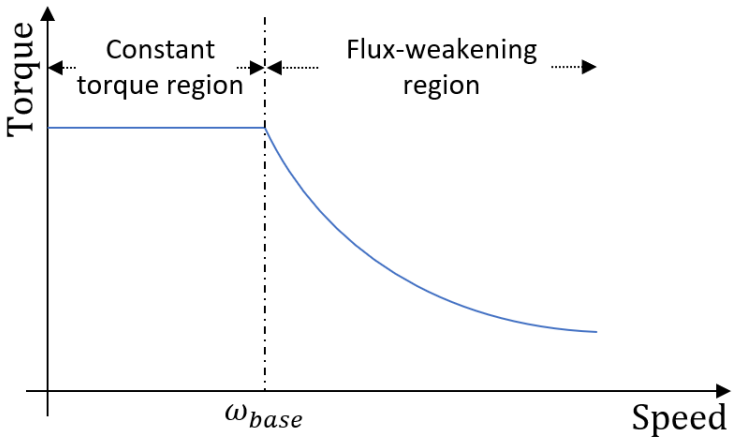

Figure 2.3: Torque-speed curve.

In the constant torque region, the stator voltage is below $U_{\text{s,max}}$ and the torque output is limited by $I_{\text{s,max}}$ [24]. To get the maximum torque, given a constant flux Ψ_{RM} from the rotor, maximum torque per ampere (MTPA) can be used to determine the current angle θ in the dq-frame according to equation (2.29) [2], [24].

$$\cos(\theta) = \frac{-\Psi_{\text{RM}} + \sqrt{\Psi_{\text{RM}}^2 + 8(L_{\text{d}} - L_{\text{q}})^2 I_{\text{s}}^2}}{4(L_{\text{d}} - L_{\text{q}})I_{\text{s}}} \tag{2.29}$$

When the speed increases the voltage limit ellipse shrinks. At the base speed ω_{base} the operating point is the intersection point between the current limit circle and the voltage limit ellipse [2], [24]. If the speed increases further the motor operates in the flux-weakening region. Here, the operating point is still the intersection point of the current limit circle and the voltage limit ellipse, which moves in a counter-clockwise direction in the dq-plane [2], [24]. This is called constant power operation [24]. In the case of the center of the voltage limit ellipse being inside the current limit circle, the stator current will have to decrease from $I_{\text{s,max}}$ for very high speeds [24].

2.4.3 Power Factor

Power factor, PF, is defined as

$$PF = \frac{p}{s}, \tag{2.30}$$

where p is the active power and s is the apparent power [23]. For an EESM it is possible to change the power factor by adjusting the field current [2]. High power factor results in a high efficiency of the stator inverter since there will be lower losses in the switches [22]. Moreover, for high speeds, the torque can be maximized by setting the power factor to unity and operate at peak active power [2].

2.5 Stator Winding Arrangements

For a three-phase electric machine there are multiple ways to arrange the stator windings and the stator slots. Common types of winding arrangements in three-phase PMSMs are overlapping distributed windings, overlapping concentrated windings and nonoverlapping concentrated windings, which could be either single layer or double layer [25]. Illustrations of these types of winding arrangements are shown in Figure 2.4. Nonoverlapping concentrated winding is called fractional-slot concentrated winding (FSCW) [25], and this type of winding arrangement will be of focus in this thesis. From Figures 2.4c and 2.4d it can be seen that when FSCW is used all turns in one stator coil are wound around one stator tooth.

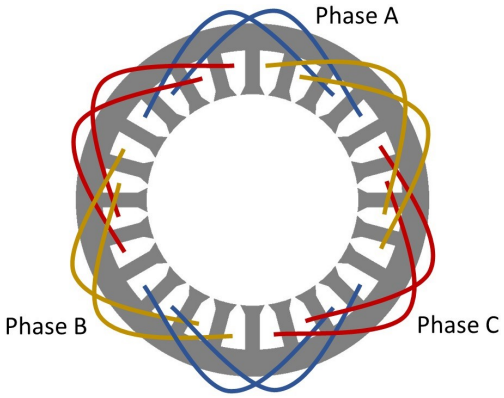

(a) Overlapping distributed winding.

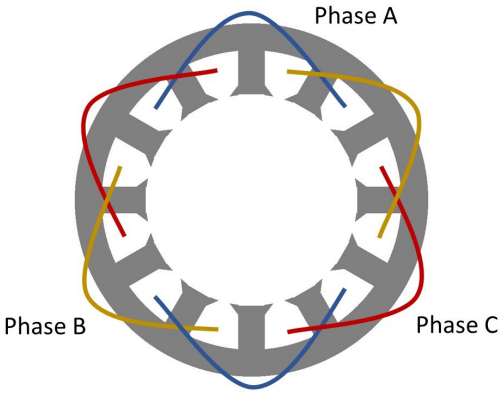

(b) Overlapping concentrated winding.

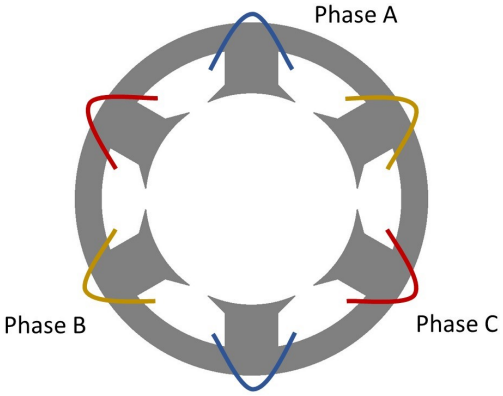

(c) Double layer nonoverlapping concentrated winding.

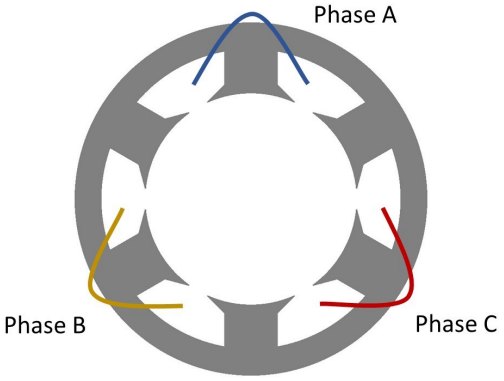

(d) Single layer nonoverlapping concentrated winding.

Figure 2.4: Illustration of different stator windings for a motor with 2 pole pairs.

2.5.1 Fractional-Slot Concentrated Winding

In general, FSCW provides higher torque density compared to other winding configurations and this is because the stator slot fill factor is high and the end windings are short [26]. To have short end windings is advantageous for short motors with a

radial flux [26], which are characteristics of the motors investigated in this thesis. However, the MMF waveforms generated by FSCW usually have a higher harmonic content compared to MMF waveforms generated by distributed windings [25]. These harmonics can be both sub- (lower than fundamental frequency) and super- (higher than fundamental frequency) harmonics and they might cause large rotor core losses. [26].

When implementing FSCW in an electric machine there are some important aspects to consider. The number of slots per pole per phase q can be calculated as

$$q = \frac{Q}{2mp}, \tag{2.31}$$

where Q is the number of stator slots, p is the number of pole pairs and m is the number of phases [26], [27]. For a machine with FSCW the value of q is smaller than one ($q < 1$), and most commonly $\frac{1}{4} \leq q \leq \frac{1}{2}$ [26]. It should be noted that for a FSCW machine with $q = \frac{1}{2}$ the torque-producing harmonic component is also the fundamental component, all other values of q result in MMF subharmonics [25], [26].

The selected combination of Q and p also affects the winding factor of the torque-producing harmonic component. This winding factor is proportional to the generated torque; therefore, it is beneficial if its value is high [27]. According to [26] the winding factor of the torque-producing harmonic component should be higher than 0.85.

Moreover, the combination of Q and p influences the periodicity of the machine. Periodicity is calculated as the greatest common divisor of the number of stator slots Q and the pole pairs p and the value describes the number of electromagnetic symmetric parts into which the electric machine can be divided [26]. The value of the periodicity should be larger than 1 to minimize noise and vibrations caused by forces acting on the rotor [26].

2.6 Torque Ripple

The constant part of the electromagnetic torque is shown in equations (2.22) and (2.23). However, there will also be additional torque components that oscillate and pulsate and those contribute to the torque ripple. Torque ripple is undesirable since it causes noise, vibrations and mechanical stress. In this thesis the torque ripple, expressed as a percentage, is calculated as

$$T_{\text{ripple}}[\%] = \frac{T_{\text{max}} - T_{\text{min}}}{T_{\text{avg}}} \cdot 100, \tag{2.32}$$

where T_{max} is the maximum torque value, T_{min} is the minimum torque value and T_{avg} is the average torque value.

The total generated torque can be expressed as in equation (2.33). Here, t_{total} is the generated electromagnetic torque, T_0 is the constant part of the torque that is described in equations (2.22) and (2.23), t_{h} is torque generated from harmonics and t_{cog} is the cogging torque.

$$t_{\text{total}} = T_0 + t_{\text{h}} + t_{\text{cog}} \tag{2.33}$$

The harmonic torque t_{h} contains several components: torque generated from harmonics in the stator current, torque generated from harmonics in magnetic flux and torque generated from the interaction between harmonics in the stator current and harmonics in the magnetic flux [28]. The torque generated from the interaction between harmonics in the stator current and harmonics in the magnetic flux is much smaller compared to the other two and can therefore be neglected [28].

Cogging torque, T_{cog}, is produced from the interaction between the iron in the stator and the magnetic flux produced in the rotor. The rotor magnetic flux naturally aligns with the flux path with the lowest reluctance, which causes an unsmooth rotation of the rotor [29], [30]. Since cogging torque is caused by reluctance it is present no matter the amplitude of the stator current [29], [30]. The period of the cogging torque in mechanical degrees is

$$\Theta_{\text{cog}} = \frac{360^\circ}{LCM(Q, 2p)}, \tag{2.34}$$

where $LCM(Q, 2p)$ is the least common multiplier between the number of slots and number of poles [30]. To obtain a low cogging torque $LCM(Q, 2p)$ and the periodicity of the motor should be high [26].

2.6.1 Harmonics in Three-Phase Electric Machines

Even harmonics will disappear in a three-phase electric motor if the input signals are half-wave symmetric [19]. Moreover, also third order harmonics $n = 3k$, ($k = 1, 2, 3...$) are canceled for the currents in a balanced three-phase system with a star connection and no neutral [19]. This is because the third order harmonic components from the three phases are equal with the same phase angles and amplitudes [19]. If there is no neutral the third order harmonic currents have to add up to zero, meaning that each one of them is zero. The third order harmonics will also cancel in the line voltages. Hence, for EESMs and PMSMs with three phases and no neutral winding the harmonics in the currents and in the line voltages are of orders $n = 6k - 1$ and $n = 6k + 1$ ($k = 1, 2, 3...$) [19].

Torque ripple produced by the interaction of the fundamental current and harmonic flux and the torque ripple produced by the interaction of the fundamental flux and harmonic current will be of order $n = 6k$ ($k = 1, 2, 3...$). Other harmonics will be canceled.

Total harmonic distortion (THD) is a measurement of the amount of harmonics in current and voltage waveforms [31]. In this thesis, THD is calculated in comparison to the fundamental component V_1 as shown in equation (2.35). Here, V_{n} are the amplitudes or the root mean square (RMS) values of the harmonics [31].

$$\text{THD} = \sqrt{\frac{\sum_{\text{n}=2}^{\infty} V_{\text{n}}^2}{V_1^2}} \tag{2.35}$$

2.7 Losses in an Electric Machine

There are several different types of losses in an electrical machine, such as copper losses, iron losses and mechanical losses due to rotation [18]. In this thesis, copper losses and iron losses will be of focus and they are described further in this section.

2.7.1 Copper Losses

When current flow through a copper winding there will be losses. Both EESM and PMSM have copper losses in the stator windings and the total copper loss from all three phases can be calculated as in equation (2.36) [18]. Here, amplitude-invariant transformation has been used and R_{s} is the per phase resistance of the stator windings.

$$P_{\text{Cu,s}} = \frac{3}{2}(i_{\text{d}}^2 + i_{\text{q}}^2)R_{\text{s}} \tag{2.36}$$

In an EESM there are also copper losses in the field windings in the rotor. These losses can be calculated as in equation (2.37), where, i_{f} is the field current and R_{f} is the resistance of the field winding [18].

$$P_{\text{Cu,f}} = i_{\text{f}}^2 R_{\text{f}}, \tag{2.37}$$

The resistance R of a copper winding can be calculated as

$$R = \frac{\rho L}{A}, \tag{2.38}$$

where ρ is the resistivity, L is the length of the wire and A is the cross section area of the wire [32]. Moreover, the resistivity is temperature dependent according to equation (2.39), where ρ is the resistivity at temperature T, ρ_0 is the resistivity at temperature T_0 and α is the temperature coefficient [32]. The constant α is different for different materials.

$$\rho = \rho_0(1 + \alpha(T - T_0)) \tag{2.39}$$

2.7.2 Core Losses

Electromagnetic fields that vary with time will generate core losses in an electric machine [18], [33]. These losses are not taken into account in the mathematical model of the EESM in Section 2.3.2 but they will be described further in this section.

2.7.2.1 Hysteresis Losses

Ferromagnetic materials, such as the laminated steel in an electric machine, are composed of small domains. Every domain contains approximately 10^{15} to 10^{16} atoms with aligning magnetic dipole moments [15]. The boundaries of a domain are called domain walls and an externally applied field will cause the domain walls to move. If the applied field is strong enough to cause rotation of domains, such that the magnetic dipole moments align with the external field, the movements of the domain walls are said to be non-reversible [15]. This causes the magnetization of the ferromagnetic material to lag and the phenomenon is called hysteresis [15]. If the applied magnetic field varies between $\pm H_\mathrm{m}$ the magnetic flux density will follow the hysteresis loop shown in Figure 2.5 [15]. Here, the lagging effect is clear; when the magnetic field H reaches 0 A/m there is still a flux density B_r. This flux density is called the remanence flux density [17]. A negative magnetic field $-H_\mathrm{c}$, called the coercive force, must be applied to reduce the magnetic flux density to 0 T [17].

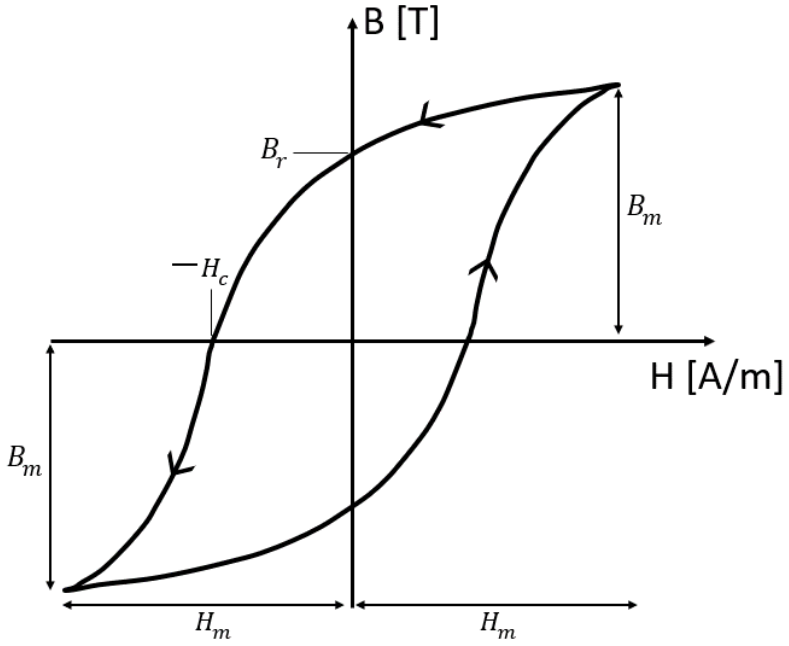

Figure 2.5: Hysteresis loop.

The area enclosed by the loop is proportional to the hysteresis loss per unit volume for each magnetic field period [15], [18]. This loss is caused by friction from rotation and movements of the domains [15], [18]. The corresponding power loss can be calculated from equation (2.40) [2], [17], [18]. Here, B_m is the amplitude of the magnetic flux density, k_h is a material-dependent constant and M is the mass of the core material.

$$p_h = k_\mathrm{h} f B_\mathrm{m}^2 M \tag{2.40}$$

2.7.2.2 Eddy Current Losses

Eddy current losses in the laminated steel are caused by the fact that the steel is conductive [18]. When a varying magnetic field is applied on the core, EMF will be induced in conductive contours in the iron according to equation (2.4) [18]. This results in currents flowing in these contours as shown in Figure 2.6 [17], [18]. These currents are called eddy currents and they cause eddy current losses.

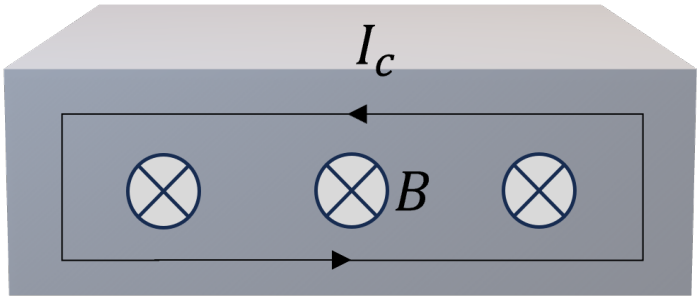

Figure 2.6: Illustration of eddy current I_c generated due to the varying magnetic field B.

Assuming that the magnetic flux density has a magnitude of B_m and varies with a frequency f, the EMF amplitude will be proportional to the product of the magnetic flux density amplitude and the frequency, $\mathcal{E} \propto fB_m$ [18]. The induced current I_C can be calculated as $\mathcal{E}/R_C$, where R_C is the resistance in the contour [18]. Thus, it is true that $I_C \propto fB_m/R_C$ [18]. Power losses due to the eddy current I_C are proportional to $R_C I_C^2 \propto R_C f^2 B_m^2$ and therefore the power loss caused by eddy currents can be calculated as in equation (2.41) [18]. Here, k_c is a constant that depends on the material.

$$p_c = k_c f^2 B_m^2 M \tag{2.41}$$

Traditionally, the total core loss is calculated as the sum of hysteresis losses and classical eddy current losses [33]. However, it has been shown that for many ferromagnetic materials the actual amount of eddy current loss is larger than the classical eddy current losses described above [33], [34]. To compensate for the difference between experimental results and the theoretical value of $p_h + p_c$, excess eddy current losses may be added [33], [34]. The power loss due to excess eddy currents can be calculated as in equation (2.42) [33]. As before, k_e is a material-dependent constant [33].

$$p_e = k_e f^{1.5} B_m^{1.5} M \tag{2.42}$$

2.7.3 Efficiency

The efficiency η can be calculated as

$$\eta[\%] = \frac{p_{\text{out}}}{p_{\text{in}}} \cdot 100 = \frac{p_{\text{em}}}{p_{\text{em}} + p_{\text{Cu}} + p_{\text{Fe}}} \cdot 100, \tag{2.43}$$

where p_{em} is the electromagnetic power, $p_{\text{Cu}} = p_{\text{Cu,s}} + p_{\text{Cu,f}}$ is the total copper loss and $p_{\text{Fe}} = p_{\text{h}} + p_{\text{c}} + p_{\text{e}}$ is the total core loss. It should be noted that only copper losses and core losses are considered to calculate the efficiency in this thesis, other losses such as mechanical losses are neglected.

2.8 Thermal Modeling

Losses in an electrical machine will cause the temperature to increase. There are several mechanisms for heat transfer: conduction, convection and radiation [35]. In this thesis focus will be on modeling the temperature in an electric machine using conduction and convection.

2.8.1 Conduction

In gases and liquids, heat is transferred by conduction when molecules with high energy collide with molecules with lower energy [35]. In solids the heat is instead transferred by lattice vibrations [35]. The heat is always transferred from a region with a higher temperature to a region with a lower temperature and the heat flux $\boldsymbol{q}$ can be calculated from Fourier's law in equation (2.44) [35]. Here, k is the thermal conductivity and ∇T is the temperature gradient. Hence, higher thermal conductivity results in a larger heat flux.

$$\boldsymbol{q} = -k\nabla T \tag{2.44}$$

2.8.2 Convection

Temperature differences within fluids cause density differences. These density differences result in movements of the fluid and heat is transferred by natural convection [36]. Heat can also be transferred by forced convection and that is when the movements of the fluid are caused by external forces, such as a pump or a fan [36]. The heat flux to or away from a surface with temperature T_s is calculated from Newton's law of cooling in equation (2.45) [35].

$$q = h(T_{\text{s}} - T_{\infty}) \tag{2.45}$$

Here, h is the convective heat transfer coefficient and T_{∞} is the temperature of the cooling fluid.

3

Initial Model Setup

In this chapter, the initial model setup for the EESM is described in detail. First, the operating region of the air compressor is presented. Then, the setups for electromagnetic and thermal simulations of both the EESM and the reference PMSM are described. For these simulations the finite element method (FEM) is used. FEM is a method that numerically solves partial differential equations in subdomains, so-called finite elements, that are part of a larger domain. Finally in this chapter, a method for geometry optimization of the EESM and methods for current optimization are explained. Since this project only includes simulations and no external data is collected it is considered to have no environmental, societal or ethical consequences. Thus, there is no further discussion on those aspects regarding the method choice.

3.1 Air Compressor

The motor investigated in this thesis is for the application of an air compressor. This air compressor is used to create pressure in a tank to open the entry doors in buses. The motor is powered by a battery with a DC voltage of 600 V.

3.1.1 Operating Region for the Air Compressor

The operating point of the compressor is dependent on the pressure in the tank, and this is shown in Table 3.1. The corresponding torque-speed curves can be seen in Figure 3.1. It is shown that the pressure in the tank can vary between 8 bar and 15 bar, the speed can vary between 1500 rpm to 3500 rpm and the torque can vary between 12.6 Nm to 22.2 Nm. For this project, an operating region is defined. This operating region includes all torque values between 12.6 Nm and 22.2 Nm in the speed interval 1500 rpm to 3500 rpm. This is a simplification that gives a slightly larger operating region than that in Figure 3.1.

Table 3.1: Torque at different speeds and pressures for the air compressor.

Pressure / Speed	8 bar	10 bar	11 bar	13 bar	15 bar
1500 rpm	13.7 Nm	15.6 Nm	17.2 Nm	19.1 Nm	22.2 Nm
2000 rpm	13.3 Nm	15.0 Nm	16.2 Nm	18.1 Nm	20.7 Nm
2500 rpm	12.7 Nm	14.4 Nm	15.7 Nm	17.8 Nm	19.9 Nm
3000 rpm	12.6 Nm	14.2 Nm	15.4 Nm	17.4 Nm	19.4 Nm
3500 rpm	12.6 Nm	14.2 Nm	15.4 Nm	17.3 Nm	19.1 Nm

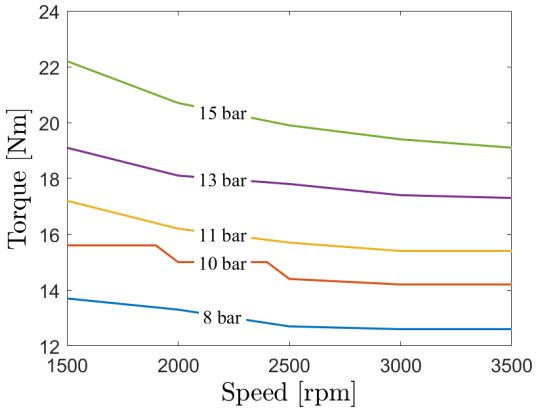

Figure 3.1: Torque-speed curves for different pressures.

3.1.2 Nominal Operating Point and Design Requirements

Rated power, nominal torque, nominal speed and nominal voltage for the motor are shown in Table 3.2. The designed EESM must fulfill the requirement regarding nominal torque at the nominal speed for continuous operation.

Table 3.2: Rated and nominal values for the reference PMSM.

Rated power (W)	7300
Nominal torque (Nm)	20
Nominal speed (rpm)	3500
Nominal voltage (V)	600

Other aspects to consider are the temperature in the motor and the torque ripple. The motor may operate for long times and should therefore be designed for continuous operation. The maximum temperature in the motor should never be higher than 170 °C to not speed up the aging process of the motor. The temperature in the motor should not surpass this temperature limit for continuous operation at operating points with a torque of 20 Nm (nominal torque) or lower. The stator of the reference PMSM is water-cooled. If nothing else is mentioned, this cooling technique was also used for the thermal analysis of different EESM designs. Moreover,

torque ripple is not very important for an air compressor application. However, to avoid unnecessary noise, vibrations and mechanical stress the torque ripple of the designed EESM should not be larger than that of the reference PMSM in the nominal operating point. The torque ripple of the PMSM at the nominal operating point is 59.0 %.

3.2 Setup in Ansys Maxwell for Electromagnetic Simulations

In this section it is described how the PMSM and the EESM were implemented in the software Ansys Maxwell for electromagnetic analysis.

3.2.1 Implemented Geometries

Both the geometry of the PMSM and the geometry of the EESM were implemented in 2D to save computational cost. Furthermore, only one fourth of the radial cross section was implemented. This simplification was possible to do since the machines have four pole pairs and each pole pair will have the same electromagnetic behavior.

The topology of the reference PMSM is shown in Figure 3.2. The motor has a three-phase double layer FSCW with 12 stator slots. The coils for each phase are connected in series. The number of pole pairs is equal to 4. Thus, the number of slots per pole per phase is $q = \frac{1}{2}$, and it is therefore the fundamental component that will produce the torque. This winding configuration has a fundamental winding factor of 0.866 [26]. Moreover, according to [26], this winding configuration also has high enough periodicity and $LCM(Q, 2p)$ to limit noise, vibrations and cogging torque.

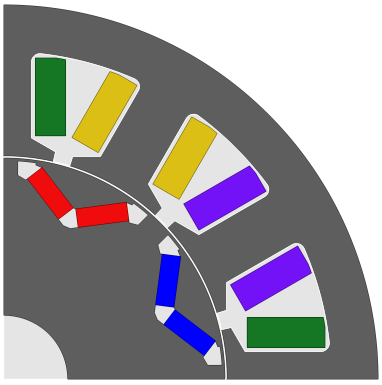

Figure 3.2: Geometry of reference PMSM.

A base model of the EESM is shown in Figure 3.3a. Similar models have been investigated for traction applications, and shown to be a promising alternative to PMSMs, in several previous studies [2], [4] [12], [14], [37]. The parameters x_1 x_2, x_3, x_4 and x_5 of the rotor pole of the EESM are shown in Figure 3.3b. These parameters are the rotor pole body width, rotor pole body height, rotor pole shoe

width, rotor pole shoe height and the total height of the rotor pole shoe, respectively. These parameters will be optimized from a parametric sweep described in Section 3.4. The rotor coils in Figure 3.3a are used for the electromagnetic simulations. However, in a real motor the total copper area will be equal to the product of the fill factor and the slot area, $A_{\mathrm{Cu}} = k_{\mathrm{r,fill}} A_{\mathrm{r,slot}}$. The rotor slot area will be different for different combinations of the parameters x_1 x_2, x_3 x_4 and x_5; thus, different numbers of turns of the field winding will be used for the different designs.

Furthermore, since the winding configuration used in the PMSM is considered to have rather good performance the same stator and winding configuration was used for the EESM to simplify the design process.

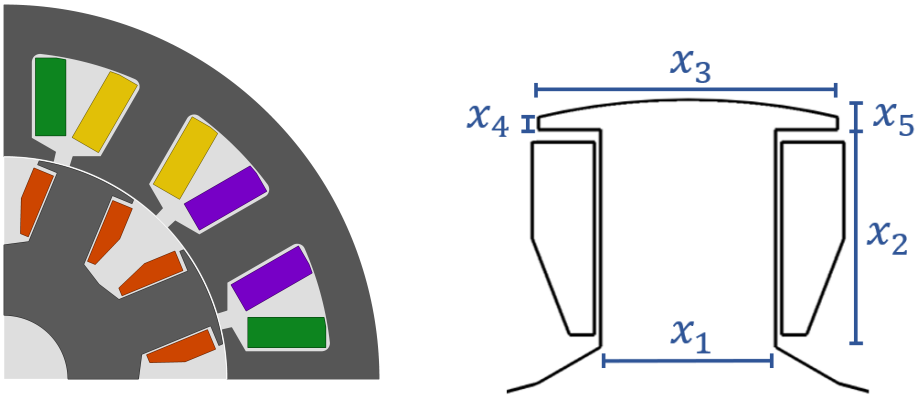

(a) EESM base model. **(b)** Rotor pole parameters.

Figure 3.3: Geometry of a base model of the EESM.

3.2.2 Important Design Parameters

Important design parameters for both the PMSM and the EESM are shown in Table 3.3. These parameters will be fixed for the parametric sweep and, therefore, the pole parameters, the number of turns of the field winding and the field winding resistance are not shown in the table.

Table 3.3: Design parameters for the PMSM and the initial EESM model.

Parameter	**Denotation**	**PMSM**	**EESM**	**Unit**
Shaft length	L_{shaft}	47	47	mm
Outer diameter of stator	OD_{stator}	176	176	mm
Inner diameter of stator	ID_{stator}	105	105	mm
Air gap	g_{air}	0.5	0.5	mm
Shaft diameter	d_{shaft}	30	30	mm
Number of stator slots	Q	12	12	-
Number of pole pairs	p	4	4	-
Number of phases	m	3	3	-
Number of slots per pole per phase	q	1/2	1/2	-
Wire diameter stator	$d_{\text{s,wire}}$	1.5	1.5	mm
Wire diameter rotor	$d_{\text{r,wire}}$	-	1	mm
Fill factor stator	$k_{\text{s,fill}}$	0.32808	0.32808	-
Fill factor rotor	$k_{\text{r,fill}}$	-	0.32	-
Stator slot area	$A_{\text{s,slot}}$	474.00	474.00	mm^2
Stator winding number of turns	$N_{\text{s,turns}}$	44	44	-
Stator phase resistance (20 °C)	$R_{\text{s,20}}$	0.303	0.303	Ω
Stator phase resistance (120 °C)	R_{s}	0.421	0.421	Ω
DC link voltage	U_{DC}	600	600	V
Maximum stator current amplitude	$I_{\text{s, max}}$	59.3	59.3	A
Maximum field current	$I_{\text{f, max}}$	22	22	A
Maximum temperature	T_{max}	170	170	°C

A few things should be noted regarding the strand diameter of the field winding, the fill factor of the rotor slots, the resistance estimations and the maximum currents. The strand diameter of the field winding $d_{\text{r,wire}}$ had to be chosen. Values between 0.7 mm and 1.4 mm were considered feasible and the value was arbitrarily set to 1 mm. The fill factor of the rotor slots $k_{\text{r,fill}}$ was also estimated. It was not considered possible to achieve a higher fill factor than what is used for the stator winding and the fill factor in the rotor was therefore set to $k_{\text{r,fill}} = 0.32$.

The resistance of both the stator windings and the field winding also had to be estimated to calculate the copper losses. The procedure for this is shown in Appendix A. In Table 3.3 the resistances are presented both at 20 °C and 120 °C. The values at 120 °C are the resistances used for thermal modeling and copper loss calculations.

Moreover, the maximum stator phase current amplitude $I_{\text{s, max}}$ is the maximum current that can be provided by the inverter. Thermal issues must be taken into account to decide the maximum current that the motor can be provided with continuously. The maximum field current $I_{\text{f, max}}$ is also the maximum current that can be provided to the field windings for a short amount of time. This value was chosen rather arbitrarily since the energy transfer to the rotor is not investigated in this thesis. Moreover, the maximum field current will affect the maximum peak torque; however, this value is not significant since it is the continuous torque that matters.

3.2.3 Material Properties for Electromagnetic Simulations

The rotor and the stator in both the reference PMSM and the EESM are made of the steel material M310-50A [38], which B-H curve is shown in Appendix B. The hysteresis coefficient was set to $k_{\mathrm{h}} = 291.432\,\mathrm{W/m^3}$, the classical eddy current coefficient was set to $k_{\mathrm{c}} = 0.693\,\mathrm{W/m^3}$ and the excess eddy current coefficient was set to $k_{\mathrm{e}} = 0\,\mathrm{W/m^3}$. The density of M310-50A is typically $7650\,\mathrm{kg/m^3}$ [39].

The windings in the stator and the windings in the rotor of the EESM are made of annealed copper with a resistivity of $1.724 \cdot 10^{-8}\,\Omega\,\mathrm{m}$ at the temperature $20\,^{\circ}\mathrm{C}$ [32]. The constant α is $3.9 \cdot 10^{-3}\,\mathrm{K^{-1}}$ [32]. Furthermore, copper has a density of $8960\,\mathrm{kg/m^3}$ [32].

The PMSM has no rotor windings, but it has permanent magnets. These magnets are of the type NdFeB45SH. This magnet has a maximum energy product $(BH)_{\max}$ of 45 MGOe.

3.2.4 Implemented Mesh

Both motors were meshed to generate subdomains for the FEM analysis. The mesh of the reference PMSM is shown in Figure 3.4a and the mesh around the air gap can be seen in more detail in Figure 3.4b. The number of mesh elements in the PMSM model is 8710. Similar mesh settings were used for the EESM and the mesh is shown in Figure 3.4c. In Figure 3.4d the mesh close to the air gap for the EESM is shown. The number of mesh elements in the EESM model is around 10000, the exact value differs for different designs. For both motors, the mesh is very fine in the air gap to capture the electromagnetic interaction of the stator and the rotor.

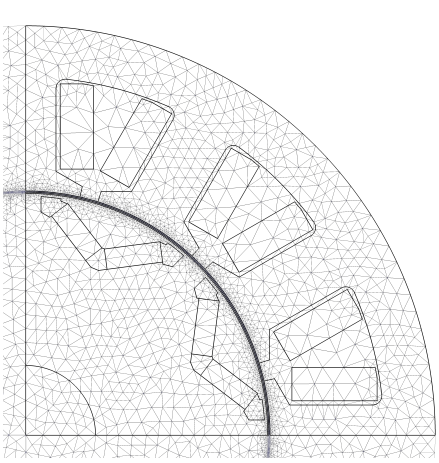

(a) Mesh for PMSM.

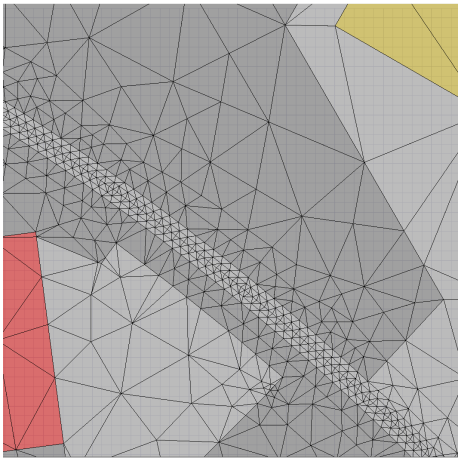

(b) Mesh in airgap for PMSM.

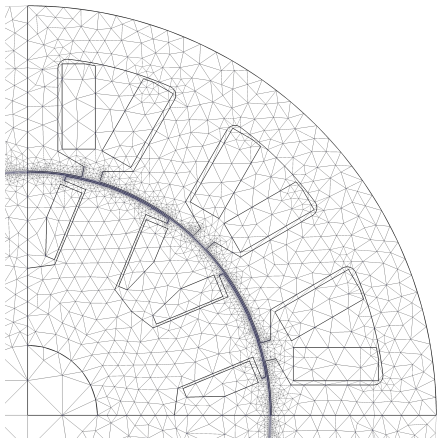

(c) Mesh for EESM.

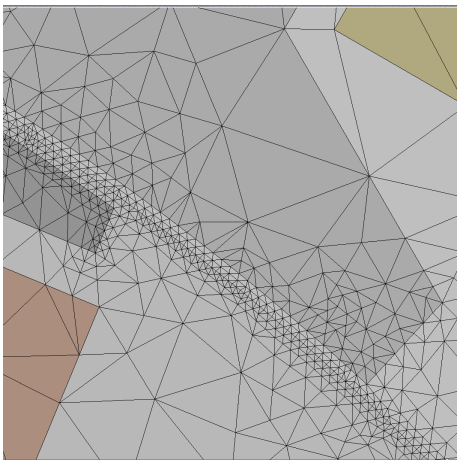

(d) Mesh in airgap for EESM.

Figure 3.4: Mesh for both motors.

3.2.5 Analysis Setup

In Ansys Maxwell, the stator currents were modeled as pure sinusoidal waves and the field current was modeled as a pure DC current. The maximum currents presented in Table 3.3 are assumed to also include various disturbances and harmonics, which currents in a real electric motor do. Thus, the maximum values of the pure sinusoidal stator current and the pure DC field current should not be set to the maximum values in Table 3.3, a margin to account for the disturbances and harmonics should be implemented. This margin was set to 10 %. Thus, for the analyses in Ansys Maxwell the maximum stator current amplitude was set to $59.3/1.1\,\mathrm{A} = 53.9\,\mathrm{A}$ and the maximum field current was set to $22/1.1\,\mathrm{A} = 20\,\mathrm{A}$.

Furthermore, a time step had to be set for the electromagnetic analyses. A very small time step would result in a long simulation time and if a too long time step was used the torque ripple would not be captured. A sweep of the time step was performed with values between 4 µs and 80 µs and average torque, torque ripple, THD and core

losses were investigated. The speed was set to the nominal speed of 3500 rpm. It was concluded that a time step of 40 µs captured all quantities of interest. This corresponds to approximately 19 measurement points for each period of the sixth harmonic of the torque ripple. Hence, the time step was set to 40 µs. For simulations on lower speeds the time step was set such that there were 20 measurement points for each period of the sixth torque ripple harmonic.

3.3 Setup in Ansys Mechanical for Thermal Simulations

The temperature in the motor increases during operation due to losses. To estimate the maximum currents that the EESM can be fed with without overheating thermal simulations in Ansys Mechanical were performed. Several assumptions were made to simplify the setup of the thermal model and those will be described further in this section. It should be noted that depending on how accurate these assumptions are the thermal analysis may be more or less correct. Therefore, the thermal results will mainly be used to give an idea of how different current values influence the temperature in the EESM, not to determine any exact values.

3.3.1 Thermal Results for the Reference PMSM

Thermal simulations and measurements have been performed on the reference PMSM before the start of this project. It has been concluded that the core losses in the rotor can be neglected for thermal simulations and that the maximum phase current amplitude that can be provided to the stator in continuous operation is 23.73 A. Note that this current amplitude includes the disturbances and harmonics that are present in a real motor. To get the corresponding pure sinusoidal current used in Ansys Maxwell a margin of 10 % should be used.

3.3.2 Implemented Geometries

For the PMSM core losses in the stator and the rotor and copper losses in the stator windings will generate heat. Since it already has been concluded that the rotor core losses do not contribute to the steady state temperature, only the stator was investigated and the implemented geometry is shown in figure 3.5a. This is a 3D model and the length of the stator is the actual stack length L_{stack}. Note that no isolated copper strands are modeled in the stator slots, instead the slots consist of a homogeneous equivalent material. This is a simplification that was made to reduce the complexity of the geometry and boundary conditions.

Figure 3.5b shows the implemented geometry of the EESM. The stator is the same as for the PMSM, however, due to copper losses in the field windings also the rotor had to be considered. The rotor slots are also modeled with an equivalent homogeneous material.

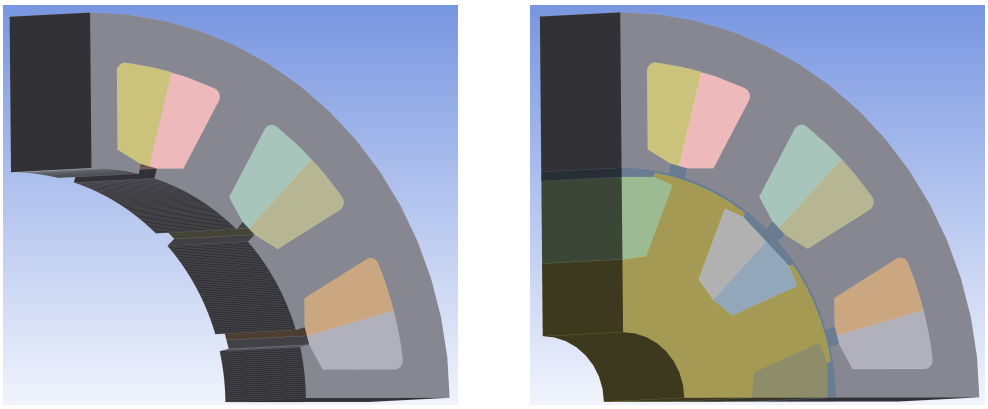

(a) PMSM. **(b)** EESM.

Figure 3.5: Implemented geometries for thermal simulations.

Another simplification is that the end windings are not modeled. The main reason for this simplification is that the isolated copper wires will have different thermal conductivity in different directions. This makes it difficult to implement an equivalent material for the isolated copper that conducts current in more than one direction. The thermal conductivity of the equivalent material will be further discussed in Section 3.3.3. However, with no end windings the cooling will be less efficient, causing the thermal model to overestimate the temperature.

3.3.3 Material Properties for Thermal Simulations

Thermal conductivity is an important material property for thermal analysis. The laminated steel has higher thermal conductivity within one layer compared to between two layers. In Figure 3.6a this corresponds to a thermal conductivity value of $27\,\mathrm{W/(m \cdot K)}$ in the x- and y-directions and a thermal conductivity of $0.27\,\mathrm{W/(m \cdot K)}$ in the z-direction. These values were recommended to use by the R&D department at Aros Electronics.

The isolated copper wires are modeled with a homogeneous material that has an equivalent thermal conductivity to the isolated copper wires. Copper has a much higher thermal conductivity compared to the isolation layer around the copper strands. The thermal conductivity of copper is $401\,\mathrm{W/(m \cdot K)}$ and the thermal conductivity of the isolation layer is $0.18\,\mathrm{W/(m \cdot K)}$ [32]. In the direction that the current flows, the z-direction in Figure 3.6b, the thermal conductivity was set to be the same as for copper. However, the isolation layer will greatly affect the thermal conductivity between the strands. Previous thermal measurements on the PMSM were used to find a suitable value for the thermal conductivity in the x- and y-directions in Figure 3.6b for the homogeneous material. These measurements show that the PMSM reaches the maximum temperature $170\,^{\circ}\mathrm{C}$ when it is fed with the current amplitude $23.73\,\mathrm{A}$. By setting the stator current amplitude to $23.73\,\mathrm{A}$ and using the corresponding core losses it was found that the thermal conductivity in the x- and y-directions must be $0.76\,\mathrm{W/(m \cdot K)}$ for the temperature to reach $170\,^{\circ}\mathrm{C}$.

Here, the model in Figure 3.5a was used. However, it was assumed that the thermal conductivity 0.76 W/(m · K) could be used for both the stator slots and the rotor slots for the EESM.

The thermal conductivity in the air gap also had to be estimated. Air has a thermal conductivity of 0.0254 W/(m · K) [32]. Since the air in the air gap is moving when the rotor rotates it was considered necessary to set the thermal conductivity to a value slightly higher than 0.0254 W/(m · K). Recommendations from the R&D department at Aros suggested that the thermal conductivity in the air gap should be close to 0.1 W/(m · K), and this value was therefore used.

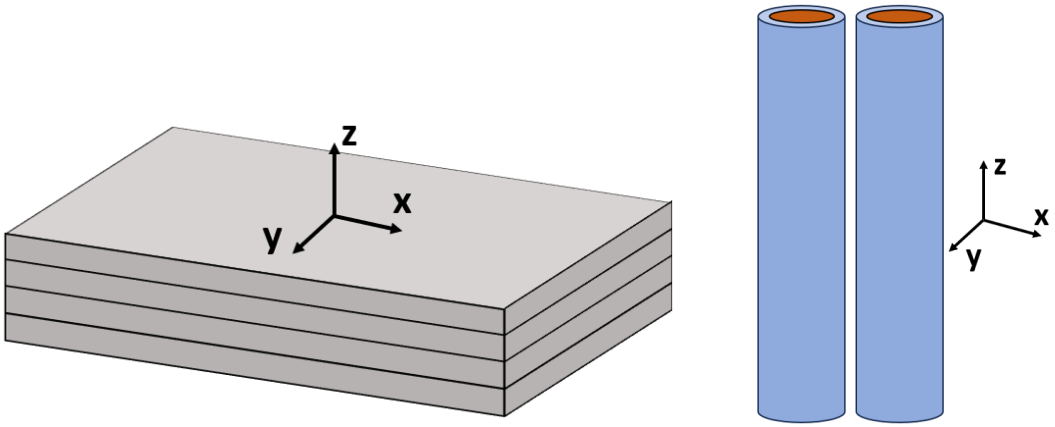

(a) Laminated steel.

(b) Isolated copper wires.

Figure 3.6: Illustration of laminated steel and isolated copper wires.

3.3.4 Implemented Mesh

The mesh of the thermal model of the EESM is shown in Figure 3.7 and contains 232278 elements. The minimum length of an element edge is 0.0042 mm and the maximum is 16 mm. It should be noted that these values varied slightly depending on the pole parameters.

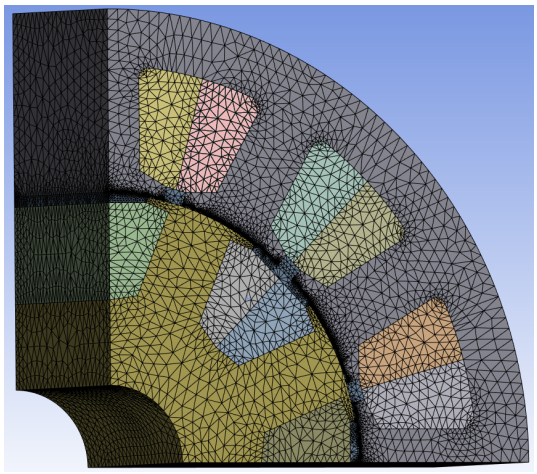

Figure 3.7: Mesh for EESM in Ansys Mechanical.

3.3.5 Boundary Conditions for Thermal Simulations

Both copper losses and core losses had to be added to the thermal models. Copper losses were added to the stator slots for the PMSM and the stator slots as well as the rotor slots for the EESM. These copper losses were calculated from equations (2.36) and (2.37) using the current values and the estimated resistance values. Harmonics and disturbances in the currents are neglected for the electromagnetic simulations in Ansys Maxwell. However, for more accurate thermal simulations possible disturbances should be taken into account. Therefore, all currents from Ansys Maxwell were multiplied with a factor of 1.1 before doing the thermal analysis.

Core losses were added to the stator core for the PMSM and both the stator core and the rotor core for the EESM. These values were obtained from the electromagnetic simulations in Ansys Maxwell. However, in reality there will be more harmonics in the magnetic flux compared to the simulations. To account for this the core losses obtained from Ansys Maxwell were multiplied with a factor of 1.7.

Boundary conditions for how heat will transfer away from the machines also had to be set. In Figure 3.8 some of the boundaries of the EESM model are marked with numbers. Note that the boundary conditions used for the stator were the same for the PMSM. The boundary marked with number 1 is the outside of the stator. This boundary is water-cooled and is therefore cooled by convection. The convective heat transfer coefficient was set to $2000\,\mathrm{W/m^2K}$ and the water had a temperature of $70\,^{\circ}\mathrm{C}$. Inside the motor there is no water, only air, and it was assumed that both the rotor and the stator are cooled by convection due to the air. When a surface is in contact with air and is cooled by natural convection the convective heat transfer coefficient is approximately $5\,\mathrm{W/m^2K}$. If the surface is moving the convective heat transfer coefficient will be slightly higher than this. Boundary 2 is the rotor core and the field windings and this boundary will be rotating. Using recommendations from the R&D department at Aros the convective heat transfer coefficient was set to $25\,\mathrm{W/m^2K}$ and the temperature in the air was set to $100\,^{\circ}\mathrm{C}$. Boundary 3 is not moving and the convective heat transfer coefficient should therefore be lower than

for boundary 2. For simplicity, the heat transfer coefficient on boundary 3 was set to 5 W/m^2K, same as for natural convection. Since the air is moving due to the rotation of the motor this will overestimate the temperature.

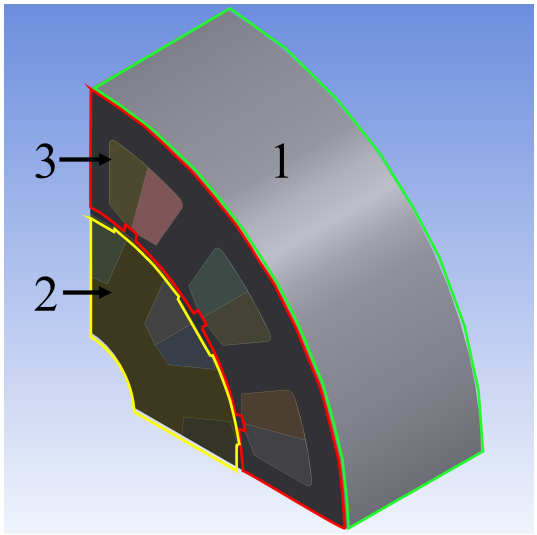

Figure 3.8: Boundaries of the EESM model.

3.4 Parametric Sweep

To find an optimal geometry for the EESM a parametric sweep was performed with the parameters x_1 x_2, x_3 and x_4 shown in Figure 3.3b. The aim of the parametric sweep was to design a rotor with a high continuous torque, preferably 20 Nm or higher. Moreover, the obtained torque ripple in the investigated operating point should be lower than the torque ripple that the PMSM exhibits in the nominal operating point.

For the electromagnetic simulations, the speed was set to 3500 rpm for all investigated geometries since that is the nominal speed. The sweep was performed in Ansys Maxwell; hence, all current and copper loss values mentioned in this section are the values corresponding to the pure sinusoidal stator currents and the pure DC field current.

3.4.1 Determine Parameter Limits

First, parameter limits due to manufacturing and durability reasons had to be investigated. It was assumed that a rotor pole height, x_2, larger than 22 mm would cause difficulties for the winding process. The rotor pole shoe height, x_4, should not be smaller than 0.6 mm; smaller values might cause problems for large scale manufacturing. Furthermore, the rotor pole shoe width, x_3, should at least be 2 mm larger than the rotor pole width, x_2, otherwise there might be a problem for the field winding to stay in place when the rotor rotates. The other limits were set based on the results from a few initial sweeps and will be further discussed in Section 4.1.1. All limits are shown in Table 3.4. The parameters x_1, x_2 and x_3 were varied with

a step of 1 mm and the parameter x_4 was varied with a step of 0.25 mm. All the different combinations of x_1, x_2, x_3 and x_4 were then investigated. For all sweeps, the parameter x_5 was set such that the curvature of the rotor pole shoe followed the curvature of the stator.

Table 3.4: Parameter limits used for the parametric sweep.

Parameter	**Lower limit [mm]**	**Upper limit [mm]**
x_1	11	17
x_2	16	22
x_3	16	27
x_4	0.6	2.35

3.4.2 Determine Stator Current Amplitude and Field Current

Ideally, thermal simulations should be performed for each investigated geometry to determine the maximum currents that could be used to keep the steady state temperature below 170 °C. However, due to limited time this was not possible and the currents had to be determined in another way.

The stator phase currents were set to be pure sinusoidal waves with an amplitude of 18 A. For the PMSM this current will give approximately 20 Nm at MTPA, which is the nominal torque.

To decide the field current amplitude the thermal aspect had to be taken into consideration. The resistance of the field winding is different for different geometries. This is due to two reasons: the shape of the rotor poles is different and different rotor slot areas result in different numbers of turns of the field winding. If the same field current would have been used for all geometries some would result in much higher copper losses than others, making it difficult to ensure that no geometry results in a higher steady-state temperature than 170 °C. To avoid having to perform thermal simulations for all different geometries the copper losses in the field winding were set to a constant value of 40 W. This value for the copper losses was considered reasonable since thermal simulations of a few different EESM models with different core losses resulted in a steady state temperature between 150 °C and 170 °C.

3.4.3 Sweep Method

For all investigated geometries the torque was then obtained from Ansys Maxwell at MTPA. MTPA was found for each geometry by sweeping the current angle and comparing the torque values. Note that the MTPA angle was not calculated analytically by using equation (2.29) since the inductance values are non-linear and vary for different values of the currents I_d, I_q and I_f.

The average torque and the torque ripple were studied for all investigated geometries. The 40 geometries with the highest torques that fulfilled that the torque ripple was smaller than that of the PMSM were further analyzed. The focus was on studying

the core losses, both in the stator and in the rotor. If the core losses are low it might be possible to increase the currents without overheating the motor. Furthermore, lower core losses will result in a higher efficiency since the copper losses are equal for all investigated models.

However, it is advantageous if the chosen model also performs well for higher field currents. Higher field current might be possible to use if a more efficient cooling technique is implemented, which will be investigated in Chapter 6. For the 40 chosen models the average torque, the torque ripple and core losses were therefore also investigated when the copper losses in the field winding were set to 120 W. This value was chosen relatively arbitrarily, however, it was not considered likely that much higher copper losses than that are possible even for more efficient cooling techniques.

Finally, an EESM model was chosen among those 40 models based on average torque value, torque ripple and core losses for both a copper loss of 40 W and a copper loss of 120 W in the field windings. The entire parametric sweep process is summarized in Figure 3.9.

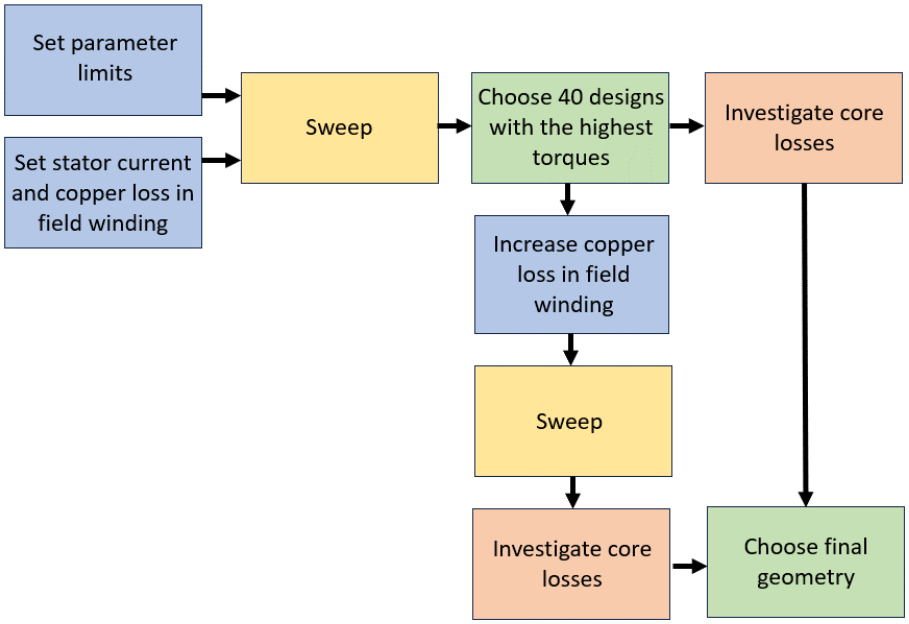

Figure 3.9: Parametric sweep process.

3.5 Copper Loss Minimization

The currents had to be optimized to analyze the performance of the EESM design chosen from the parametric sweep. In this section, it is described how the optimal currents were found for each operating point for the reference PMSM and the designed EESM.

3.5.1 Copper Loss Minimization for PMSM

For a PMSM only the currents I_d and I_q have to be optimized to achieve desirable performance. To minimize the copper losses the stator current has to be minimized and for that MTPA can be used. In this project the currents in a specific operating point were determined using MTPA. Moreover, for all operating points the phase voltage was investigated so that it did not exceed the voltage limit $U_\mathrm{s,lim} = U_\mathrm{DC}/\sqrt{3}$.

3.5.2 Copper Loss Minimization Algorithm with Penalty Factors for EESM

For an EESM the optimization problem is more complex since there is also a field current I_f. To achieve a high continuous torque without overheating, the losses in the motor should be minimized. In this section, an iterative algorithm that is used to minimize copper losses with different penalty factors on the stator and field currents is presented. This algorithm is strongly influenced by previous work in [2] and [40].

The iterative algorithm is illustrated in Figure 3.10 and was applied on one operating point at a time. The torque in the investigated operating point is called reference torque and the speed is called reference speed. First, initial values of the stator current amplitude I_s, the current angle θ and the field current I_f were chosen. In this project the initial values were set as $I_\mathrm{s} = I_\mathrm{s,max}/2$, $\theta = \pi/2$ and $I_\mathrm{f} = I_\mathrm{f,max}/2$. A parameter sweep was then performed to get arrays with I_s values, θ values and I_f values around the initial values. The ranges were determined by a parameter k and initially k was set such that the entire operating range was covered. A 3D matrix was then created with the corresponding I_d, I_q and I_f values. Each element in this matrix contained one I_d value, one I_q value and one I_f value. One at a time these elements went through an inner loop. In the inner loop the amplitude of the stator current was investigated. If the amplitude was below $I_\mathrm{s,max}$ the matrix element was analyzed further.

For each investigated combination of I_d, I_q and I_f the flux linkages Ψ_d and Ψ_q were interpolated from flux linkage 3D maps and the torque value was interpolated from a 3D torque map. These 3D maps contained information about the flux linkage, or torque, at specific current levels of I_d, I_q and I_f. Intuitively, the 3D maps can be seen as extended dq-planes, where information dependent on I_f is on a third axis perpendicular to the dq-plane. The data for creating these maps came from FEM simulations in Ansys Maxwell and for one EESM model they are visualized in Section 5.1. The stator voltage amplitude U_s was then calculated using the interpolated flux linkages values, the reference speed and equation (2.16). If the phase voltage amplitude was less than the voltage limit, $U_\mathrm{s,lim} = U_\mathrm{DC}/\sqrt{3}$, and the interpolated torque value was equal to, or larger than, the reference torque the loss was calculated. The loss function used for this project is described in equation (3.1). This loss function calculated the copper losses with penalty factors k_d, k_q and k_f on the stator current and the field current respectively. Since there will be hot spots in the copper windings it was considered most important to minimize the copper losses. Using different penalty factors makes it possible to distribute the

copper losses between the stator windings and the field windings. However, the loss function could also be the total loss or aim to minimize the field current.

$$P_{\text{loss}} = \frac{3}{2}(k_{\text{d}} I_{\text{d}}^2 + k_{\text{q}} I_{\text{q}}^2) + k_{\text{f}} I_{\text{f}}^2 \tag{3.1}$$

If the calculated loss P_{loss} was smaller than the previous minimum loss $P_{\text{loss,min}}$, the initial values were updated such that they corresponded to that matrix element. This inner loop was repeated for all elements in the 3D matrix. Then the error ϵ was calculated as

$$\epsilon = \sqrt{(I'_{\text{d}} - I''_{\text{d}})^2 + (I'_{\text{q}} - I''_{\text{q}})^2 + (I'_{\text{f}} - I''_{\text{f}})^2}, \tag{3.2}$$

where I'_{d}, I'_{q} and I'_{f} are the currents that resulted in lowest loss in this iteration and I''_{d}, I''_{q} and I''_{f} resulted in the lowest loss the previous iteration. If the error was smaller than a limit ϵ_{lim} the parameter k was reduced. The ranges for I_{s}, θ and I_{f} were then smaller in the next iteration. If k was smaller than a predefined limit k_{lim} the algorithm stopped and the optimized currents were I'_{d}, I'_{q} and I'_{f}.

For each operating point the core losses were then interpolated from a 4D map, where each element included information about the core losses at specific currents I_{d}, I_{q} and I_{f} and a specific mechanical speed of the rotor Ω_{mech}. Parts of a 4D map over the core losses for one designed EESM model are shown in Section 5.1.4. Here, the core losses in the dq-plane are shown for four different field currents and one speed value. It should be noted that the 4D map has a slightly lower resolution compared to the 3D maps over the flux linkages and the torque. This is due to limited time.

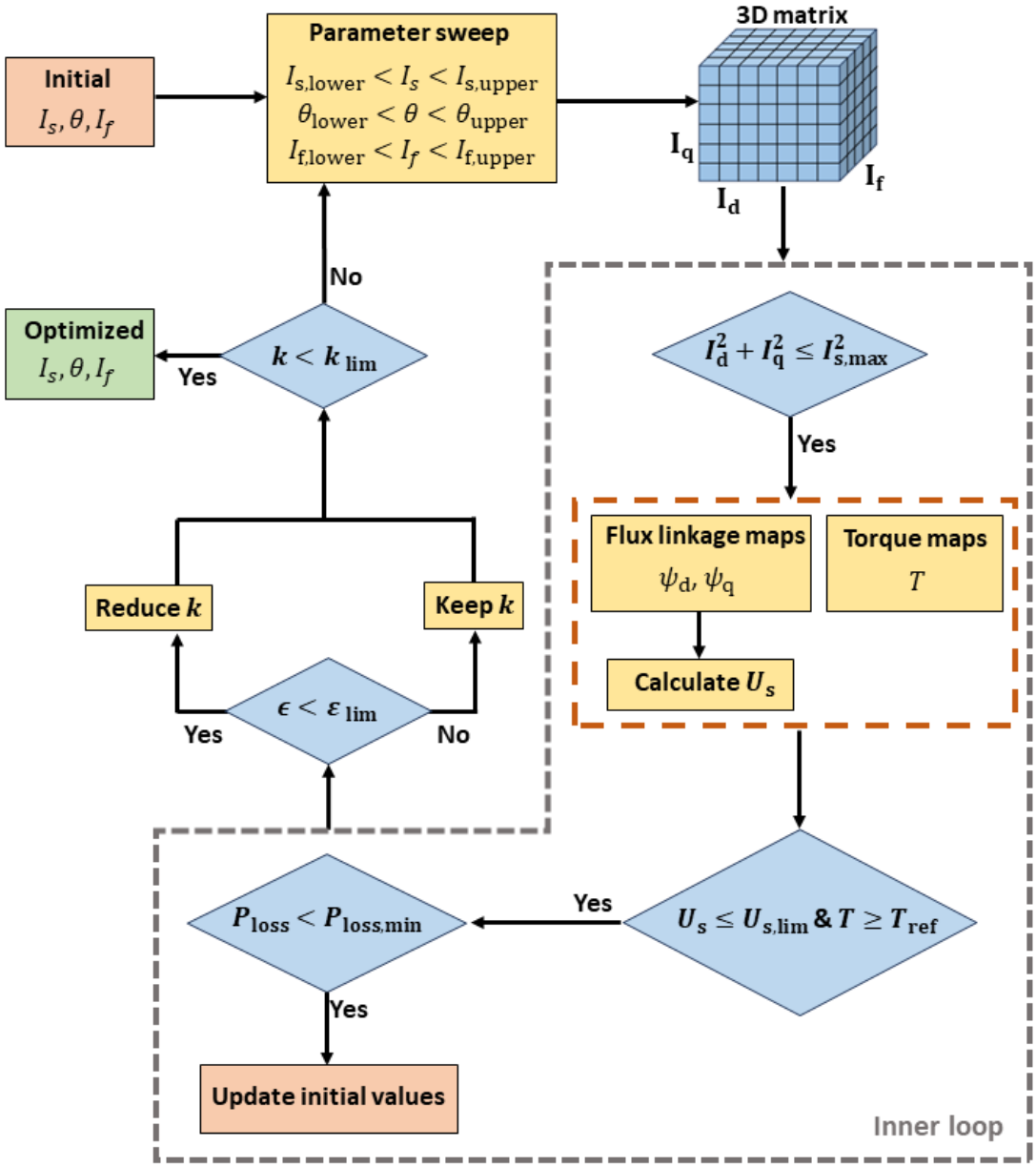

Figure 3.10: Flow chart of the copper loss minimization algorithm used to find optimal currents for the EESM.

4

Geometry Validation of EESM

This chapter presents the geometry chosen from the parametric sweep and discusses how different rotor geometries affect the continuous torque. It is also investigated if it is possible to increase the continuous torque by modifying the geometry further. Finally, an EESM model that has a continuous torque output of 20 Nm is presented. All simulations are performed at the speed 3500 rpm since that is the nominal speed. It should also be noted that all the current and copper loss values mentioned in this chapter are the values used in Ansys Maxwell for the pure sinusoidal stator currents and the pure DC field current.

4.1 Results from Parametric Sweep

The geometry chosen from the parametric sweep is shown in Figure 4.1 and the corresponding design parameters are shown in Table 4.1. All other design parameters are unchanged from the initial model setup shown in Table 3.3. Further on, this geometry will be called EESM-1. More results from the parametric sweep are shown in Appendix C.

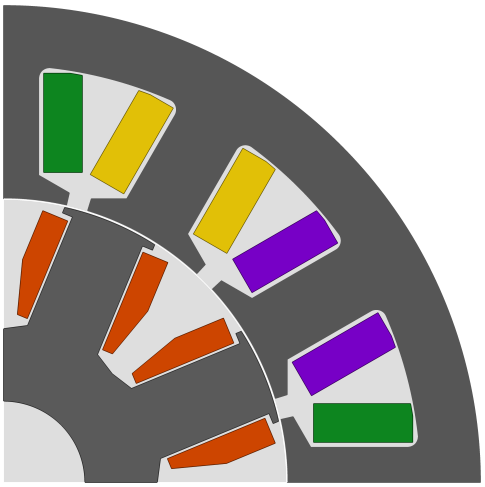

Figure 4.1: Geometry of EESM-1 that is chosen from the parametric sweep.

Table 4.1: Design parameters for EESM-1.

Parameter	Denotation	Value	Unit
Rotor pole body width	x_1	14	mm
Rotor pole body height	x_2	22	mm
Rotor pole shoe width	x_3	18	mm
Rotor pole shoe height	x_4	1.1	mm
Total rotor pole shoe height	x_5	1.89	mm
Number of turns in rotor per pole	$N_{\mathrm{r,turns}}$	74	-
Rotor slot area	$A_{\mathrm{r,slot}}$	363.34	mm^2
Field winding resistance (20 °C)	$R_{\mathrm{f,\ 20}}$	2.252	Ω
Field winding resistance (120 °C)	R_{f}	3.131	Ω

4.1.1 Influence of Rotor Pole Parameter Values

To get a better understanding of how the parameters x_1, x_2, x_3 and x_4 influence the continuous torque of the EESM, sweeps of each parameter were performed. The parameters that were not swept were kept constant to the values in Table 4.1. Furthermore, the copper losses in the field winding were set to 40 W and the stator current amplitude was set to 18 A in Ansys Maxwell, just as for the parametric sweep. Hence, it is the continuous torque that is investigated.

The sweep results of the average torque are shown in Figure 4.2. Figure 4.2a shows that the rotor pole width, x_1, should neither be very thin nor very thick to achieve a high continuous torque. If the rotor poles are thin the number of turns of the field winding $N_{\mathrm{r,turns}}$ will be high, however, the iron will be saturated for lower currents. This results in a lower torque. For thick rotor poles the number of turns of the field winding $N_{\mathrm{r,turns}}$ will be low, resulting in a low magnetic flux linkage and a low torque.

In Figure 4.2b the average torque is shown as a function of the rotor pole height x_2. The continuous torque increases slightly when the height increases. This is because a higher rotor pole corresponds to more turns of the field winding, resulting in more magnetic flux and higher torque.

Figure 4.2c shows that the continuous torque is highly affected by the rotor pole shoe width, x_3. When x_3 increases the q-axis flux path will contain more iron according to Figure 2.1. Hence, the inductance L_q will increase and the reluctance torque, as well as the total torque, will decrease. However, for very thin rotor pole shoe widths the torque will decrease as well. The reason is that only a small part of the stator will be magnetized.

From Figure 4.2d it is clear that the height of the rotor pole shoe, x_4, does not affect the torque significantly.

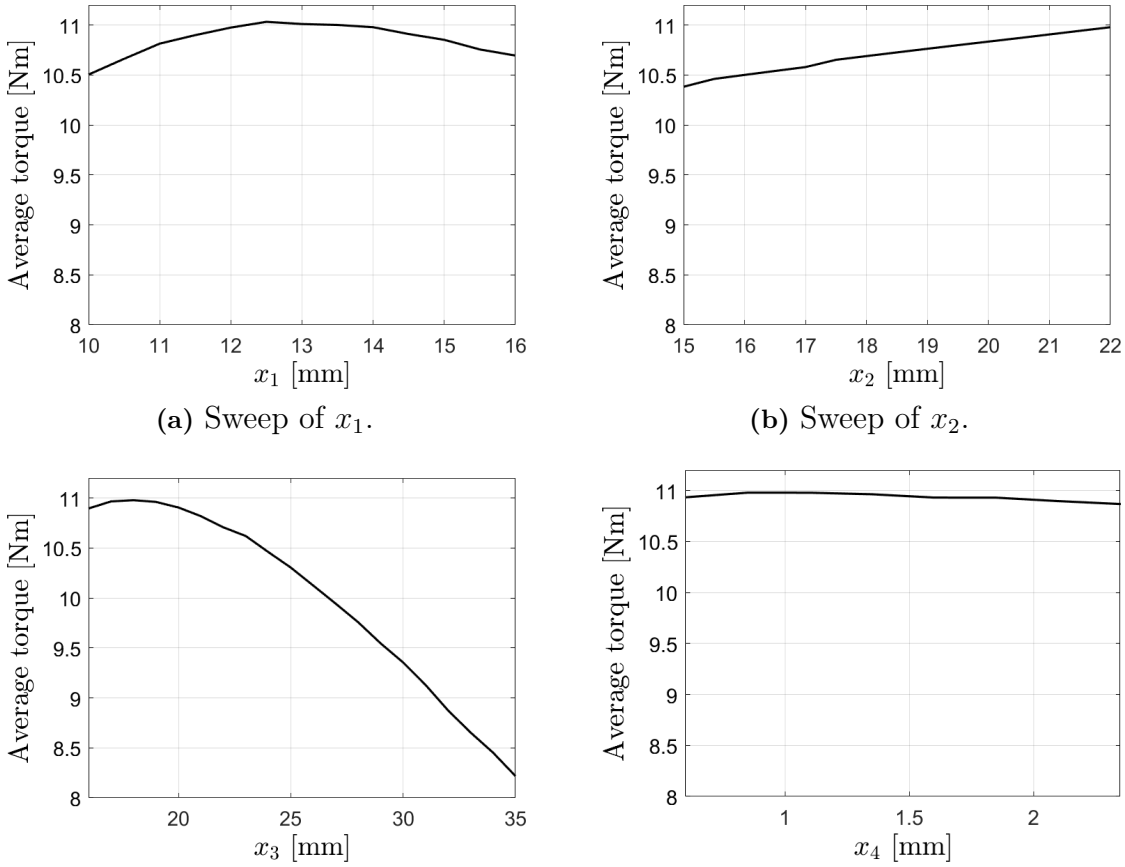

(a) Sweep of x_1.

(b) Sweep of x_2.

(c) Sweep of x_3.

(d) Sweep of x_4.

Figure 4.2: Influence of rotor pole parameters on the average continuous torque.

4.2 Continuous Torque of EESM-1

The copper loss minimization algorithm with penalty factors, described in Section 3.5.2, was applied on EESM-1 to investigate the torque output for different combinations of the stator currents and the field current. In Figure 4.3 the stator current amplitude and the field current are shown as functions of the average torque for different penalty factors. The highest torque shown in the figure is 22.2 Nm, since that is the upper limit of the defined operating region. The red dashed lines mark the currents and the corresponding torques that give a steady state temperature of 170 °C according to the thermal model. It should be noted that the highest continuous torque will be obtained when using the penalty factors $k_\mathrm{d} = k_\mathrm{q} = 0.3R_\mathrm{s}$ in Figure 4.3b. The torque at the temperature limit is then 12.6 Nm, the stator current amplitude is 21.3 A and the field current is 3.5 A. However, if the total copper loss is minimized, as for the case with $k_\mathrm{d} = k_\mathrm{q} = R_\mathrm{s}$ in Figure 4.3c, the maximum torque is only 8.8 Nm. Hence, the results show that the penalty factors affect the maximum continuous torque.

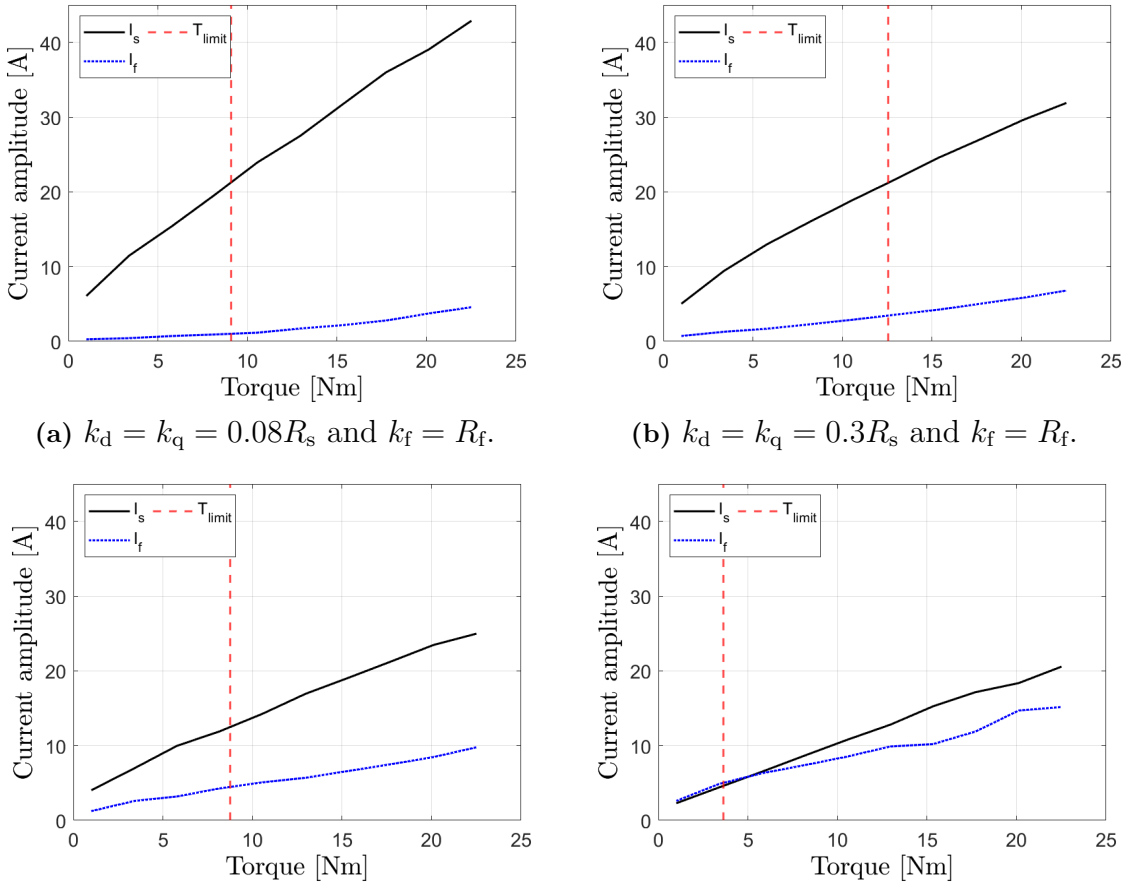

(a) $k_\mathrm{d} = k_\mathrm{q} = 0.08R_\mathrm{s}$ and $k_\mathrm{f} = R_\mathrm{f}$.

(b) $k_\mathrm{d} = k_\mathrm{q} = 0.3R_\mathrm{s}$ and $k_\mathrm{f} = R_\mathrm{f}$.

(c) $k_\mathrm{d} = k_\mathrm{q} = R_\mathrm{s}$ and $k_\mathrm{f} = R_\mathrm{f}$.

(d) $k_\mathrm{d} = k_\mathrm{q} = 8R_\mathrm{s}$ and $k_\mathrm{f} = R_\mathrm{f}$.

Figure 4.3: Stator current amplitude and field current at different torque values for different penalty factors k_d, k_q and k_f.

The results from the thermal simulations, when the maximum steady state temperature is 170 °C, are shown in Figure 4.4 for the different penalty factors discussed above. For low penalty factors on the stator currents, as for $k_\mathrm{d} = k_\mathrm{q} = 0.08R_\mathrm{s}$ in Figure 4.4a, the temperature limit is first reached in the stator windings. For high penalty factors on the stator currents, as for $k_\mathrm{d} = k_\mathrm{q} = R_\mathrm{s}$ and $k_\mathrm{d} = k_\mathrm{q} = 8R_\mathrm{s}$ in Figures 4.4c and 4.4d, the temperature limit is instead first reached in the field windings. However, for the case $k_\mathrm{d} = k_\mathrm{q} = 0.3R_\mathrm{s}$ in Figure 4.4b it is clear that the temperature limit is reached both in the stator windings and the field winding. Then the utilization of the currents is high. Hence, it is not possible to achieve much higher continuous torque than 12.6 Nm with EESM-1, relying on this thermal model. Even though the thermal model includes several assumptions, the obtained continuous torque value is very far away from the nominal torque of 20 Nm. Thus, it is not considered possible to reach 20 Nm even with another thermal model with fewer assumptions.

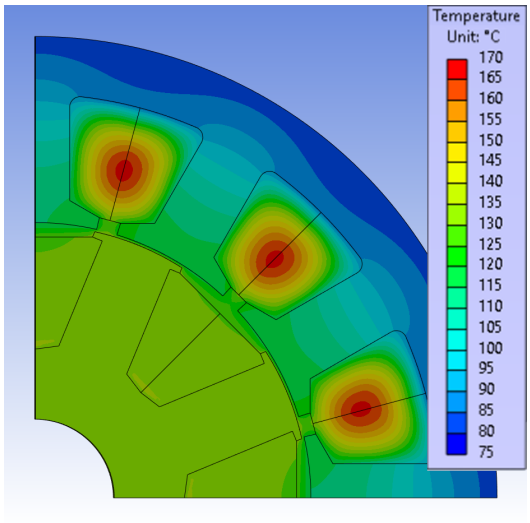

(a) $k_\mathrm{d} = k_\mathrm{q} = 0.08R_\mathrm{s}$ and $k_\mathrm{f} = R_\mathrm{f}$.

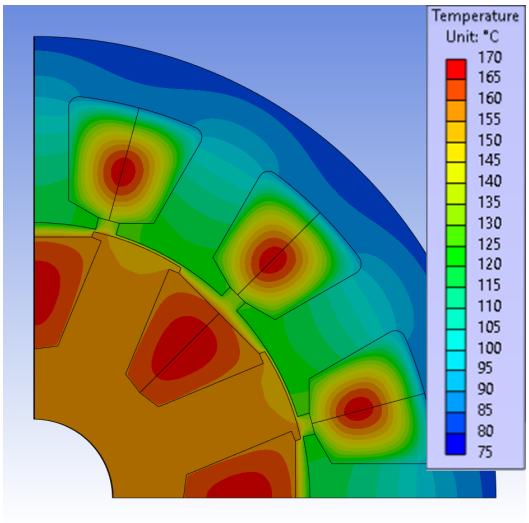

(b) $k_\mathrm{d} = k_\mathrm{q} = 0.3R_\mathrm{s}$ and $k_\mathrm{f} = R_\mathrm{f}$.

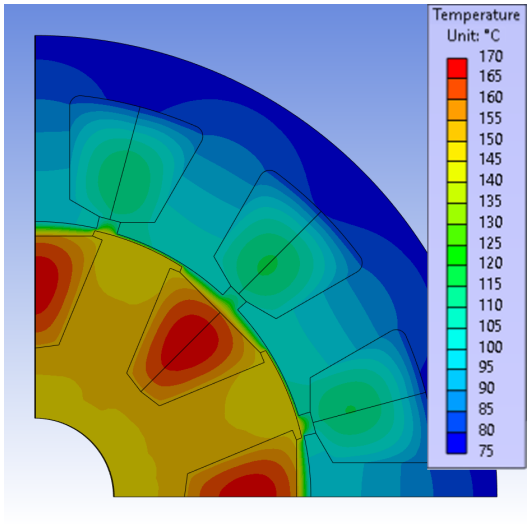

(c) $k_\mathrm{d} = k_\mathrm{q} = R_\mathrm{s}$ and $k_\mathrm{f} = R_\mathrm{f}$.

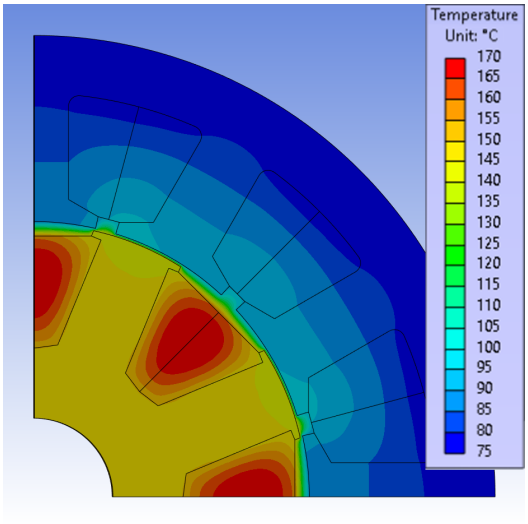

(d) $k_\mathrm{d} = k_\mathrm{q} = 8R_\mathrm{s}$ and $k_\mathrm{f} = R_\mathrm{f}$

Figure 4.4: Temperature distribution at the thermal limit, 170 °C, for different penalty factors k_d, k_q and k_f.

4.3 Modifications to Increase the Continuous Torque

From Section 4.2 it is clear that the model EESM-1 can not reach the nominal torque of 20 Nm in continuous operation without overheating. The geometry therefore has to be modified further. In this section it will be investigated if it is possible to increase the reluctance torque by increasing the curvature of the rotor pole shoe and how the stack length can be increased to reach a higher output torque.

4.3.1 Increase the Curvature of the Rotor Pole Shoe

In [13] it is described that the copper losses in the rotor are a bottleneck for the continuous operation of an EESM. To reduce the field current the saliency (L_d/L_q) of the motor should be increased and this is done by hindering the q-axis flux [13]. A simple way to do this is to increase the curvature of the rotor pole shoe [13].

Figure 4.5 shows three different geometries with different curvatures of the rotor pole shoe. The geometry EESM-1-C2 has a slightly larger curvature compared to EESM-1-C1 and EESM-1-C1 has a slightly larger curvature compared to EESM-1. The parameters x_1, x_2, x_3 and x_5 from Figure 3.3b are kept the same as for EESM-1 for all models and the parameter x_4 is changed. However, the differences are relatively small since x_4 should not be smaller than 0.6 mm. For all electromagnetic simulations performed in this section the stator current amplitude was set to 21.3 A and the field current was set to 3.5 A. From the investigation in Section 4.2 this combination of stator and field currents resulted in the highest continuous torque for EESM-1. MTPA was used to find the optimal current angles for the three designs.

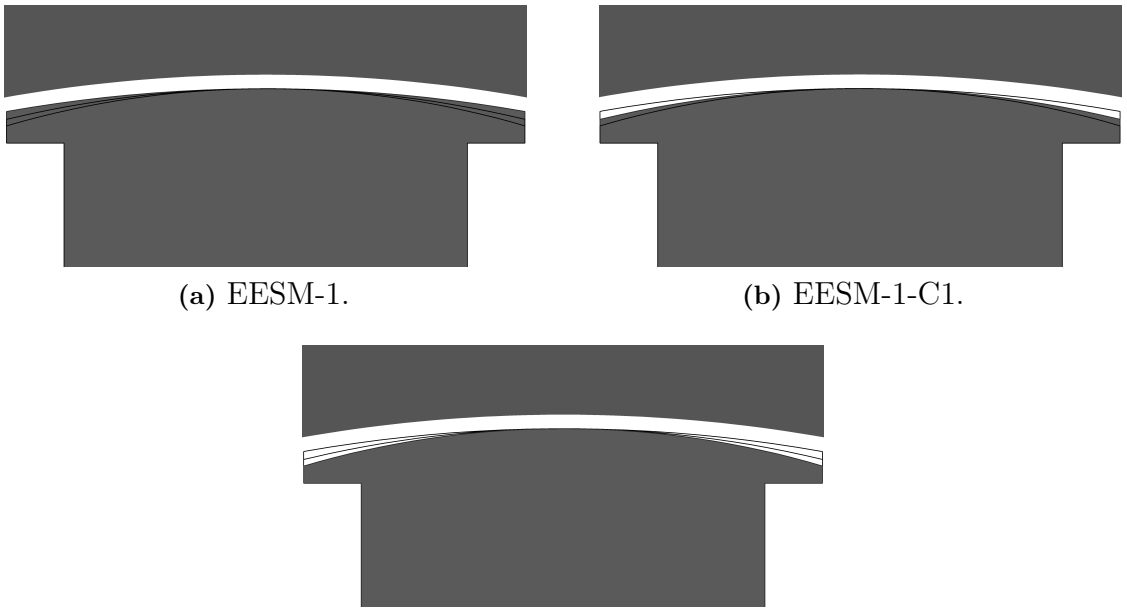

(a) EESM-1.

(b) EESM-1-C1.

(c) EESM-1-C2.

Figure 4.5: Three different models with different curvatures of the rotor pole shoe.

The results from the electromagnetic simulations of the models in Figure 4.5 are shown in Table 4.2. From the results it is clear that the highest continuous torque is obtained for EESM-1; hence, increasing the curvature of the rotor pole shoe did not increase the maximum continuous torque. Looking at the values of L_{q}, it can be seen that L_{q} indeed decreases when increasing the curvature and the saliency increases slightly. However, the total torque output decreases since an excessive curvature increases the overall air gap and the magnetization of the stator teeth is reduced. Moreover, it is clear that the core losses in both the stator and the rotor decrease when the curvature increases. One reason for this is that larger curvature

results in less magnetization of the iron. Another reason is that the THD of the induced phase voltage, the back EMF, is lower for larger curvatures and there will be less harmonics in the magnetic flux density. However, even though the core losses decrease it is not possible to increase the currents much because the hot spots are in the windings as shown in Figure 4.4. Properties such as torque ripple and power factor are relatively similar for the three models.

Table 4.2: Results from electromagnetic simulations for EESM models with different curvatures of the rotor pole shoe.

	EESM-1	**EESM-1-C1**	**EESM-1-C2**
Rotor pole shoe height x_4 (mm)	1.1	0.825	0.6
Field current (A)	3.5	3.5	3.5
Stator current amplitude (A)	21.3	21.3	21.3
Average torque (Nm)	12.6	12.1	11.8
Torque ripple (%)	23.2	25.6	28.5
Back EMF THD (%)	17.6	15.4	13.5
L_d (mH)	11.87	11.29	10.79
L_q (mH)	6.77	6.32	6.06
Saliency $L_\mathrm{d}/L_\mathrm{q}$	1.75	1.78	1.78
Core losses in stator (W)	205.6	193.2	190.1
Core losses in rotor (W)	28.7	22.5	18.7
Power factor	0.56	0.55	0.54

Since the differences between the investigated models EESM-1, EESM-1-C1 and EESM-1-C2 are relatively small a few more models with larger differences were investigated. For these models the rotor pole shoe width x_3 was increased to get a larger effect of changing the curvature. It was observed that for larger values of the rotor pole shoe width the torque will increase when increasing the curvature. The reason for this is that large values of x_3 will result in a large L_q inductance. When increasing the curvature of the rotor pole shoe L_q will decrease but there will still be enough iron in the rotor pole shoe to magnetize the stator teeth. If the maximum value of x_4 was set to 1.1 mm this phenomenon was shown for $x_3 \gtrapprox 27$ mm. However, as can be seen in Figure 4.2c the average torque drops quickly when x_3 increases above 20 mm. Therefore, even if the curvature increases for models with $x_3 \gtrapprox 27$ mm the continuous torque will still be lower compared to the torque of EESM-1.

Another trend that was observed was that the torque ripple and THD of the phase voltage decreased quite a lot when increasing the curvature for models with large values of x_3. The reason for this is that when the rotor rotates there is a more gradual transition between iron and air.

4.3.2 Increase the Stack Length

The continuous torque can be increased by increasing the stack length, L_stack, of the motor. However, it should be noted that this will reduce the continuous torque

density. To find a stack length with a continuous torque output of 20 Nm suitable stator current amplitude and field current had to be set. The stator current amplitude was decided from the MMF value $N_{\mathrm{s,turns}}I_{\mathrm{s}} = 778.8\,\mathrm{A} - \mathrm{turn}$. This is the same stator coil MMF that the PMSM has for the nominal torque output 20 Nm. By using the same stator coil MMF the comparison of the two motors is considered fair. The field current was decided using the thermal model and it was set to 3.5 A. In Section 4.2 it is shown that this field current does not overheat the EESM, even when the copper loss density is higher than it is for $N_{\mathrm{s,turns}}I_{\mathrm{s}} = 778.8\,\mathrm{A} - \mathrm{turn}$.

With these currents a stack length of 88 mm was required to reach the nominal torque 20 Nm, which is approximately 87 % longer than the reference PMSM. This model is called EESM-2 and updated design parameters are shown in Table 4.3. To avoid hitting the voltage limit within the constant torque region the winding configuration was changed slightly and for each phase the stator teeth are connected in parallel two and two. It should be noted that a consequence of this is that the stator current from the inverter will be higher, which might affect the power electronics negatively. However, this is not investigated further in this thesis.

Table 4.3: Design parameters for EESM-2.

Parameter	**Denotation**	**Value**	**Unit**
Stack length	L_{stack}	88	mm
Rotor pole body width	x_1	14	mm
Rotor pole body height	x_2	22	mm
Rotor pole shoe width	x_3	18	mm
Rotor pole shoe height	x_4	1.1	mm
Total rotor pole shoe height	x_5	1.89	mm
Number of turns of stator winding per tooth	$N_{\mathrm{s,turns}}$	51	-
Number of turns in rotor per pole	$N_{\mathrm{r,turns}}$	74	-
Rotor slot area	$A_{\mathrm{r,slot}}$	363.34	mm^2
Stator winding phase resistance (20 °C)	$R_{\mathrm{s,\ 20}}$	0.153	Ω
Stator winding phase resistance (120 °C)	R_{s}	0.212	Ω
Field winding resistance (20 °C)	$R_{\mathrm{f,\ 20}}$	3.318	Ω
Field winding resistance (120 °C)	R_{f}	4.612	Ω

Figure 4.6 shows the magnetic flux density distribution for EESM-2 at 20 Nm and 3500 rpm at two different time instants. The stator coil MMF is $778.8\,\mathrm{A} - \mathrm{turn}$, the field current is 3.5 A and MTPA has been used to find the current angle. In Figure 4.6a the flux density in the stator teeth for one of the phases exhibits a maximum flux density of 1.7 T. This is slightly lower than the saturation limit, which is close to 1.8 T. In Figure 4.6b the same stator teeth have a low flux density close to 0 T. The flux density in the rotor poles is approximately 1.3 T at all times. Since the flux density is below saturation in most parts of the motor this design is suitable for continuous operation at 20 Nm.

The rotor of EESM-2 rotates counterclockwise. In Figure 4.6 it is shown that the tip of each rotor pole shoe that first passes a new stator tooth exhibits a high magnetic

flux density of approximately 2 T. When a rotor pole rotates past a stator tooth the direction of the magnetic fields from the field winding and the stator winding will initially be in the same direction. This causes the first rotor pole shoe tip to be saturated. When the rotor pole is about to rotate away from the stator tooth the magnetic field from the corresponding stator winding changes direction and cancels part of the rotor flux. As a result, the rotor pole shoe tip that leaves the stator tooth last is not saturated.

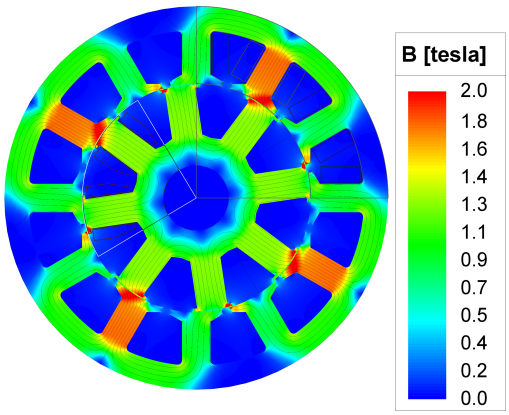

(a) High flux density in the stator teeth for one phase.

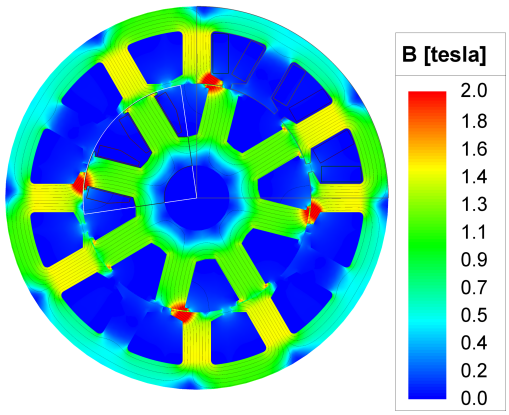

(b) Low flux density in the stator teeth for one phase.

Figure 4.6: Magnetic flux density for EESM-2 at 20 Nm at MTPA at two different time instants. The stator coil MMF is 778.8 A − turn, the field current is 3.5 A and the speed is 3500 rpm.

5

Performance and Cost Comparison of PMSM and EESM

In this chapter the performance, material cost and environmental cost of an EESM motor will be compared to the performance and cost of the reference PMSM. EESM-2 is the chosen EESM model for the performance comparison since it can reach the torque 20 Nm in continuous operation. To get a more comprehensive understanding of the two motors most quantities are investigated in the entire constant torque region in the speed range 1500 rpm to 3500 rpm. However, the actual operating region is mainly output torques in the range 12.6 Nm to 22.2 Nm. Thus, not much focus will be put on the maximum peak torques and the corresponding quantities. As before, all current values mentioned in this chapter are for the pure sinusoidal currents and pure DC currents that are used in Ansys Maxwell.

5.1 Non-Linear Characteristics

In this section, the non-linear characteristics obtained from FEM simulations of the reference PMSM and EESM-2 are presented. Flux linkages, inductances, electromagnetic torque and core losses are presented in the first and second quadrants in the dq-plane since that is where the motors operate. For the EESM the results are also shown for different field current levels. Similar results for an EESM designed for a traction application and optimized for high peak torque are presented in [2] and [12]. This section aims to show and explain the characteristics of an EESM optimized for high continuous torque and also to point out the similarities and differences between EESMs and PMSMs. Moreover, the results presented in this section are used for further analysis of efficiency maps and power factor maps.

5.1.1 Flux Linkages

Figure 5.1 shows the d-axis flux linkage Ψ_{d} and the q-axis flux linkage Ψ_{q} for different d-axis currents I_{d} and q-axis currents I_{q} for the reference PMSM. The black solid half circle represents the maximum stator current amplitude 53.9 A. It is clear that a high I_{d} current results in a high Ψ_{d}. Moreover, Ψ_{q} is mainly affected by I_{q} and a high value of I_{q} results in high Ψ_{q}. This corresponds to the theoretical calculations in Section 2.3.2, where $\Psi_{\mathrm{d}} = L_{\mathrm{d}} I_{\mathrm{d}} + \Psi_{\mathrm{RM}}$ and $\Psi_{\mathrm{q}} = L_{\mathrm{q}} I_{\mathrm{q}}$.

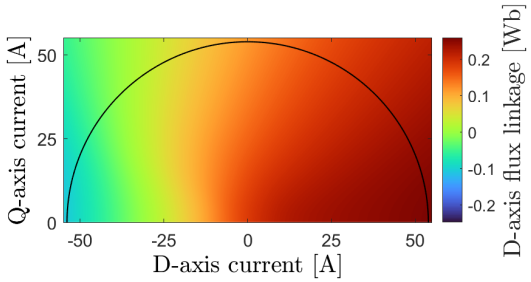

(a) D-axis flux Ψ_d. **(b)** Q-axis flux Ψ_q.

Figure 5.1: Flux linkages of the PMSM.

The d-axis flux linkages Ψ_d of EESM-2 for different values of the field current I_f are shown in Figure 5.2. The black solid half circle represents the maximum stator current amplitude 53.9 A. The flux Ψ_d is highly affected by both the I_d and I_f, since $\Psi_\mathrm{d} = L_\mathrm{d} I_\mathrm{d} + \Psi_\mathrm{RM} = L_\mathrm{d} I_\mathrm{d} + L_\mathrm{m} I_\mathrm{f}$. Furthermore, for high values of I_f the Ψ_d map looks quite similar to that of the PMSM.

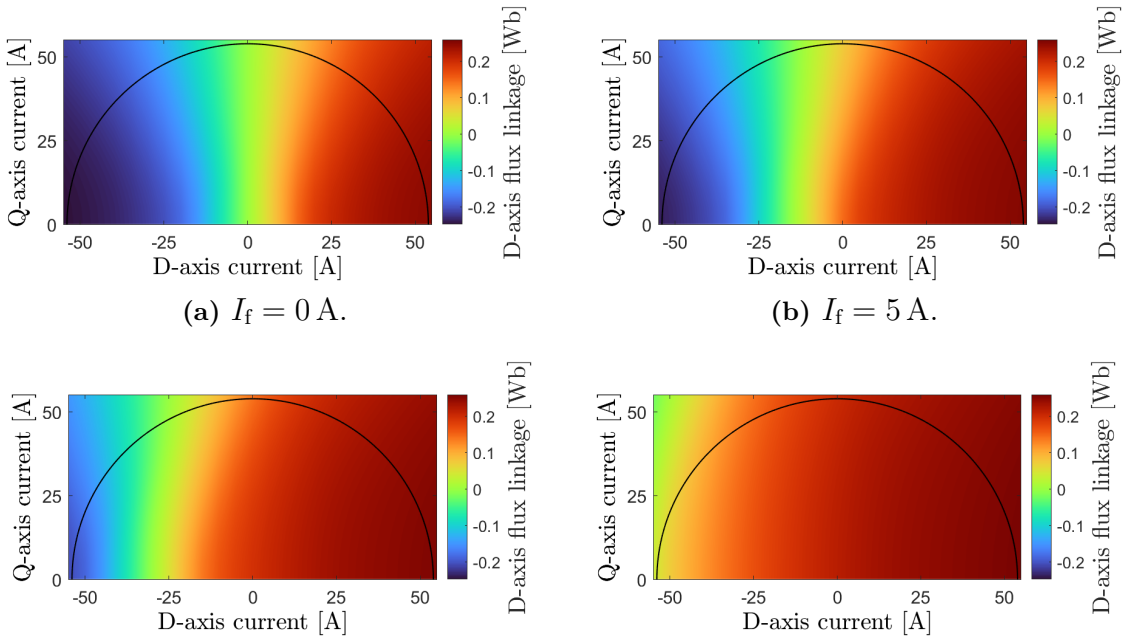

(a) $I_\mathrm{f} = 0$ A. **(b)** $I_\mathrm{f} = 5$ A.

(c) $I_\mathrm{f} = 10$ A. **(d)** $I_\mathrm{f} = 20$ A.

Figure 5.2: D-axis flux linkages Ψ_d of the EESM for different field currents I_f.

Figure 5.3 shows the q-axis flux linkage Ψ_q of EESM-2 in the dq-plane for different field currents. As for the PMSM, Ψ_q is mainly affected by the q-axis current I_q. However, when the field current increases the contour lines of Ψ_q move up towards the left in the dq-plane. This is probably because the L_q inductance decreases when the iron gets more saturated at high field currents. Furthermore, for all field currents, Ψ_q in the EESM is lower compared to in the PMSM. The reason is probably that the EESM has a slightly higher reluctance in the q-axis flux path.

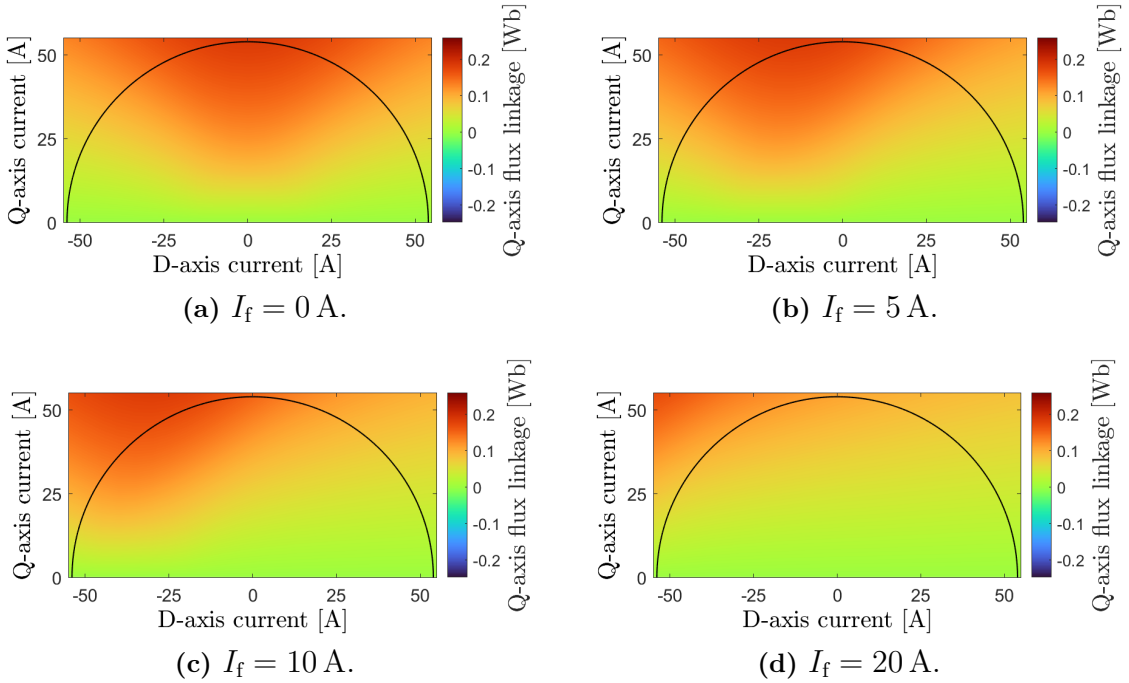

(a) $I_\mathrm{f} = 0\,\mathrm{A}$. **(b)** $I_\mathrm{f} = 5\,\mathrm{A}$.

(c) $I_\mathrm{f} = 10\,\mathrm{A}$. **(d)** $I_\mathrm{f} = 20\,\mathrm{A}$.

Figure 5.3: Q-axis flux linkages Ψ_q of the EESM for different field currents I_f.

5.1.2 Inductances

The d-axis and q-axis inductances L_d and L_q of the reference PMSM are shown in Figure 5.4 in the dq-plane. It is clear that both L_d and L_q peak at low current values; at higher current levels the iron gets saturated. Furthermore, it can be observed that $L_\mathrm{q} > L_\mathrm{d}$. This is because the permanent magnets are on the d-axis and those have low permeability causing a high reluctance and a low inductance.

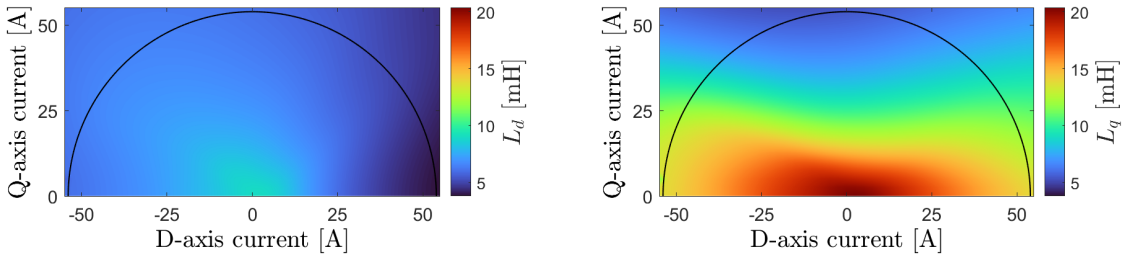

(a) D-axis inductance L_d. **(b)** Q-axis inductance L_q.

Figure 5.4: Inductances of the PMSM.

The Figures 5.5 and 5.6 show the inductance maps of EESM-2. Note that the scale on the colorbars differs from Figure 5.4. Figure 5.5 shows that the L_d inductance is highly affected by the currents I_d and I_f; high I_d and I_f currents saturate the d-axis flux path resulting in a low L_d inductance. However, from Figure 5.6 it can be seen that L_q is also slightly influenced by I_f and that a high value of I_f causes a decrease

of L_q as well. Hence, a high field current also saturates the iron in the q-axis flux path. It should be noted that for low field currents $L_d > L_q$ since there is more iron in the d-axis flux path and the iron is not yet saturated. However, L_d is more affected than L_q by saturation when the field current increases. At the maximum field current 20 A, $L_q > L_d$ for large values of I_d. However, for currents with a current angle close to 90°, or larger, the d-axis inductance L_d is still larger than the q-axis inductance L_q. This indicates that the rotor poles are not heavily saturated.

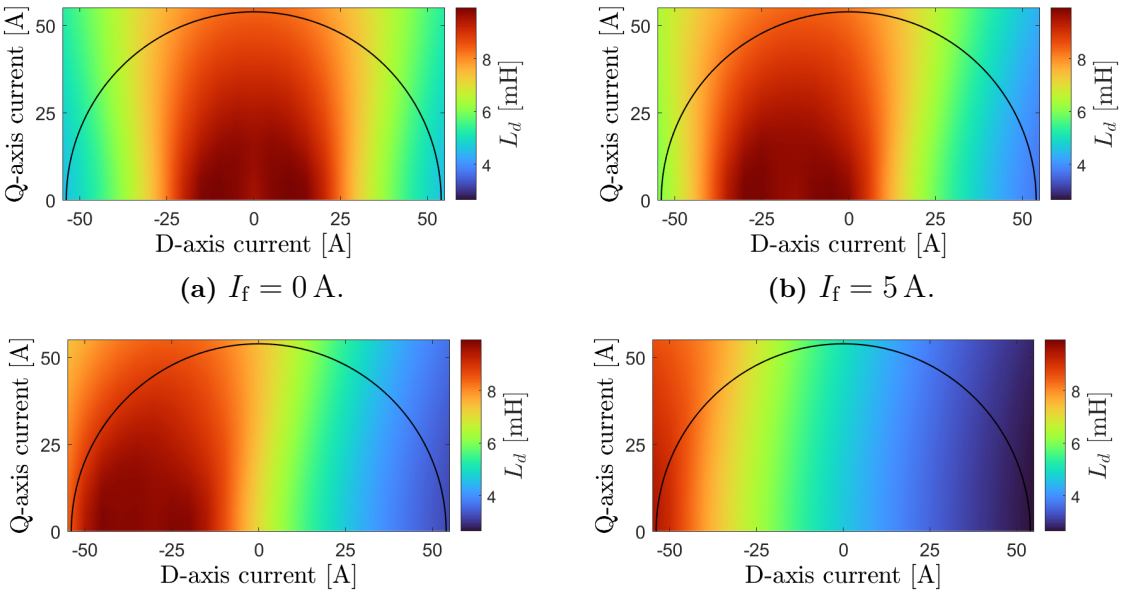

(a) $I_f = 0$ A. **(b)** $I_f = 5$ A.

(c) $I_f = 10$ A. **(d)** $I_f = 20$ A.

Figure 5.5: D-axis inductances L_d of the EESM for different field currents I_f.

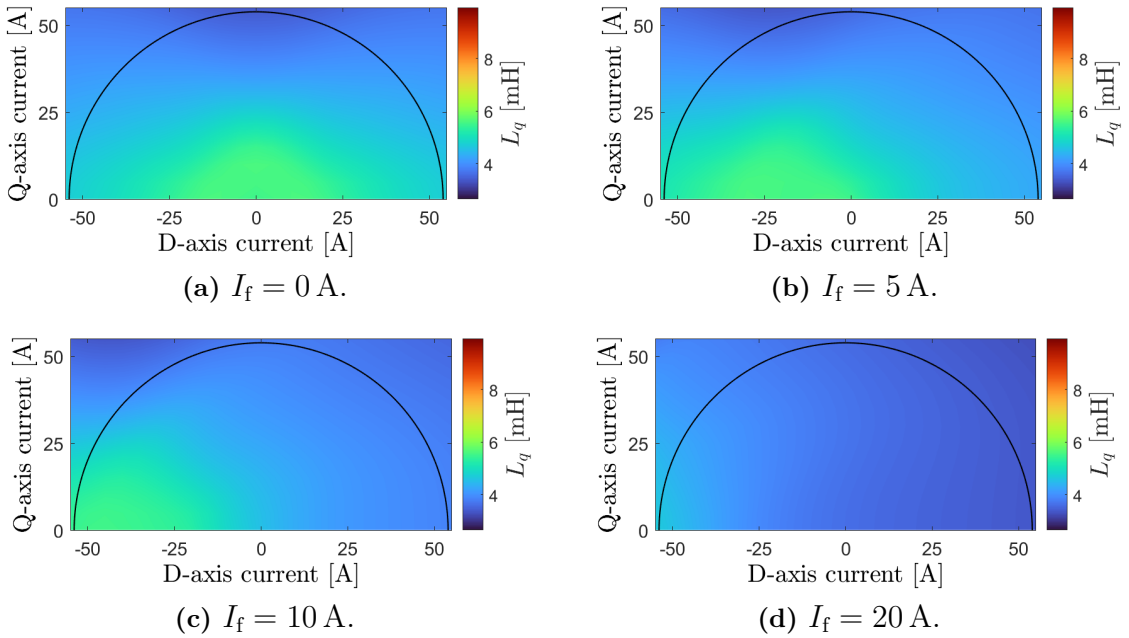

(a) $I_\mathrm{f} = 0\,\mathrm{A}$. (b) $I_\mathrm{f} = 5\,\mathrm{A}$.

(c) $I_\mathrm{f} = 10\,\mathrm{A}$. (d) $I_\mathrm{f} = 20\,\mathrm{A}$.

Figure 5.6: Q-axis inductances L_q of the EESM for different field currents I_f.

5.1.3 Electromagnetic Torque

The torque map for the PMSM is shown in Figure 5.7. The dotted line is the MTPA curve. The maximum torque for all stator current amplitudes is reached in the second quadrant. This is because $L_\mathrm{q} > L_\mathrm{d}$, requiring a negative value of I_d to generate positive reluctance torque.

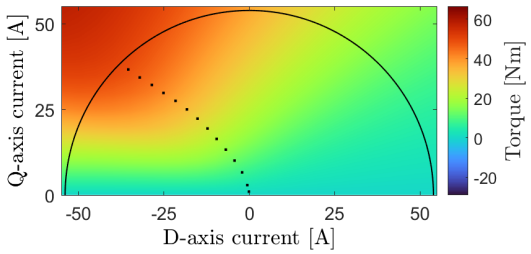

Figure 5.7: Torque map of the PMSM.

The torque maps at different field current levels for EESM-2 are shown in Figure 5.8. The MTPA curves are marked with a dotted black line in all torque maps. For $I_\mathrm{f} = 0\,\mathrm{A}$ the current angle is approximately 45°. When the field current increases the current angle at MTPA also increases. For $I_\mathrm{f} = 20\,\mathrm{A}$ the MTPA curve is no longer in the first quadrant, but in the second. This can partially be explained by looking at the inductances L_d and L_q. For a low field current $L_\mathrm{d} > L_\mathrm{q}$ and a positive value of I_d is needed to generate a positive reluctance torque and MTPA will be found in the first quadrant. According to equation (2.23) a negative value of I_d is needed when $L_\mathrm{q} > L_\mathrm{d}$. However, from Figures 5.5 and 5.6 it can be seen that L_d is still larger than L_q for current angles close to 90° when the field current is 20 A. The

reason why the MTPA angle still ends up in the second quadrant in Figure 5.8d is probably due to mutual inductances that were neglected in equation (2.18).

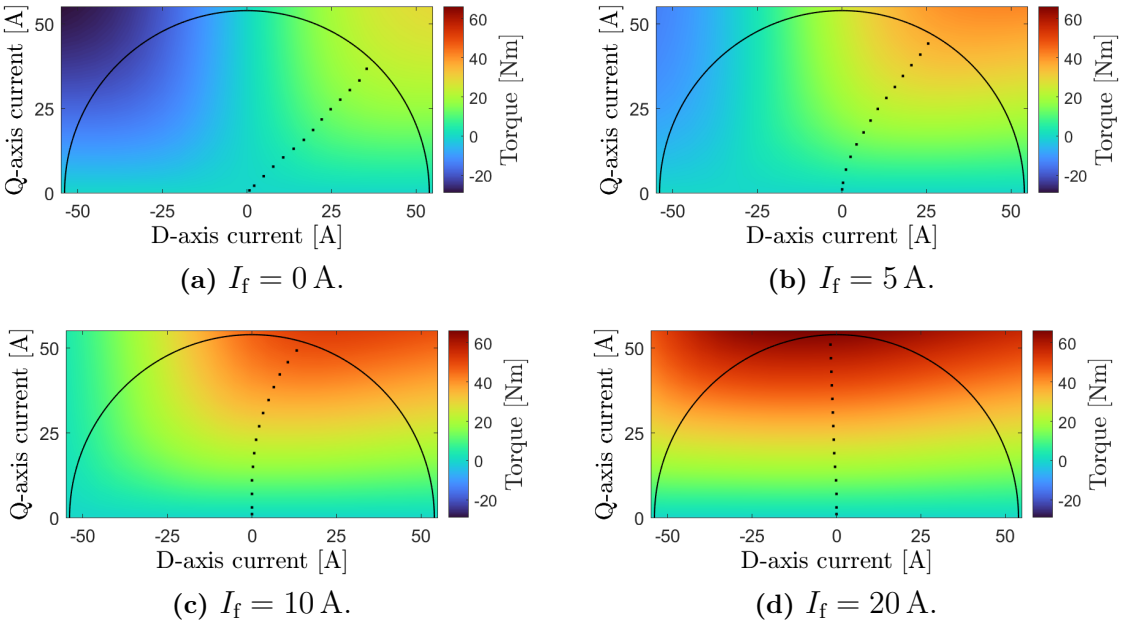

(a) $I_\mathrm{f} = 0\,\mathrm{A}$. **(b)** $I_\mathrm{f} = 5\,\mathrm{A}$.

(c) $I_\mathrm{f} = 10\,\mathrm{A}$. **(d)** $I_\mathrm{f} = 20\,\mathrm{A}$.

Figure 5.8: Torque maps of the EESM for different field currents I_f.

5.1.4 Core Losses

Core losses affect the efficiency and the temperature of an electric motor, therefore it is important to understand when the core losses are high. The core losses in the dq-plane are shown for the reference PMSM in Figure 5.9. It can be observed that maximum core losses occur for high currents and when the d-axis current I_d is positive. This is because positive values of I_d cause a magnetic flux that aligns with the rotor flux, resulting in higher magnetic flux density and subsequently higher core losses. The core loss map is at the speed 3500 rpm. For lower speeds, the map will look similar but the core losses will be lower.

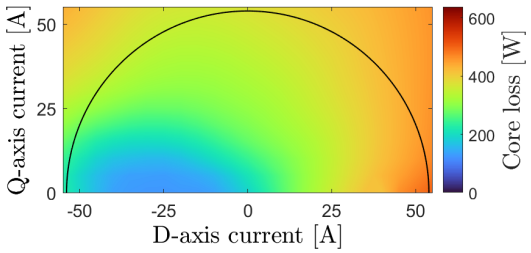

Figure 5.9: Core loss map of the PMSM at 3500 rpm.

The core losses at different field currents for EESM-2 are shown in Figure 5.10. The speed is 3500 rpm. Just as for the PMSM, the rotor flux and the flux caused by a positive current I_d are in the same direction. Thus, when the field current is close

to 0 A the current I_d should also be close to 0 A to obtain low core losses, which can be observed in Figure 5.10a. When the field current increases a negative value of I_d is required to cancel some of the rotor flux. Thus, contrary to the PMSM, tuning the currents to obtain low core losses is possible. Furthermore, it can be observed that the losses are slightly larger for EESM-2 compared to the reference PMSM. The main reason for this is that EESM-2 is longer and contains more iron compared to the PMSM.

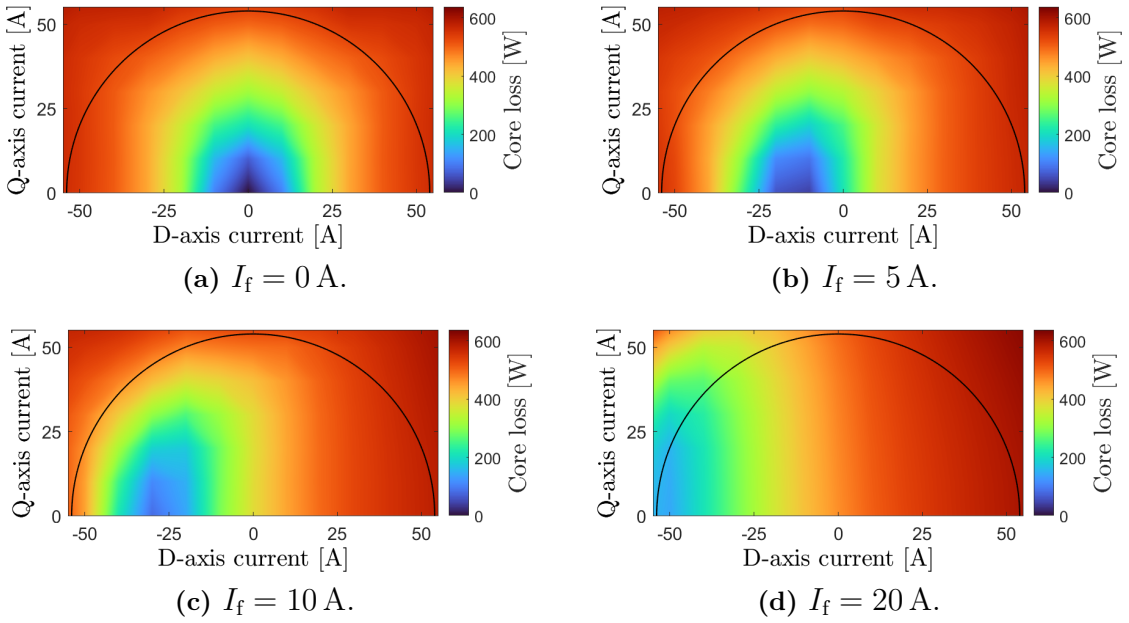

(a) $I_f = 0$ A. **(b)** $I_f = 5$ A.

(c) $I_f = 10$ A. **(d)** $I_f = 20$ A.

Figure 5.10: Core loss maps of the EESM for different field currents I_f.

5.2 Optimized Currents

Since the motors work in the constant torque region the required current for a specific torque output will be similar for different speeds. Thus, in this section, the optimized currents are only shown for the nominal speed 3500 rpm. Additionally, the optimized currents are shown for torque values ranging from 2 Nm to the maximum peak torque achievable. Lower torque values than 2 Nm are not considered important since the motors never operate at such low torques.

For the PMSM, copper loss minimization was performed according to Section 3.5.1 to find the optimal stator currents. The current amplitude as a function of torque output is shown in Figure 5.11. The red dashed line shows that the temperature limit 170 °C is reached when the current is 21.6 A and the torque is 23.2 Nm. According to previous thermal measurements of the PMSM the thermal limit is reached when the current amplitude is 23.73 A when the current contains harmonics and disturbances. According to the discussion in Section 3.2.5 this is assumed to correspond to a pure sinusoidal current in Ansys Maxwell with an amplitude of $23.73/1.1\,\text{A} \approx 21.6\,\text{A}$.

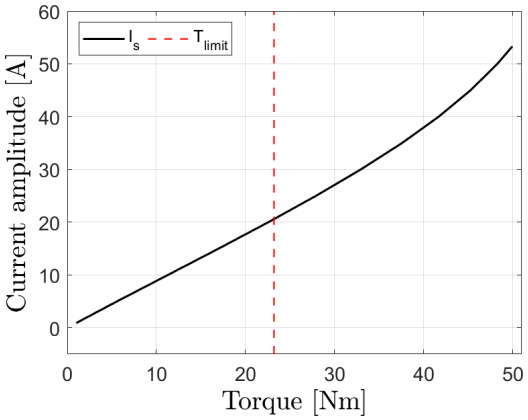

Figure 5.11: Stator current amplitude at MTPA for different torque values for the PMSM.

The optimized currents for EESM-2 were determined using the iterative copper loss minimization algorithm described in Section 3.5.2. The stator current amplitude I_s, the d-axis current I_d, the q-axis current I_q and the field current I_f are shown for different penalty factors in Figure 5.12. Contrary to the PMSM, the possibility of adjusting the rotor flux makes it possible to tune the currents for each operating point. With low penalty factors applied to the stator currents, the stator current amplitude increases relatively fast and reaches the current limit before the field current limit is reached. Conversely, higher penalty factors on the stator currents result in the stator current amplitude being slightly lower and the field current being a bit higher at each operating point. The d-axis current I_d and the q-axis current I_q also differ at each operating point depending on the penalty factors. For low penalty factors on the stator currents the field current is low and from the torque maps in Figure 5.8 this corresponds to a higher value of I_d at MTPA. Hence, the current I_d is relatively high for the penalty factors $k_d = k_q = 0.08R_s$ and $k_d = k_q = 0.3R_s$ in Figures 5.12a and 5.12b. When the stator current limit is reached the field current starts to increase more rapidly, causing I_d to decrease quickly. For higher penalty factors on the stator current, on the other hand, the field current is higher resulting in a lower value of I_d. At the maximum peak torque the currents I_s, I_d, I_q and I_f are the same for all different penalty factors since a unique current combination is required to reach that torque.

Additionally, the red dashed line in the graphs in Figure 5.12 shows the maximum continuous torque and the corresponding currents at 170 °C. As discussed in Section 4.2, the selection of penalty factors influences the maximum continuous torque. For the investigated penalty factors the maximum continuous torque is obtained for $k_d = k_q = 0.3R_s$. The continuous torque is then 25.4 Nm, the stator current amplitude is 39.1 A and the field current is 3.7 A. This torque output is higher than the maximum continuous torque of the PMSM; thus, the thermal model suggests that EESM-2 could be made slightly shorter and still fulfill the torque output requirement. For higher penalty factors on the stator currents more copper losses will be distributed in the field windings. From Figures 5.12c and 5.12d it can be seen that the maximum continuous torque is then lower. Thus, it is shown that if the motor is cooled on

the outside of the stator more losses should be distributed in the stator windings to achieve high continuous torque. Furthermore, the temperature distributions for the different penalty factors are similar as in Figure 4.4 where the temperature distributions for EESM-1 are shown for different penalty factors.

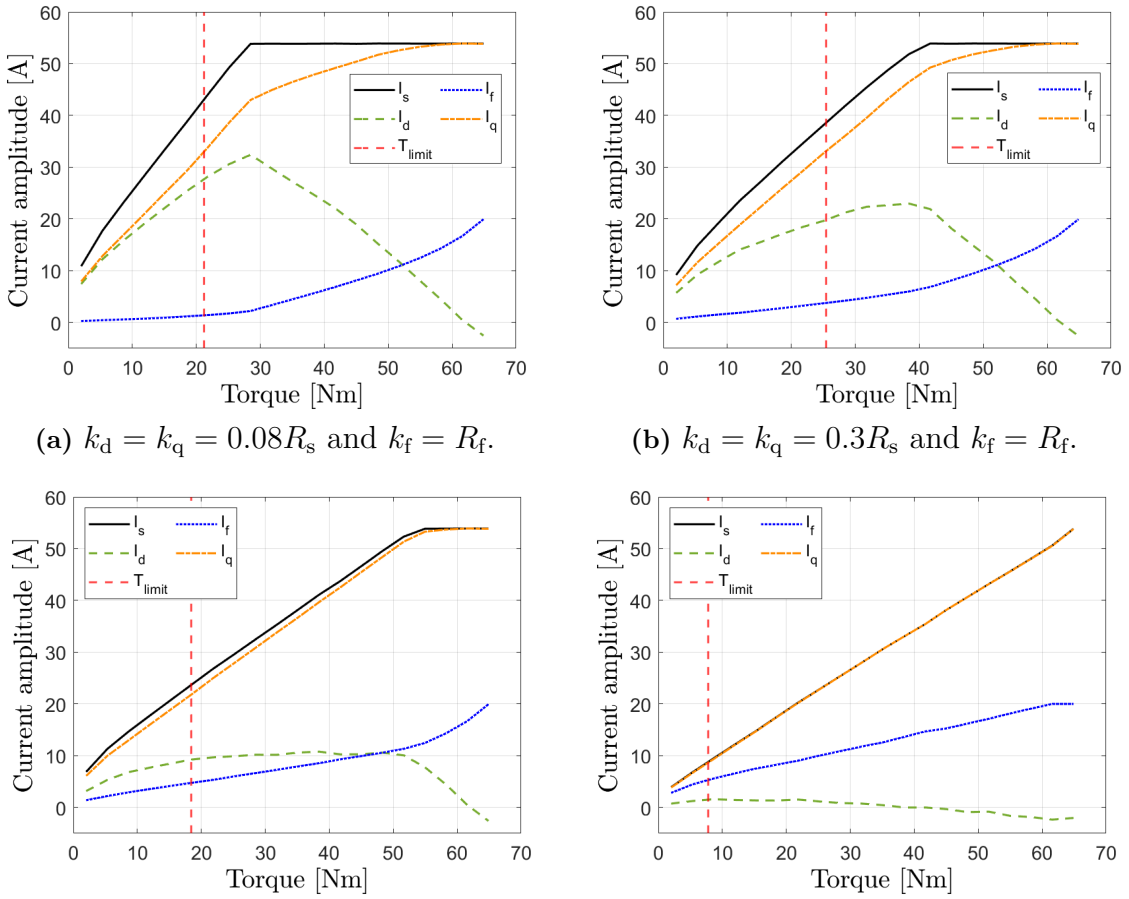

(a) $k_\mathrm{d} = k_\mathrm{q} = 0.08R_\mathrm{s}$ and $k_\mathrm{f} = R_\mathrm{f}$.

(b) $k_\mathrm{d} = k_\mathrm{q} = 0.3R_\mathrm{s}$ and $k_\mathrm{f} = R_\mathrm{f}$.

(c) $k_\mathrm{d} = k_\mathrm{q} = R_\mathrm{s}$ and $k_\mathrm{f} = R_\mathrm{f}$.

(d) $k_\mathrm{d} = k_\mathrm{q} = 8R_\mathrm{s}$ and $k_\mathrm{f} = R_\mathrm{f}$.

Figure 5.12: Stator current amplitude and field current at different torque values for different penalty factors k_d, k_q and k_f.

5.3 Efficiency and Power Factor

Efficiency and power factor are both important measurements of the performance of an electrical machine. The efficiency and the power factor of both motors are dependent on the speed of the motor. Therefore, this section will present the efficiency and power factor of the two motors across the entire speed range, spanning from 1500 rpm to 3500 rpm. As for the optimized currents above, the shown torque values will be between 2 Nm and the maximum peak torque possible. Furthermore, the operating region refers to operating points with torque values between 12.6 Nm and 22.2 Nm. This is where the motor most often operates according to Section 3.1.

5.3.1 Efficiency Maps

The efficiency map of the PMSM is shown in Figure 5.13. For each operating point copper loss minimization has been used according to Section 3.5.1. The gray horizontal lines mark the limits 12.6 Nm and 22.2 Nm of the operating region. It is clear that the efficiency is highest close to the nominal operating point at 20 Nm and 3500 rpm. However, the efficiency is rather high in the entire operating region; in most parts of the operating region it is over 92 %.

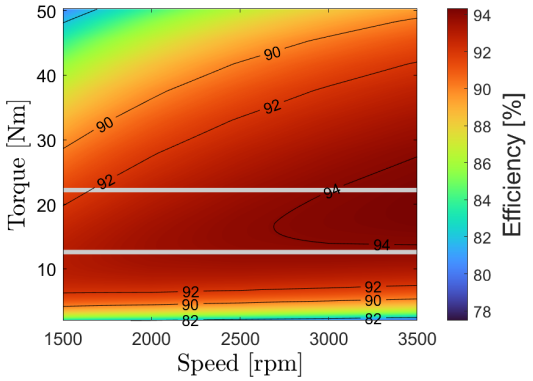

Figure 5.13: Efficiency map of the PMSM.

Figure 5.14 shows the efficiency maps of EESM-2 for different penalty factors. For all penalty factors the efficiency is higher for higher speeds. Furthermore, for all penalty factors the efficiency in the operating region, as well as the maximum efficiency, is lower compared to the PMSM. The main reason for this is most probably that the EESM has additional copper losses in the rotor. The EESM also has higher core losses and stator copper losses since it is longer than the PMSM.

It is important to acknowledge that the efficiency maps will vary significantly depending on the chosen penalty factors. The efficiency in the operating region is highest for the case $k_\mathrm{d} = k_\mathrm{q} = R_\mathrm{s}$. This outcome is reasonable since those penalty factors will limit the total copper loss. According to Figure 5.12c it is possible to optimize the currents to obtain high efficiency in most of the operating region without overheating. However, for torque values close to 20 Nm slightly lower penalty factors on the stator currents are required to avoid overheating.

From Figure 5.14 it can also be observed that for low penalty factors, $k_\mathrm{d} = k_\mathrm{q} = 0.08R_\mathrm{s}$ and $k_\mathrm{d} = k_\mathrm{q} = 0.3R_\mathrm{s}$, the efficiency will vary quite a lot when going from low torque to high torque at a fixed speed. In Figure 5.14a the efficiency is relatively low for torque values close to 30 Nm and in Figure 5.14b the efficiency is relatively low for torque values close to 40 Nm. From Figures 5.12a and 5.12b it is clear that those torque values correspond to the highest values of the d-axis current I_d. As discussed in Section 5.1.4 high values of I_d correspond to high core losses. The same phenomenon is not visible for higher penalty factors since the current I_d is relatively small for all torque values, which can be seen in Figures 5.12c and 5.12d. This result indicates that it may be necessary to also include core losses in the current optimization algorithm.

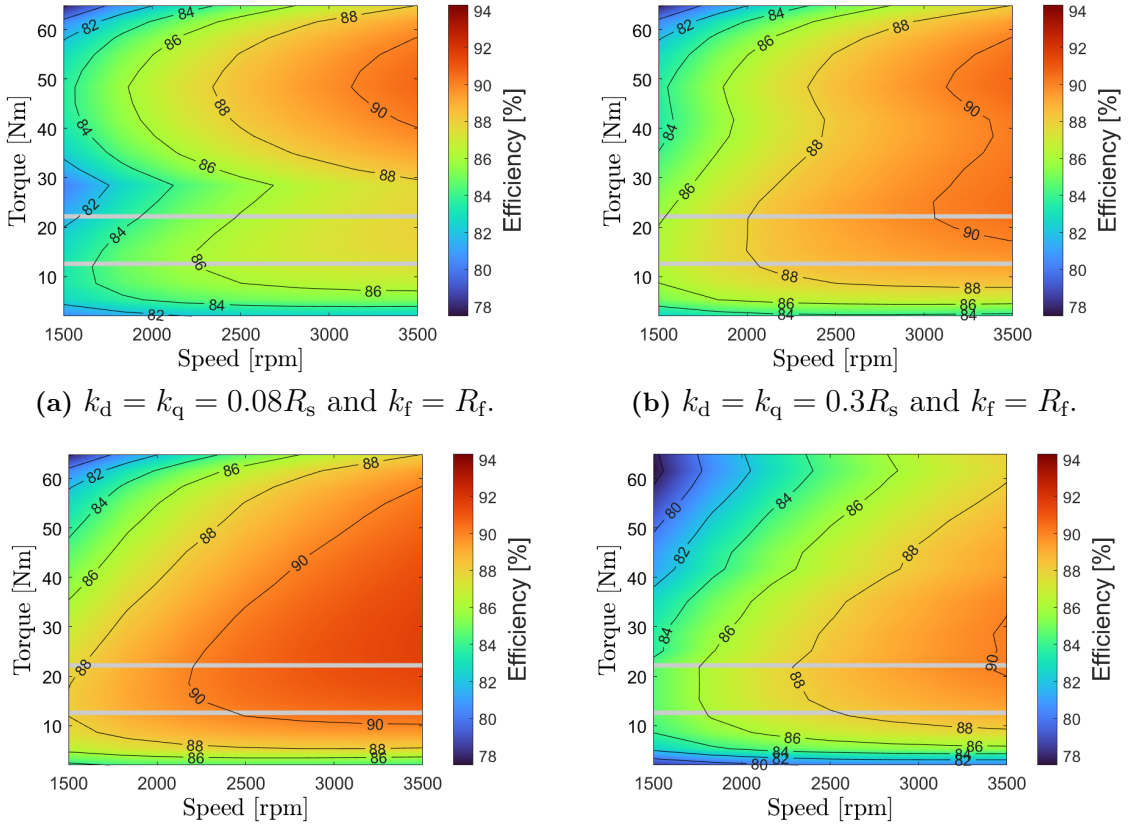

(a) $k_\mathrm{d} = k_\mathrm{q} = 0.08 R_\mathrm{s}$ and $k_\mathrm{f} = R_\mathrm{f}$.

(b) $k_\mathrm{d} = k_\mathrm{q} = 0.3 R_\mathrm{s}$ and $k_\mathrm{f} = R_\mathrm{f}$.

(c) $k_\mathrm{d} = k_\mathrm{q} = R_\mathrm{s}$ and $k_\mathrm{f} = R_\mathrm{f}$.

(d) $k_\mathrm{d} = k_\mathrm{q} = 8 R_\mathrm{s}$ and $k_\mathrm{f} = R_\mathrm{f}$.

Figure 5.14: Efficiency maps of EESM-2 for different penalty factors k_d, k_q and k_f.

Finally, the obtained efficiencies at the nominal operating point for the PMSM and EESM-2 are shown in Table 5.1. As discussed above, the PMSM exhibits higher efficiency compared to the EESM. The maximum efficiency of the EESM in the nominal operating point is obtained for the penalty factors $k_\mathrm{d} = k_\mathrm{q} = R_\mathrm{s}$ and it is 91.46 %, which is more than 2.8 percentage points lower compared to the PMSM. However, to not overheat the motor during nominal operation the penalty factors on the stator currents have to be slightly lower than $k_\mathrm{d} = k_\mathrm{q} = R_\mathrm{s}$. Thus, the maximum efficiency of the EESM in the nominal operating point during continuous operation will probably be slightly lower than 91.46 %. The exact value depends on the thermal results and due to assumptions in the thermal model this value is not determined in this project.

Table 5.1: Efficiency at the nominal operating point with a torque of 20 Nm and a speed of 3500 rpm for the two motors. For the EESM, the efficiencies obtained for the different investigated penalty factors are shown.

Motor type	Optimization strategy	Efficiency (%)
PMSM	MTPA	94.30
EESM	$k_d = k_q = 0.08R_s$ and $k_f = R_f$	87.79
	$k_d = k_q = 0.3R_s$ and $k_f = R_f$	90.29
	$k_d = k_q = R_s$ and $k_f = R_f$	91.46
	$k_d = k_q = 8R_s$ and $k_f = R_f$	90.02

5.3.2 Power Factor Maps

The power factor map of the PMSM is shown in Figure 5.15. It is clear that the power factor is highest for low torque values and then decreases slightly when the torque increases. This is because the motor gets saturated for higher currents. In the entire operating region the power factor is above 0.9. As before, the operating region is torque values between 12.6 Nm and 22.2 Nm and it is marked with gray solid lines.

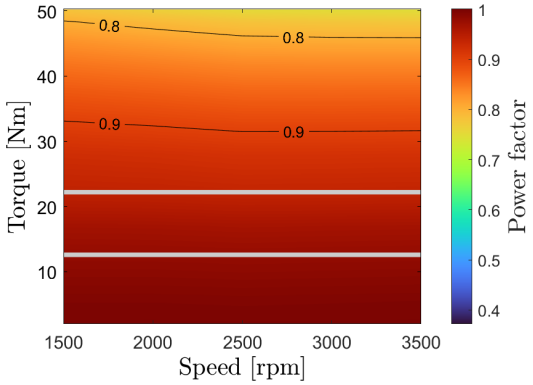

Figure 5.15: Power factor map of the PMSM.

Figure 5.16 shows the power factor maps of EESM-2 for different penalty factors. The power factor is highly affected by the penalty factors. For the penalty factors $k_d = k_q = 0.08R_s$, $k_d = k_q = 0.3R_s$ and $k_d = k_q = R_s$ the power factor will be rather low, except for high torque values, which can be seen in the Figures 5.16a, 5.16b and 5.16c. This can be explained by the optimized currents in Figure 5.12. For the penalty factors $k_d = k_q = 0.08R_s$, $k_d = k_q = 0.3R_s$ and $k_d = k_q = R_s$ the stator current limit is reached before the field current limit. Before the stator current limit is reached the field current will be rather low, resulting in a quite low torque output compared to the stator current amplitude. This will result in a low active stator power p_s, which also can be seen from equation (2.21). Then also the power factor will be low. When the stator current limit is reached the field current will start to increase more rapidly. This will cause the torque output to increase, even though the stator current amplitude remains the same, and the active power will increase accordingly. Hence, the power factor will be high for high torque values.

For the penalty factors $k_\mathrm{d} = k_\mathrm{q} = 8R_\mathrm{s}$ the power factor is rather high, above 0.9, in the entire investigated constant torque region. This can be seen in Figure 5.16d. The reason is that the stator current amplitude is rather low compared to the torque output, instead the field current is high. According to equation (2.21) that will result in a high active power p_s and also a high power factor.

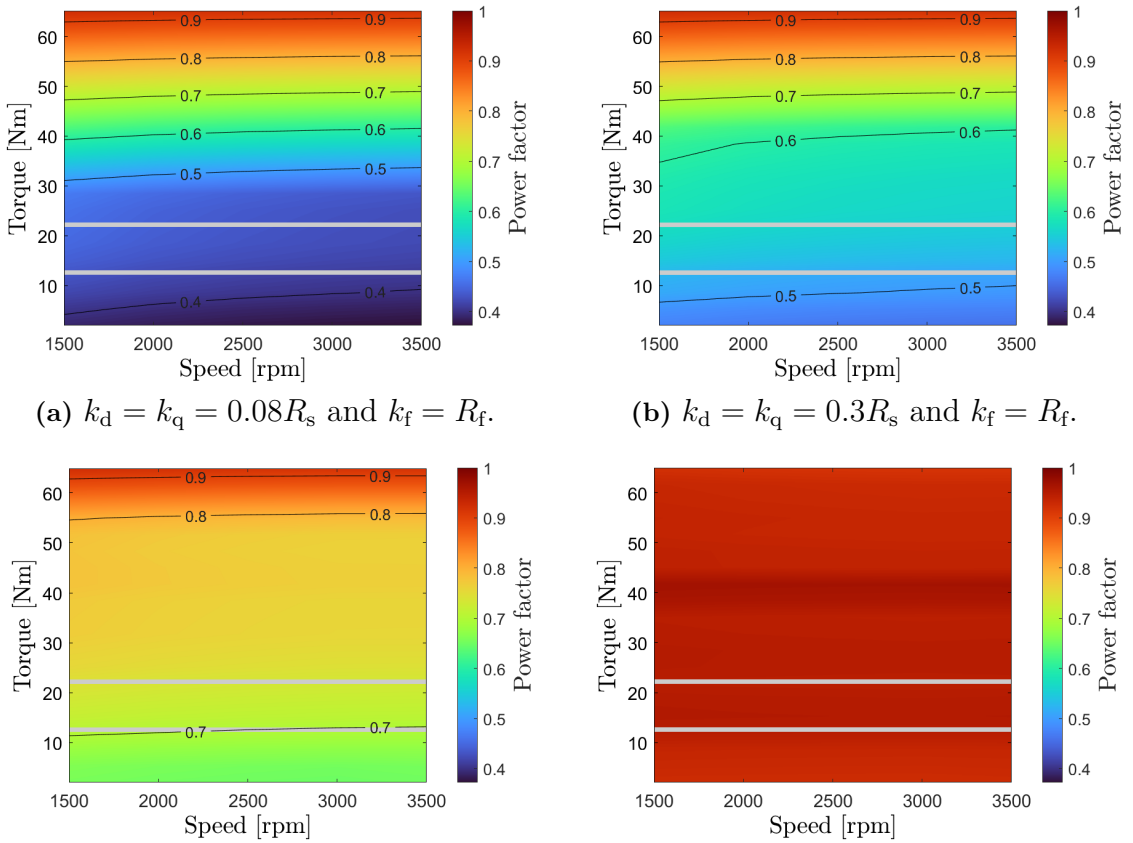

(a) $k_\mathrm{d} = k_\mathrm{q} = 0.08R_\mathrm{s}$ and $k_\mathrm{f} = R_\mathrm{f}$.

(b) $k_\mathrm{d} = k_\mathrm{q} = 0.3R_\mathrm{s}$ and $k_\mathrm{f} = R_\mathrm{f}$.

(c) $k_\mathrm{d} = k_\mathrm{q} = R_\mathrm{s}$ and $k_\mathrm{f} = R_\mathrm{f}$.

(d) $k_\mathrm{d} = k_\mathrm{q} = 8R_\mathrm{s}$ and $k_\mathrm{f} = R_\mathrm{f}$.

Figure 5.16: Power factor of EESM-2 for different penalty factors k_d, k_q and k_f.

The power factors at the nominal operating point for both motors are shown in Table 5.2. For the EESM only the case with the penalty factors $k_\mathrm{d} = k_\mathrm{q} = 8R_\mathrm{s}$ resulted in a power factor as high as for the PMSM. Hence, it can be concluded that a high field current is needed for a high power factor in the constant torque region. It is important to remember that such high field current is not possible to use in continuous operation if only stator cooling is used. Thus, the power factor in continuous operation will be relatively low compared to the PMSM. Since the currents and the voltage are below the limits a low power factor in the constant torque region mainly results in higher losses in the stator inverter. However, by using penalty factors close to $k_\mathrm{d} = k_\mathrm{q} = R_\mathrm{s}$ it is probable that the total efficiency of the drive line is relatively high anyways.

Table 5.2: Power factor at the nominal operating point with a torque of 20 Nm and a speed of 3500 rpm for the two motors. For the EESM, the power factors obtained for the different investigated penalty factors are shown.

Motor type	Optimization strategy	Power factor
PMSM	MTPA	0.95
EESM	$k_\mathrm{d} = k_\mathrm{q} = 0.08R_\mathrm{s}$ and $k_\mathrm{f} = R_\mathrm{f}$	0.42
	$k_\mathrm{d} = k_\mathrm{q} = 0.3R_\mathrm{s}$ and $k_\mathrm{f} = R_\mathrm{f}$	0.54
	$k_\mathrm{d} = k_\mathrm{q} = R_\mathrm{s}$ and $k_\mathrm{f} = R_\mathrm{f}$	0.73
	$k_\mathrm{d} = k_\mathrm{q} = 8R_\mathrm{s}$ and $k_\mathrm{f} = R_\mathrm{f}$	0.95

5.4 Torque Ripple and Harmonics

Torque ripple is not that significant for an air compressor. However, it is still desirable to avoid excessive torque ripple since that causes noise and mechanical stress. Therefore, the torque ripple, torque harmonics and back EMF harmonics are investigated further in this section. A smaller time step of 20 µs has been used for all the simulations in this section to increase the visibility of the plots. However, as discussed in Section 3.2.5 this does not affect the values of average torque, torque ripple or THD noticeably.

5.4.1 Torque Ripple and Harmonics at the Nominal Torque

Figure 5.17 shows the torque waveforms for one electric period for both the reference PMSM and EESM-2 at the mechanical speed 3500 rpm and an average torque of 20 Nm. For the PMSM, MTPA has been used to determine the stator currents. For the EESM the copper loss minimization algorithm with the penalty factors $k_\mathrm{d} = k_\mathrm{q} = 0.3R_\mathrm{s}$ has been used to determine the stator currents and the field current. The torque ripple of the PMSM is 59.0 % and the EESM has a lower torque ripple of 28.4 %.

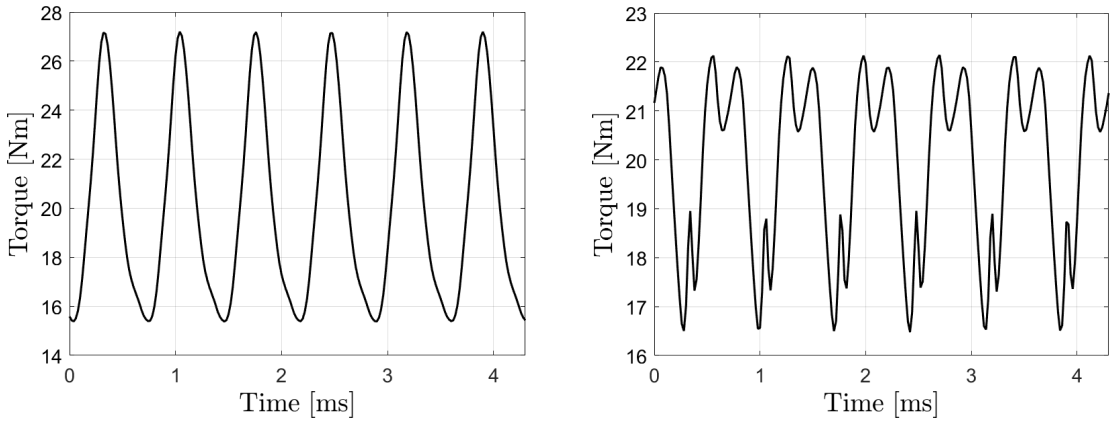

(a) PMSM. **(b)** EESM.

Figure 5.17: Torque ripple at the nominal operating point for one electric period for the reference PMSM and EESM-2.

Furthermore, by looking at Figures 5.17a and 5.17b it is clear that it is the sixth harmonic, with a frequency of 1400 Hz, that is most prominent. This can also be seen from the frequency spectra of the torque waveforms in Figures 5.18a and 5.18b. Moreover, both torque waveforms contain higher order harmonics. This is especially visible for the torque waveform of the EESM in Figure 5.17b and it can also be seen in the frequency spectrum in Figure 5.18b. These higher order harmonics are all of order $n = 6k$ ($k = 1, 2, 3...$), which corresponds to the theory discussed in Section 2.6.1. The fact that the electromagnetic torque of the EESM contains slightly more higher order harmonics should not be a major problem for the mechanics. From the swing equation in equation (2.24) it can be seen that the inertia will slow down the rate at which the rotor can change its speed. Thus, the load will not notice all the changes in the electromagnetic torque caused by high order harmonics.

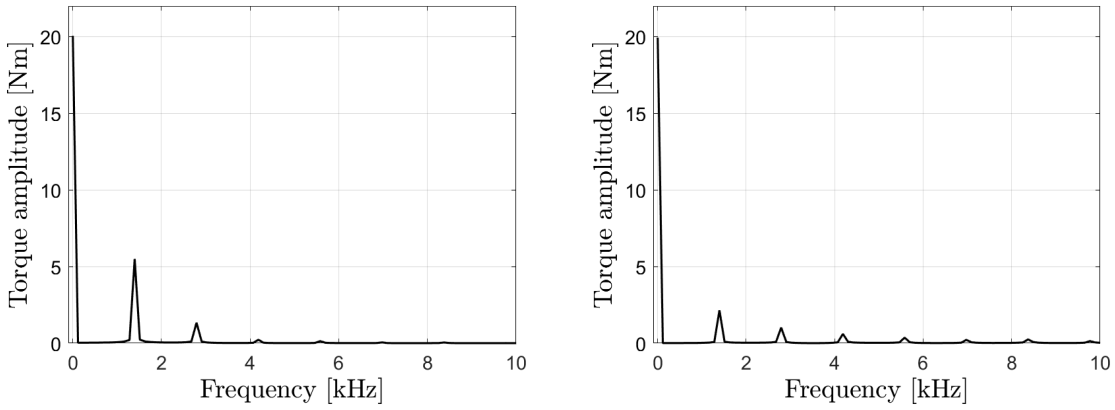

(a) PMSM. **(b)** EESM.

Figure 5.18: Frequency spectra of the reference PMSM and EESM-2 torque outputs.

The frequency spectra of the induced stator phase voltages, also called back EMF, are shown in Figure 5.19 for the two motors. It is clear that the torque-producing component also is the fundamental component with a frequency of 233.33 Hz, which should be the case since $q = \frac{1}{2}$. However, as expected there are also higher order harmonics, mainly of orders $n = 6k-1$ and $n = 6k+1$ ($k = 1, 2, 3...$) for both motors. These harmonics cause the sixth order torque ripple. The EESM has slightly more prominent higher order harmonics, which explains why the torque ripple of the EESM contains more higher order harmonics. It can also be noted that the third harmonic is visible in both frequency spectra. However, as discussed in Section 2.6.1 third order harmonics will cancel in the line voltages.

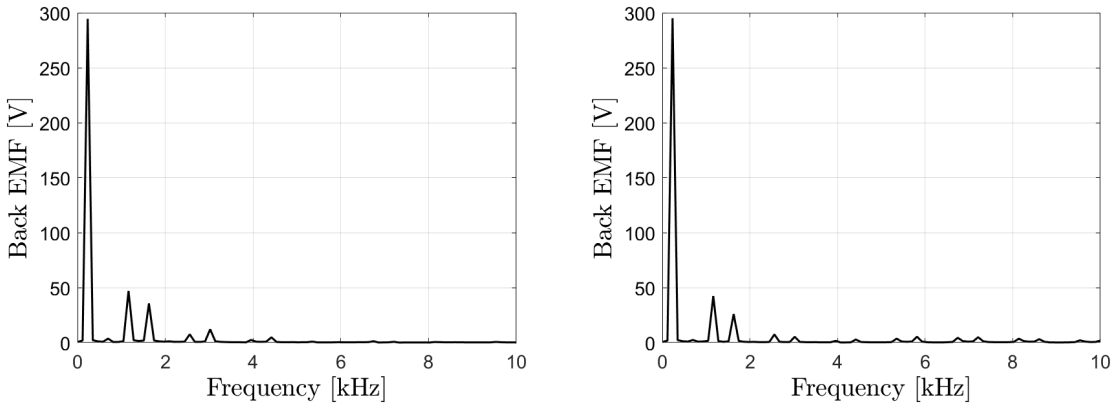

(a) PMSM. **(b)** EESM.

Figure 5.19: Frequency spectra of the induced stator phase voltages for the reference PMSM and EESM-2.

5.4.2 Torque Ripple in the Constant Torque Region

The torque ripple was also investigated for different torque values in the constant torque region. In this section the torque ripple is presented for the speed 3500 rpm and for torque values between 2 Nm and the maximum peak torque that can be obtained. However, the presented torque ripples are similar at other speeds in the constant torque region as well.

Figure 5.20 shows the torque ripple as a function of average torque for the PMSM. As before, MTPA has been used to obtain the stator currents. The highest ripple of 66.1 % is obtained for the average torque 2 Nm and the lowest torque ripple of 36.1 % is obtained at the maximum peak torque. In the operating region, which includes torque values between 12.6 Nm and 22.2 Nm, the torque ripple is between 57.6 % and 59.7 %.

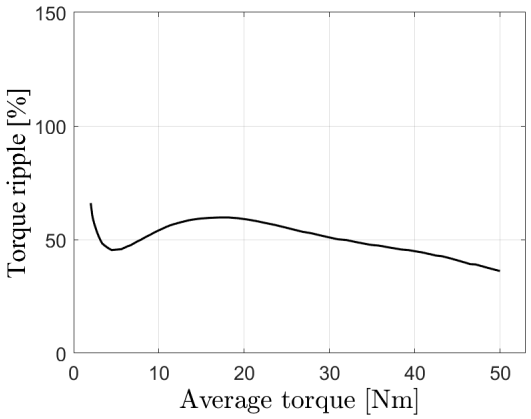

Figure 5.20: Torque ripple for different torque values of the reference PMSM.

The torque ripple of EESM-2 for different penalty factors are shown in Figure 5.21. The torque ripple curves are quite different for different penalty factors. Hence,

it is possible to change the torque ripple in one operating point by adjusting the relationship between the stator current and the field current. At the operating point 20 Nm the torque ripple is lower for EESM-2 compared to the reference PMSM for all penalty factors. The lowest torque ripple at 20 Nm is 23.1 % and it is obtained for the penalty factors $k_\mathrm{d} = k_\mathrm{q} = R_\mathrm{s}$. By adjusting the stator current and the field current, taking torque ripple and the temperature limit shown in Figure 5.12 into account, it is possible to obtain a torque ripple smaller than that of the PMSM in the entire operating region. The operating region includes torque values between 12.6 Nm and 22.2 Nm.

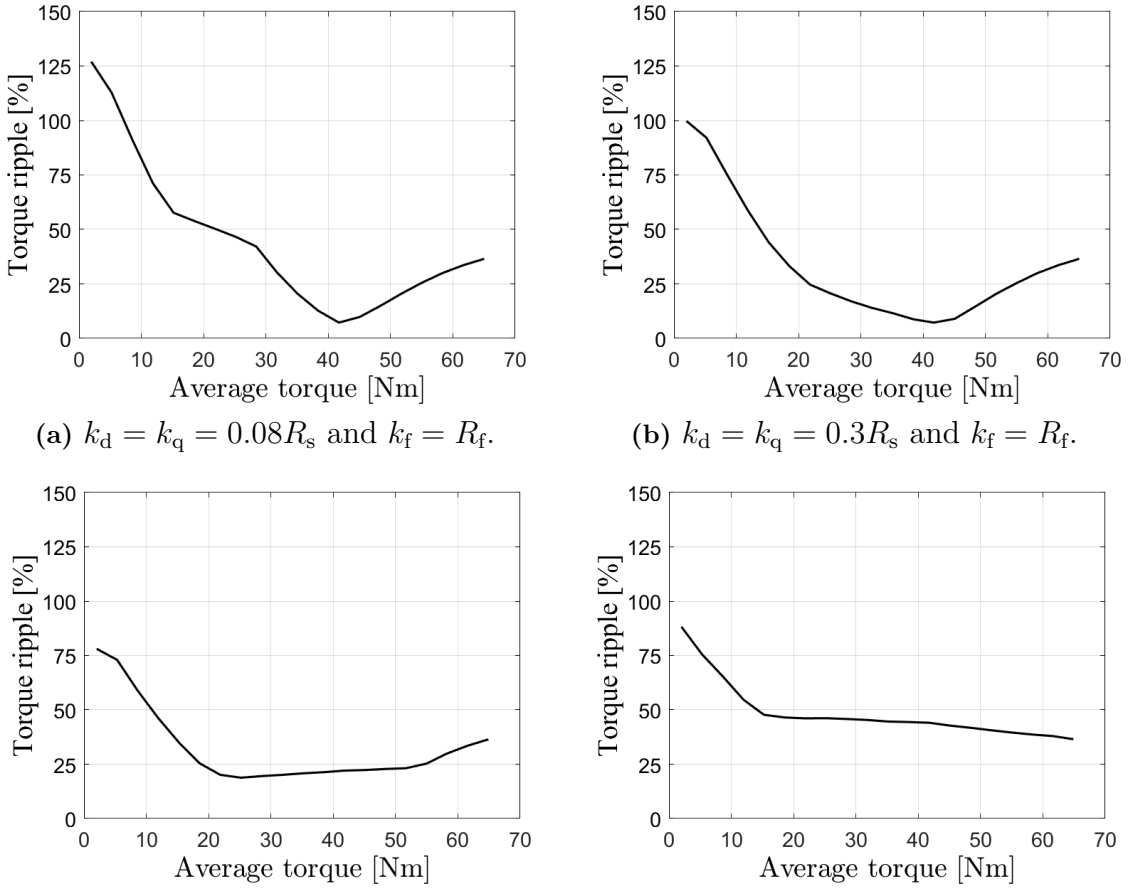

(a) $k_\mathrm{d} = k_\mathrm{q} = 0.08R_\mathrm{s}$ and $k_\mathrm{f} = R_\mathrm{f}$.

(b) $k_\mathrm{d} = k_\mathrm{q} = 0.3R_\mathrm{s}$ and $k_\mathrm{f} = R_\mathrm{f}$.

(c) $k_\mathrm{d} = k_\mathrm{q} = R_\mathrm{s}$ and $k_\mathrm{f} = R_\mathrm{f}$.

(d) $k_\mathrm{d} = k_\mathrm{q} = 8R_\mathrm{s}$ and $k_\mathrm{f} = R_\mathrm{f}$.

Figure 5.21: Torque ripple at different torque values for EESM-2 for different penalty factors k_d, k_q and k_f.

5.4.3 Cogging Torque

The cogging torques of the reference PMSM and EESM-2 were investigated separately. The cogging torques of the two machines are shown in Figure 5.22 for one electric period for the mechanical speed 3500 rpm. However, the cogging torque will be similar for other speeds. The PMSM has a peak cogging torque of 0.69 Nm. The cogging torque of the EESM is dependent on the field current. A field current of 0 A results in zero cogging torque since there is no rotor flux. When the field current

increases, the rotor flux and cogging torque increase as well. A field current lower than 3 A is required for the EESM to have a lower cogging torque than the PMSM. The maximum field current shown in Figure 5.22b is 6 A; much higher field current will cause overheating.

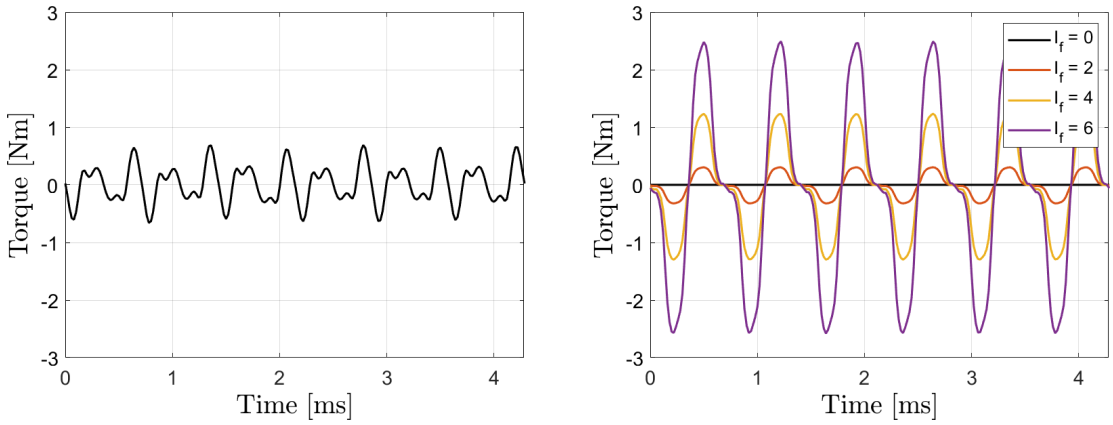

(a) PMSM. **(b)** EESM.

Figure 5.22: Cogging torque for the reference PMSM and EESM-2. The cogging torque of EESM-2 is shown for different field currents I_f [A]. The mechanical speed is 3500 rpm for both motors.

5.5 Sustainability and Cost

Two of the main reasons why an EESM should be used instead of a PMSM is to reduce cost and environmental impact. Therefore, in this section the material cost and the environmental cost of the two motors are investigated. The results are presented for both EESM-1 and EESM-2 to analyze how the motor size affects the costs.

Both the material cost and the environmental cost are dependent on several factors, such as materials, manufacturing, production volume, profit margins and transportation [41]. In this thesis, only the cost of the active materials is considered since this is assumed to cause the largest cost difference. The active materials are the laminated steel, the copper in the copper wires and the NdFeB magnets. According to [42] the production of electric motors results in scrap materials, in which some can be reused and some can not. This means more material is needed at the input of the production compared to the material in the finished motor. However, to simplify the analysis only the active materials in the final motor will be investigated in this project. The presented material and environmental costs will therefore represent the lower limits.

Furthermore, it should be noted that an EESM needs an energy transmitter to transfer currents to the field windings. This transmitter is not investigated in this thesis and the corresponding costs are therefore not considered in the analysis. However,

depending on which kind of technology is used this might affect both the material cost and the environmental cost of the EESMs.

All cost quantities will be given per kg material mass and the masses for the different materials are therefore needed. The mass of the steel, copper and magnets for the reference PMSM, EESM-1 and EESM-2 are shown in Table 5.3. The end windings are included in the copper mass.

Table 5.3: Material mass in kg for the PMSM, EESM-1 and EESM-2.

	PMSM	**EESM-1**	**EESM-2**
Stator steel laminations	3.598 kg	3.598 kg	6.737 kg
Rotor steel laminations	2.363 kg	1.636 kg	3.063 kg
Stator copper winding	1.474 kg	1.474 kg	2.106 kg
Rotor copper winding	-	0.722 kg	1.064 kg
Total steel mass	5.961 kg	5.234 kg	9.800 kg
Total copper mass	1.474 kg	2.196 kg	3.170 kg
Total NdFeB magnet mass	0.310 kg	-	-

5.5.1 Material Cost

The material costs per kg material are summarized in Table 5.4. The cost of the steel laminations is for the material M310-50A. It is the average cost during April 2024 and the data is taken from Shanghai Metals Market (SMM) [43]. The cost of the NdFeB45SH magnet is also the average cost during April 2024 according to SMM [44]. Cost data for a longer time period was not available at SMM. The specified copper cost is the average cost between January and Mars 2024 from the London Metal Exchange (LME) [45].

Table 5.4: Cost in USD per kg for the active materials used in the motors.

Material	**Cost (USD/kg)**	**References**
Steel laminations	1.0	[43]
Copper	8.4	[45]
NdFeB magnet	33.4	[44]

The total material cost of the PMSM, EESM-1 and EESM-2 are shown in Table 5.5. EESM-1 is the cheapest motor with a cost of 23.6 USD. EESM-2, on the other hand, is the most expensive one with a cost of 36.4 USD. The reference PMSM has an active material cost of 28.8 USD. However, as discussed in Section 1.1 the cost of NdFeB magnets may vary. According to [46] there was an increase in the raw material price of NdFeB magnets between 2017 and 2022, from 31.6 USD/kg to 71.4 USD/kg. Now the price is back close to the 2017 level again. Using the magnet cost for 2022 the reference PMSM would have a total active material cost of 40.5 USD, which is higher than the cost of EESM-2. Thus, using prices accurate for 2024 a longer EESM that fulfills the performance criteria is not more cost-efficient

compared to the reference PMSM. However, if the prices of NdFeB magnets increase even a long EESM may be cheaper compared to the PMSM.

Table 5.5: Material cost in USD for the PMSM, EESM-1 and EESM-2.

	PMSM	**EESM-1**	**EESM-2**
Steel lamination	6.0 USD	5.2 USD	9.8 USD
Copper	12.4 USD	18.4 USD	26.6 USD
NdFeB magnet	10.4 USD	-	-
Total material cost	28.8 USD	23.6 USD	36.4 USD

5.5.2 Environmental Cost

The active materials used in PMSMs and EESMs also impact the environment. There are several ways to measure environmental impact and in this thesis two different measurements are presented: global warming potential and eco cost.

It should be noted that the efficiencies of the motors are not considered in the analysis of the environmental cost in this thesis. As shown in Section 5.3.1, the efficiency of the EESM in the operating region is slightly lower compared to the efficiency of the PMSM. Low efficiency means that more electricity is needed. Depending on the electricity source this will also affect the environment.

5.5.2.1 Global Warming Potential

Global warming is caused by greenhouse gas emissions (GHG emissions). The unit of measurement that is used to compare the global warming potential (GWP) of different GHGs is kilogram carbon dioxide equivalent per kilogram material (kg CO_2-eq/kg) [47]. Thus, if the GWP is given in the unit kg CO_2-eq/kg several GHGs are accounted for.

Table 5.6 shows the GWP in kg CO_2-eq/kg for the active materials. This data is for cradle-to-gate, meaning that it accounts for the GWP in all processes from the extraction of the raw materials (cradle) to when the material leaves the factories (gate). It is important to note that the chosen mining strategy and the manufacturing processes of the materials may affect GHG emissions. The GWP of copper is highly dependent on the ore grade, mine size and the extraction process [48], [49]. For a low ore grade the GWP can be almost 20 kg CO_2-eq/kg, while higher ore grades correspond to a GWP of approximately 2-3 kg CO_2-eq/kg [48]. Fuel sources for heating and electricity also matter [50]. As a result of this, the GWP of copper varies between different parts of the world. In Sweden the average GWP of copper production is roughly 2 kg CO_2-eq/kg but in South Africa it is over 8 kg CO_2-eq/kg [50]. Globally, the average GWP of copper production is approximately 6 kg CO_2-eq/kg [50], this is the value for the GWP of copper used in this thesis. Data for the GWP of the steel laminations and the NdFeB magnets is more consistent in the literature [3], [51], [52].

Table 5.6: GWP, measured in kg CO_2-eq/kg, for the active materials used in the motors.

Material	**GWP (kg CO_2-eq/kg)**	**References**
Steel laminations	2	[51]
Copper	6	[50]
NdFeB magnet	30	[3], [51], [52]

The total GWPs of the reference PMSM, the EESM-1 and the EESM-2 are shown in Table 5.7. EESM-1 has the lowest GWP of 23.7 kg CO_2-eq, whereas EESM-2 has the highest value of 38.6 kg CO_2-eq. As for the material cost, it is clear that if the EESM has the same outer dimension as the PMSM it has a lower GWP. However, if the EESM needs to be significantly larger to meet the performance requirements, it may contribute more to global warming.

Table 5.7: GWP, measured in kg CO_2-eq, for the PMSM, EESM-1 and EESM-2.

	PMSM	**EESM-1**	**EESM-2**
Steel laminations	11.9 kg CO_2-eq	10.5 kg CO_2-eq	19.6 kg CO_2-eq
Copper	8.8 kg CO_2-eq	13.2 kg CO_2-eq	19.0 kg CO_2-eq
NdFeB magnet	9.3 kg CO_2-eq	-	-
Total GWP	30.0 kg CO_2-eq	23.7 kg CO_2-eq	38.6 kg CO_2-eq

5.5.2.2 Eco Cost

The production of the active materials in electric motors does not only impact the environment through GHG emissions; the production affects the resource availability, human health, water quality and biodiversity. To include different types of environmental impacts eco cost may be used.

Raw materials can be classified as critical materials if they have a high economic significance and a high risk of disruption in supply [53]. Some raw materials that are of strategic importance are also classified as strategic materials [53]. Iron is neither a critical nor a strategic raw material [53]. This is because iron is a common element in the earth's crust and it has a high recycling rate of 90 % [54]. Copper is considered a vital material for electrification, and it is therefore classified as a strategic material [53]. However, copper is not a critical raw material since the production is distributed across many countries and the risk of supply shortages is therefore reduced [53]. REEs are considered critical and strategic materials because of increased supply risks, geopolitical reasons and low recycling rates [53], [54].

Mining and production of copper and REEs also affect the surrounding environment and human health [54]. Copper mining causes deforestation and pollution of air, water and soil [55], [56]. Human health is also affected directly by pollution in air and smelter dust and indirectly by contaminated water and food [55]. For REE production there are 2000 tonnes of solid waste for each tonne of produced REE [7]. Two major concerns connected to REE production are that many chemicals are

used and that large quantities of the waste contain radioactive elements [57]. This affects both the surrounding environment and human health negatively [54], [57].

Eco cost is the cost required to decrease environmental pollution and resource depletion to what aligns with Earth's carrying capacity [58]. The total eco cost of a specific material is the sum of the eco costs of ecosystems, human health, global warming and resource depletion [58]. Table 5.8 shows the eco costs of the active materials used in the electric motors. The data for the steel laminates is taken as the eco cost for hot rolled steel sheets. Moreover, the data for the NdFeB magnet is not specifically for the type NdFeB45SH, but for a magnet with 40 MGOe. However, the eco costs for those magnets are assumed to be similar.

Table 5.8: Eco costs in USD/kg for the active materials used in the electric motors.

Material	**Eco cost (USD/kg)**	**References**
Steel laminations	0.6	[59]
Copper	5.8	[59]
NdFeB magnet	115.9	[59]

Table 5.9 shows the total eco costs for the active materials in the three different motors. The reference PMSM has the highest eco cost due to the magnets. The eco cost of EESM-2 is roughly half that of the PMSM and the eco cost of EESM-1 is even lower. Thus, to reduce the eco cost an EESM should be used instead of a PMSM. Furthermore, it can be argued that from ethical and societal perspectives, the impacts on the environment, human health and resource depletion should be kept as low as possible. Hence, choosing a motor with a low eco cost is also beneficial considering ethical aspects.

Table 5.9: Eco costs measured in USD for the PMSM, EESM-1 and EESM-2.

	PMSM	**EESM-1**	**EESM-2**
Steel lamination	3.6 USD	3.1 USD	5.9 USD
Copper	8.5 USD	12.7 USD	18.4 USD
NdFeB magnet	35.9 USD	-	-
Total eco cost	48.0 USD	15.8 USD	24.3 USD

6

Effect of Different Cooling Methods

The copper losses in the field windings are a bottleneck for the continuous torque of the EESM since the losses result in high hot-spot temperatures. In this chapter, different cooling techniques are investigated to reduce the temperature in the rotor. For the simulations in this chapter the model EESM-1 with a stack length of 47 mm will be used, since it is of interest to investigate if it is possible to achieve the same continuous torque density as with the reference PMSM. Furthermore, all current values mentioned in this chapter are the values used in Ansys Maxwell. For the thermal simulations these currents are multiplied with a factor of 1.1 to account for harmonics and other disturbances.

6.1 Rotor Cooling Topologies

There are several different rotor cooling techniques. In this project three different topologies will be investigated: rotor shaft cooling, direct rotor cooling with channels and rotor shaft cooling combined with direct rotor cooling with channels. All of these require a cooling liquid. For all investigated rotor cooling topologies the stator will be water-cooled as before.

6.1.1 A: Rotor Shaft Cooling

The rotor can be cooled by pumping a cooling liquid through the hollow shaft and this is illustrated in Figure 6.1 [60]. The inlet and the outlet may be connected with a cooling chamber in between. This cooling configuration is rather easy to implement, however, the cooling of the rotor lamination will be indirect [60]. This cooling technique will be referred to as method A further on.

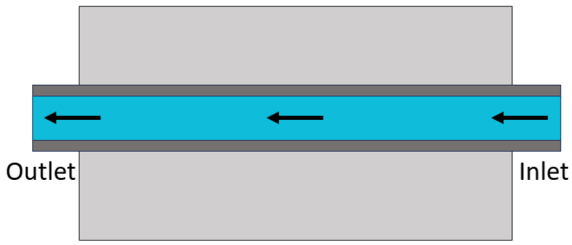

Figure 6.1: Illustration of rotor shaft cooling.

6.1.2 B: Direct Rotor Cooling with Channels

Direct rotor cooling with channels is illustrated in Figure 6.2. The coolant flows into the shaft and is then led into axial channels through the rotor laminations. According to [60] this cooling configuration has the advantage of the coolant flowing close to the field windings. Another advantage is that there is no coolant inside the rotor shaft, making it possible to place a rotary transformer, or another device for energy transfer to the field windings, inside the shaft. This cooling method will be called method B.

Figure 6.2 shows that the cooling channels are placed on the q-axis in the rotor and they have a diameter of 6 mm. They are placed relatively close to the field windings to cool them efficiently. However, putting them too close to the windings would cause saturation of the iron around the channels. The placement and the size of the channels were determined through electromagnetic simulations in Ansys Maxwell and thermal simulations in Ansys Mechanical. It was confirmed that larger channels result in a reduced torque output and smaller channels do not cool the rotor as efficiently. Furthermore, if the channels were placed on the d-axis the torque output was also reduced.

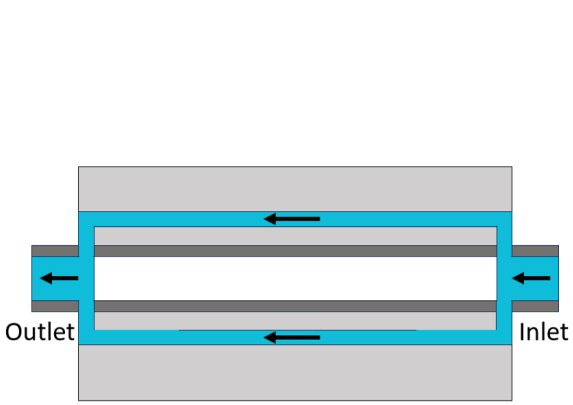

(a) Axial cross section of the rotor.

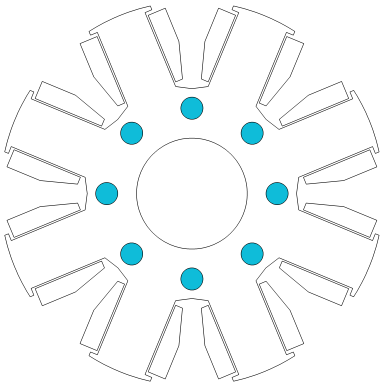

(b) Radial cross section of the rotor.

Figure 6.2: Illustration of direct rotor cooling with channels.

6.1.3 C: Rotor Shaft Cooling Combined with Direct Rotor Cooling with Channels

Rotor shaft cooling combined with direct rotor cooling with channels is illustrated in Figure 6.3. This cooling method is a combination of method A and method B and will be referred to as method C.

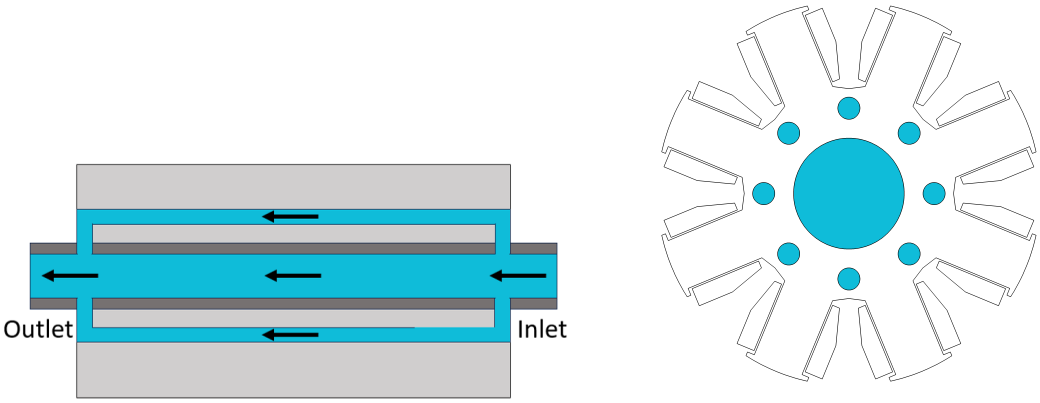

(a) Axial cross section of the rotor.

(b) Radial cross section of the rotor.

Figure 6.3: Illustration of rotor shaft cooling combined with direct rotor cooling with channels.

6.2 Boundary Conditions for Thermal Simulations and Liquid Properties

All boundary conditions for the thermal simulations were assumed to be the same as the boundary conditions presented in Section 3.3.5. However, new boundary conditions had to be added for the cooling channels. The rotor shaft rotates along with the rotor and the thermal properties of a liquid flowing through a rotating shaft are rather complex to model. This is mainly due to the influence of the Coriolis and centrifugal forces that cause the heat transfer coefficient to be highly dependent on the rotational speed [61]. However, to simplify the thermal modeling these effects were not taken into account. Instead, it was assumed that the walls of the shaft and/or the channels are cooled by convection and the convective heat transfer coefficient was set to $2000\,\mathrm{W/m^2K}$ and the liquid was set to have a temperature of $70\,^{\circ}\mathrm{C}$. These are the same boundary conditions used for the water-cooling of the stator.

Which cooling liquid that should be used for the rotor is not specified in this project; the boundary conditions are assumed to be true for several different coolants. However, it should be noted that if the liquid is in direct contact with the electric machine a dielectric fluid, like oil, is required [61]. Furthermore, if another liquid than water is used it is probably beneficial to also use it for the cooling of the stator to remove the need for two different cooling systems.

6.3 Simulation Results

For the cooling methods A, B and C described above electromagnetic and thermal simulations were performed. The stator and field current were chosen such that the thermal limit 170 °C was hit in both the stator windings and the field windings. In that way the torque was maximized. The results are shown in Table 6.1. Here, the currents and the average torque obtained without any cooling inside the rotor are also presented. It is clear that it is possible to use a higher field current for continuous operation when the rotor is cooled more efficiently and that will result in a higher average torque. Furthermore, using cooling channels, as method B and method C do, seems to be advantageous. A probable reason for this is that the coolant gets closer to the field windings where the hot spots are. For cooling method C the continuous torque is increased by almost 40 % compared to the case with no rotor cooling.

Table 6.1: Results from simulations of different cooling methods.

	No rotor cooling	**A**	**B**	**C**
Average torque (Nm)	12.6	16.8	17.4	17.5
Stator current amplitude (A)	21.3	21.6	21.6	21.6
Field current (A)	3.5	6.5	7.0	7.1

It can be concluded that with a more efficient rotor cooling technique it is possible to increase the continuous torque output. Thus, if an efficient rotor cooling technique is implemented it is possible to make the EESM shorter than 88 mm, which was the case for EESM-2. This is beneficial in terms of space and weight saving. Also, the material cost and the environmental cost will be reduced. However, since the nominal torque 20 Nm is not reached for any of the investigated cooling methods the thermal model suggests that it is not possible to use as short stack length as 47 mm, which the reference PMSM has.

7

Conclusion

In this project, an EESM was designed by sweeping the rotor geometry and using a stator from a reference PMSM. It was shown that the geometry of the rotor poles affects the maximum continuous torque. The width of the rotor pole shoe has the largest effect on the output torque; a wide rotor pole shoe results in a lower continuous torque due to a low reluctance torque. Furthermore, if the rotor pole shoe width is rather small the curvature of it should follow that of the stator. However, if only stator cooling is used the EESM has to be made longer than the PMSM to reach the nominal torque in continuous operation.

The characteristics and performance of an EESM model with a 87 % longer stack length than the reference PMSM were investigated further. The characteristics of the designed EESM are similar to those of the reference PMSM. The main difference is that the EESM offers a larger opportunity to tune the performance by adjusting the field current. To determine the optimal currents in an EESM a copper loss minimization algorithm that distributes the copper losses in the stator and the rotor based on chosen penalty factors can be used. With only stator cooling, high continuous torque is achieved when more copper losses are distributed to the stator windings. Moreover, to maximize the efficiency, the total copper loss should be minimized while the thermal limit is considered. In the nominal operating point, the maximum efficiency of the designed EESM is slightly more than 2.8 percentage points lower than the efficiency of the PMSM. Furthermore, to reach as high power factor as for the PMSM a high field current is required, which overheats the motor. Thus, with the designed EESM it is impossible to achieve high continuous torque, maximum efficiency and high power factor in the constant torque region simultaneously. This is possible with the reference PMSM. However, to obtain a high overall efficiency it is probably beneficial to primarily focus on obtaining the required continuous torque while maximizing the efficiency of the machine, and not so much on the power factor. Regarding the torque ripple, it seems achievable to reduce the ripple in the entire region where the motor operates by using the designed EESM instead of the PMSM.

The material costs are different for an EESM and a PMSM. If the EESM and the PMSM have the same outer dimensions the material cost is lower for the EESM. However, if a much longer EESM is needed the material cost may surpass that of the PMSM. The same is true for the GWP. However, considering the eco costs it is beneficial to use an EESM, even if the EESM is longer. Lowering the eco cost

is probably the major advantage of using an EESM instead of a PMSM for the considered application.

To improve the continuous torque of an EESM a more efficient rotor cooling technique is required. Simple techniques that utilize liquid cooling channels in the rotor steel laminations are shown to improve the continuous torque by almost 40 %.

Finally, it can be concluded that whether or not it is feasible to use an EESM instead of a PMSM for an application that operates continuously in the constant torque region depends on the design, performance and cost requirements. If the EESM should have the same outer dimensions and only stator cooling is used, it is not possible to achieve the required continuous torque. However, if the motor can be made a little longer, a slightly lower efficiency can be accepted and more efficient rotor cooling is implemented it may be possible to use an EESM as a more sustainable alternative. However, future work is needed to confirm this and to improve the design of the EESM.

7.1 Future Work

To further investigate the possibility of using an EESM instead of a PMSM for an application that operates continuously in the constant torque region several different aspects should be considered. In this study, only the copper losses were used to optimize the currents. In Section 5.3.1 it is shown that also the core losses has a significant effect on the efficiency of the EESM. Thus, it is possible that higher efficiency can be obtained if also core losses are taken into account in the iterative algorithm and this should be investigated further.

In this thesis, it is assumed that the power factor does not affect the overall efficiency of the driveline significantly. Therefore, it is recommended to focus on obtaining a high efficiency of the motor, not a high power factor. However, to confirm this the efficiency of the stator inverter should be investigated for lower power factors.

It should also be investigated if it is possible to increase the continuous torque without changing the outer dimensions by modifying the stator geometry. A comparison between EESM and PMSM has been conducted by [37] for a traction application. For the EESM the size of the rotor was increased at the expense of the stator size. The outer dimensions of the two motors were kept the same. By increasing the rotor size there is room for more copper in the rotor. This might be beneficial for the copper losses in the rotor and the generated rotor MMF. Therefore, this should be investigated in future work.

A more accurate thermal model should be implemented to increase the accuracy of the thermal simulations. With a more accurate model, it would be possible to determine more reliable values for the maximum currents and torque for continuous operation. It would also be possible to do more precise investigations of different rotor cooling systems. It is suggested that each strand in the windings should be modeled separately to increase the accuracy, even though this has the downside of an increased simulation time. Moreover, measurements or calculations should be

performed to determine the convective heat transfer coefficient between the rotor and the stator.

With a more accurate thermal model, it is possible to determine the shortest possible stack length needed to reach the same continuous torque as the reference PMSM when different cooling methods are implemented. This needs to be studied to draw further conclusions regarding the size and cost of the EESM.

Moreover, it is concluded that with the same cooling method as the PMSM, the EESM has lower torque density, lower efficiency and lower power factor. These characteristics are similar to those of IMs and synRMs, as discussed in Section 1.1. Hence, the EESM should be compared to an IM and a synRM to determine which magnet-free motor has the most satisfactory performance.

Finally, if it seems feasible to use an EESM after the stator has been redesigned, the thermal model has been updated and the performance has been compared to other magnet-free motors, the energy transfer to the rotor should be investigated further. Also, the control of the machine should be studied.

Bibliography

[1] J.-R. Riba Ruiz, J. A. Rosero, A. Garcia Espinosa, and L. Romeral, "Detection of Demagnetization Faults in Permanent-Magnet Synchronous Motors Under Nonstationary Conditions," *IEEE Transactions on Magnetics*, vol. 45, no. 7, pp. 2961–2969, 2009. DOI: 10.1109/TMAG.2009.2015942.

[2] J. Tang, "Design and Control of Electrically Excited Synchronous Machines for Vehicle Applications", Ph.D. dissertation, Department of Electrical Engineering, Chalmers University of Technology, Gothenburg, Sweden, 2021. [Online]. Available: https://research.chalmers.se/publication/522780.

[3] J. D. Widmer, R. Martin, and M. Kimiabeigi, "Electric vehicle traction motors without rare earth magnets," *Sustainable Materials and Technologies*, vol. 3, pp. 7–13, 2015, ISSN: 2214-9937. DOI: 10.1016/j.susmat.2015.02.001.

[4] G. Mademlis, Y. Liu, J. Tang, L. Boscaglia, and N. Sharma, "Performance Evaluation of Electrically Excited Synchronous Machine compared to PMSM for High-Power Traction Drives," in *2020 International Conference on Electrical Machines (ICEM)*, vol. 1, 2020, pp. 1793–1799. DOI: 10.1109/ICEM49940.2020.9270852.

[5] D. G. Dorrell, A. M. Knight, M. Popescu, L. Evans, and D. A. Staton, "Comparison of different motor design drives for hybrid electric vehicles," in *2010 IEEE Energy Conversion Congress and Exposition*, 2010, pp. 3352–3359. DOI: 10.1109/ECCE.2010.5618318.

[6] P. Andrews-Speed and A. Hove, "China's rare earths dominance and policy responses," Oxford Institute for Energy Studies, Tech. Rep. ISBN 978-1-78467-208-9, Jun. 2023. [Online]. Available: https://www.oxfordenergy.org/publications/chinas-rare-earths-dominance-and-policy-responses/.

[7] T. McNulty, N. Hazen, and S. Park, "Processing the ores of rare-earth elements," *MRS Bulletin*, vol. 47, pp. 258–266, 2022. DOI: 10.1557/s43577-022-00288-4.

[8] J.-R. Riba, C. López-Torres, L. Romeral, and A. Garcia, "Rare-earth-free propulsion motors for electric vehicles: A technology review," *Renewable and Sustainable Energy Reviews*, vol. 57, pp. 367–379, 2016, ISSN: 1364-0321. DOI: https://doi.org/10.1016/j.rser.2015.12.121.

[9] D. C. Ludois, J. K. Reed, and K. Hanson, "Capacitive Power Transfer for Rotor Field Current in Synchronous Machines," *IEEE Transactions on Power Electronics*, vol. 27, no. 11, pp. 4638–4645, 2012. DOI: 10.1109/TPEL.2012.2191160.

[10] J. Haruna and T. Raminosoa, "Modeling and Steady-State Analysis of a Rotary Transformer-Based Field Excitation System for Wound Rotor Synchronous Machine," in *2019 IEEE Transportation Electrification Conference and Expo (ITEC)*, 2019, pp. 1–8. DOI: 10.1109/ITEC.2019.8790472.

[11] R. Manko, M. Vukotić, D. Makuc, D. Vončina, D. Miljavec, and S. Čorović, "Modelling of the Electrically Excited Synchronous Machine with the Rotary Transformer Design Influence," *Energies*, vol. 15, no. 8, 2022, ISSN: 1996-1073. DOI: 10.3390/en15082832.

[12] J. Tang and Y. Liu, "Design and Experimental Verification of a 48 V 20 kW Electrically Excited Synchronous Machine for Mild Hybrid Vehicles," in *2018 XIII International Conference on Electrical Machines (ICEM)*, 2018, pp. 649–655. DOI: 10.1109/ICELMACH.2018.8507259.

[13] E.M. Illiano, "Design of a highly efficient brushless current excited synchronous motor for automotive purposes", Ph.D. dissertation, Department of Information Technology and Electrical Engineering, ETH Zurich, Zurich, Switzerland, 2014. [Online]. Available: https://api.semanticscholar.org/CorpusID:73591324.

[14] A. Hussain, Z. Baig, W. T. Toor, *et al.*, "Wound Rotor Synchronous Motor as Promising Solution for Traction Applications," *Electronics*, vol. 11, no. 24, 2022. DOI: 10.3390/electronics11244116.

[15] D. K. Cheng, *Field and Wave Electromagnetics*, second edition. Edinburgh Gate, Harlow, Essex, CM20 2JE, Scotland: Pearson, 2014.

[16] P. Kundur, *Power System Stability and Control*, first edition. New York, USA: McGraw-Hill, 1994.

[17] T. Lipo, *Introduction to ac machine design*, New Jersey, NJ, USA, 2017. [Online]. Available: https://ieeexplore.ieee.org/servlet/opac?bknumber=8068864.

[18] S. N. Vukosavic, *Electrical Machines, Power Electronics and Power Systems*, New York, NY, USA, Springer, 2013. DOI: 10.1007/978-1-4614-0400-2.

[19] L. Harnefors, *Control of variable speed drives*. Västerås, Sweden: Mälardalen University, Department of Electronics, Applied Signal Processing and Control, 2002.

[20] C. J. O'Rourke, M. M. Qasim, M. R. Overlin, and J. L. Kirtley, "A Geometric Interpretation of Reference Frames and Transformations: dq0, Clarke, and Park," *IEEE Transactions on Energy Conversion*, vol. 34, no. 4, pp. 2070–2083, 2019. DOI: 10.1109/TEC.2019.2941175.

[21] J. Liu and W. Chen, "Generalized DQ model of the permanent magnet synchronous motor based on extended park transformation," in *2013 1st International Future Energy Electronics Conference (IFEEC)*, 2013, pp. 885–890. DOI: 10.1109/IFEEC.2013.6687627.

[22] J. Tang and Y. Liu, "Design of Electrically Excited Synchronous Machines to Achieve Unity Power Factor in Field Weakening for Long-Haul Electric Trucks," in *2020 International Conference on Electrical Machines (ICEM)*, vol. 1, 2020, pp. 422–428. DOI: 10.1109/ICEM49940.2020.9270755.

[23] H. Akagi, E. H. Watanabe, and M. Aredes, *Instantaneous Power Theory and Applications to Power Conditioning*, New Jersey, USA, Wiley-IEEE Press,

2007. [Online]. Available: https://ieeexplore.ieee.org/servlet/opac?bknumber=5236653.

[24] S. Kim, *Electric Motor Control: DC, AC, and BLDC Motors*, 1st ed. San Diego, USA: Elsevier Science & Technology, 2017.

[25] A. M. EL-Refaie, "Fractional-Slot Concentrated-Windings Synchronous Permanent Magnet Machines: Opportunities and Challenges," *IEEE Transactions on Industrial Electronics*, vol. 57, no. 1, pp. 107–121, 2010. DOI: 10.1109/TIE.2009.2030211.

[26] S. Skoog and A. Acquaviva, "Pole-Slot Selection Considerations for Double Layer Three-phase Tooth-Coil Wound Electrical Machines," in *2018 XIII International Conference on Electrical Machines (ICEM)*, 2018, pp. 934–940. DOI: 10.1109/ICELMACH.2018.8506772.

[27] J. Zhao, Y. Liu, and X. Xu, "Comparisons of Concentrated and Distributed Winding PMSM in MV Power Generation," in *2018 XIII International Conference on Electrical Machines (ICEM)*, 2018, pp. 2437–2443. DOI: 10.1109/ICELMACH.2018.8507199.

[28] C. Lai, G. Feng, K. Mukherjee, V. Loukanov, and N. C. Kar, "Torque Ripple Modeling and Minimization for Interior PMSM Considering Magnetic Saturation," *IEEE Transactions on Power Electronics*, vol. 33, no. 3, pp. 2417–2429, 2018. DOI: 10.1109/TPEL.2017.2695440.

[29] H. Jussila, P. Salminen, M. Niemela, and J. Pyrhonen, "Guidelines for Designing Concentrated Winding Fractional Slot Permanent Magnet Machines," in *2007 International Conference on Power Engineering, Energy and Electrical Drives*, 2007, pp. 191–194. DOI: 10.1109/POWERENG.2007.4380186.

[30] C.-Y. Hsiao, S.-N. Yeh, and J.-C. Hwang, "A Novel Cogging Torque Simulation Method for Permanent-Magnet Synchronous Machines," *Energies*, vol. 4, no. 12, pp. 2166–2179, 2011, ISSN: 1996-1073. DOI: 10.3390/en4122166.

[31] D. Shmilovitz, "On the definition of total harmonic distortion and its effect on measurement interpretation," *IEEE Transactions on Power Delivery*, vol. 20, no. 1, pp. 526–528, 2005. DOI: 10.1109/TPWRD.2004.839744.

[32] C. Nordling and J. Österman, *Physics Handbook for Science and Engineering*, ninth edition. Lund, Sweden: Studentlitteratur AB, 2020.

[33] Y. Zhang, M.-C. Cheng, and P. Pillay, "Magnetic Characteristics and Excess Eddy Current Losses," in *2009 IEEE Industry Applications Society Annual Meeting*, 2009, pp. 1–5. DOI: 10.1109/IAS.2009.5324814.

[34] S. Talebian, Y. Hojjat, M. Ghodsi, and M. R. Karafi, "Study on classical and excess eddy currents losses of Terfenol-D," *Journal of Magnetism and Magnetic Materials*, vol. 388, pp. 150–159, 2015, ISSN: 0304-8853. DOI: 10.1016/j.jmmm.2015.04.033.

[35] J. H. Lienhard IV and J. H. Lienhard V, *A Heat Transfer Textbook*, 5th. Cambridge, MA: Phlogiston Press, Aug. 2020, 784 pp., Version 5.10. [Online]. Available: http://ahtt.mit.edu.

[36] M. Farid, "13 - Heat and Mass Transfer in Food Processing," in *Handbook of Farm, Dairy, and Food Machinery*, M. Kutz, Ed., Norwich, NY: William Andrew Publishing, 2007, pp. 367–390, ISBN: 978-0-8155-1538-8. DOI: 10.1016/B978-081551538-8.50015-7.

[37] W. Q. Chu, Z. Q. Zhu, J. Zhang, *et al.*, "Comparison of electrically excited and interior permanent magnet machines for hybrid electric vehicle application," in *2014 17th International Conference on Electrical Machines and Systems (ICEMS)*, 2014, pp. 401–407. DOI: 10.1109/ICEMS.2014.7013504.

[38] Cogent Surahammars Bruk AB, "Typical data for SURA® M310-50A Data Sheet", Jun. 2008.

[39] Voestalpine, "isovac 310-50 A Data Sheet", Oct. 2022.

[40] J. Tang and Y. Liu, "Comparison of copper loss minimization and field current minimization for Electrically Excited Synchronous Motor in mild hybrid drives," in *2017 19th European Conference on Power Electronics and Applications (EPE'17 ECCE Europe)*, 2017, P.1–P.10. DOI: 10.23919/EPE17ECCEEurope.2017.8099352.

[41] E. A. Grunditz, S. T. Lundmark, M. Alatalo, T. Thiringer, and A. Nordelöf, "Three traction motors with different magnet materials — Influence on cost, losses, vehicle performance, energy use and environmental impact," in *2018 Thirteenth International Conference on Ecological Vehicles and Renewable Energies (EVER)*, 2018, pp. 1–13. DOI: 10.1109/EVER.2018.8362387.

[42] A. Nordelöf, E. Grunditz, A.-M. Tillman, T. Thiringer, and M. Alatalo, "A Scalable Life Cycle Inventory of an Electrical Automotive Traction Machine - Technical and Methodological Description, version 1.0," Divisions of Environmental Systems Analysis & Electric Power Engineering, Department of Energy and Environment, Chalmers University of Technology, Gothenburg, Sweden, Tech. Rep. Report No. 2016:4, 2016.

[43] Shanghai Metals Market, "Wuhan,Wuhan Iron and Steel,50WW310 price Charts", [Online], Available: https://www.metal.com/Finished-Steel/202206070012 (accessed 2024-05-02).

[44] Shanghai Metals Market, "NdFeB blank 45SH (Ce) Price, CNY/kg", [Online], Available: https://www.metal.com/Rare-Earth-Magnets/202103120033?type=1%20Month (accessed 2024-04-29).

[45] London Metal Exchange, "Daily prices and monthly averages", [Online], Available: https://www.lme.com/Market-Data/Reports-and-data/Monthly-averages (accessed 2024-04-29).

[46] M. Schönfeldt, U. Rohrmann, P. Schreyer, *et al.*, "Magnetic and structural properties of multiple recycled and sustainable sintered Nd-Fe-B magnets," *Journal of Alloys and Compounds*, vol. 939, p. 168 709, 2023, ISSN: 0925-8388. DOI: 10.1016/j.jallcom.2023.168709.

[47] European Environment Agency (EEA), "carbon dioxide equivalent", 2001. [Online], Available: https://www.eea.europa.eu/help/glossary/eea-glossary/carbon-dioxide-equivalent (accessed 2024-04-30).

[48] A. Beylot and J. Villeneuve, "Accounting for the environmental impacts of sulfidic tailings storage in the life cycle assessment of copper production: A case study," *Journal of Cleaner Production*, vol. 153, pp. 139–145, 2017, ISSN: 0959-6526. DOI: 10.1016/j.jclepro.2017.03.129.

[49] S. Northey, S. Mohr, G. Mudd, Z. Weng, and D. Giurco, "Modelling future copper ore grade decline based on a detailed assessment of copper resources

and mining," *Resources, Conservation and Recycling*, vol. 83, pp. 190–201, 2014, ISSN: 0921-3449. DOI: 10.1016/j.resconrec.2013.10.005.

[50] A. Ekman Nilsson, M. Macias Aragonés, F. Arroyo Torralvo, *et al.*, "A review of the carbon footprint of cu and zn production from primary and secondary sources," *Minerals*, vol. 7, no. 9, 2017, ISSN: 2075-163X. DOI: 10.3390/min7090168.

[51] X. Zhang, D. Gerada, Z. Xu, F. Zhang, and C. Gerada, "A review of carbon emissions from electrical machine materials," *Electronics*, vol. 13, no. 9, 2024, ISSN: 2079-9292. DOI: 10.3390/electronics13091714.

[52] H. Jin, P. Afiuny, T. McIntyre, Y. Yih, and J. W. Sutherland, "Comparative life cycle assessment of ndfeb magnets: Virgin production versus magnet-to-magnet recycling," *Procedia CIRP*, vol. 48, pp. 45–50, 2016, The 23rd CIRP Conference on Life Cycle Engineering, ISSN: 2212-8271. DOI: 10.1016/j.procir.2016.03.013.

[53] Sveriges geologiska undersökning, "Kritiska och strategiska råvaror", 2023. [Online], Available: https://www.sgu.se/mineralnaring/kritiska-ravaror/ (accessed 2024-05-01).

[54] H. Schillingmann, S. Gehler, and M. Henke, "Life cycle assessment of electrical machine production considering resource requirements and sustainability," in *2021 11th International Electric Drives Production Conference (EDPC)*, 2021, pp. 1–7. DOI: 10.1109/EDPC53547.2021.9684195.

[55] G. Izydorczyk, K. Mikula, D. Skrzypczak, K. Moustakas, A. Witek-Krowiak, and K. Chojnacka, "Potential environmental pollution from copper metallurgy and methods of management," *Environmental Research*, vol. 197, p. 111 050, 2021, ISSN: 0013-9351. DOI: 10.1016/j.envres.2021.111050.

[56] F. Chaddad, F. A. Mello, M. Tayebi, *et al.*, "Impact of mining-induced deforestation on soil surface temperature and carbon stocks: A case study using remote sensing in the amazon rainforest," *Journal of South American Earth Sciences*, vol. 119, p. 103 983, 2022, ISSN: 0895-9811. DOI: 10.1016/j.jsames.2022.103983.

[57] P. Zapp, A. Schreiber, J. Marx, *et al.*, "Environmental impacts of rare earth production," *MRS Bulletin*, vol. 47, pp. 267–275, 2022. DOI: 10.1557/s43577-022-00286-6.

[58] Sustainability Impact Metrics, The concept, structure, and midpoint tables of the eco-costs for LCA, [Online], Available: https://www.ecocostsvalue.com/ecocosts/eco-costs-concept/ (accessed 2024-05-02).

[59] Sustainability Impact Metrics, "Excel files: Idemat and Ecoinvent, and eco-costs midpoint tables", 2024, [Online], Available: https://www.ecocostsvalue.com/data-tools-books/ (accessed 2024-05-01).

[60] M. Raimondo, G. Puccio, S. Nategh, D. Barater, M. Merelli, and A. Carlsson, "Development of Direct Oil Cooling Solutions for E-mobility Traction Motors : Part II: Rotor Cooling Concept," in *2023 IEEE International Electric Machines & Drives Conference (IEMDC)*, 2023, pp. 1–6. DOI: 10.1109/IEMDC55163.2023.10239076.

[61] J. Nonneman, B. van der Sijpe, I. T'Jollyn, S. Vanhee, J. Druant, and M. de Paepe, "Evaluation of High Performance Rotor Cooling Techniques for Perma-

nent Magnet Electric Motors," in *2021 IEEE International Electric Machines & Drives Conference (IEMDC)*, 2021, pp. 1–7. DOI: 10.1109/IEMDC47953.2021.9449603.

A

Resistance Calculation

The resistance of the copper windings in the stator and the rotor had to be estimated. The resistance of the copper windings where calculated using equation (2.38). The length of the copper winding around one stator tooth or rotor pole was calculated as

$$L = N_{\text{turns}}\Big(2(L_{\text{stack}} + 2L_{\text{isolation}}) + \pi(2L_s + w_{\text{tooth}})\Big), \tag{A.1}$$

where the parameters are explained in Figure A.1. L_{stack} is the stack length, $L_{\text{isolation}}$ is an isolation layer with a thickness of 2.5 mm, w_{tooth} is the width of the stator tooth or the width of the rotor pole and L_s is the thickness of half of the winding.

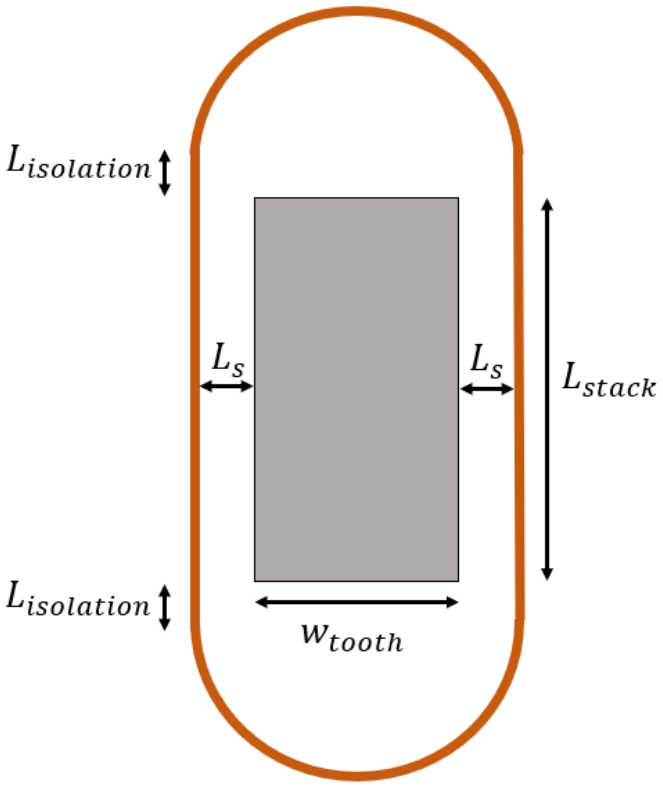

Figure A.1: Illustration of the copper winding around a stator tooth or a rotor pole.

B

Material Properties

The B-H curve for the material M310-50A is shown in Figure B.1 [38].

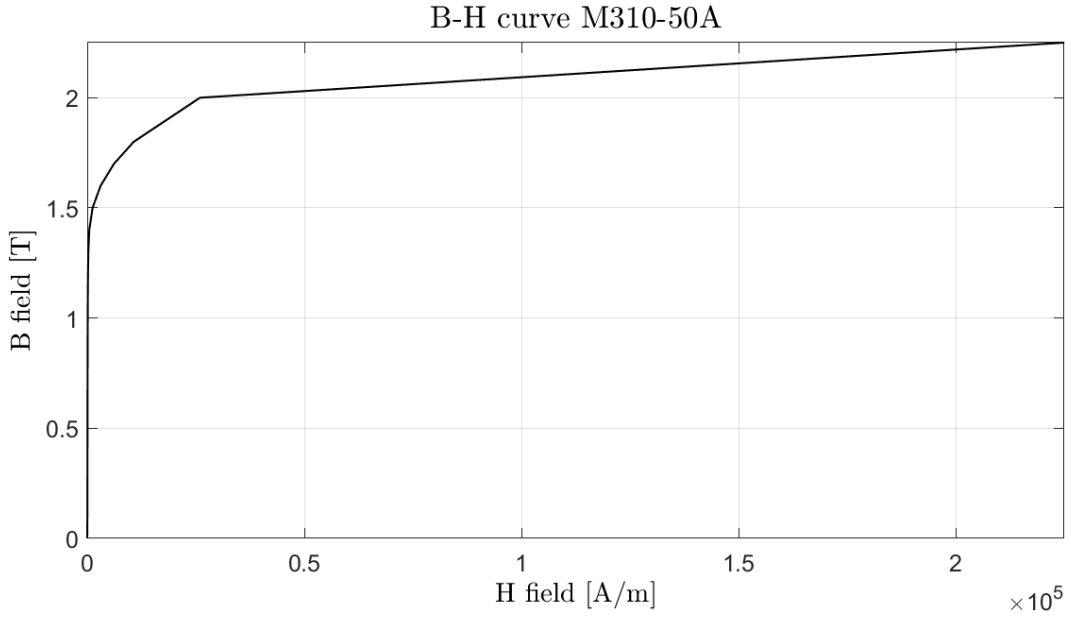

Figure B.1: B-H curve for the material M310-50A.

C

Parametric Sweep of EESM Geometry

In this appendix, the results from the parametric sweep of the EESM are presented. Figure C.1 shows the average torque and the torque ripple for all investigated geometries. The stator current amplitude was set to 18 A and the copper losses in the rotor were set to 40 W. The red dashed line represents the torque ripple of the PMSM at 20 Nm, which is the nominal torque. The operating points marked in yellow correspond to the 40 geometries with the highest torque values and torque ripples lower than that of the PMSM. These geometries were investigated further.

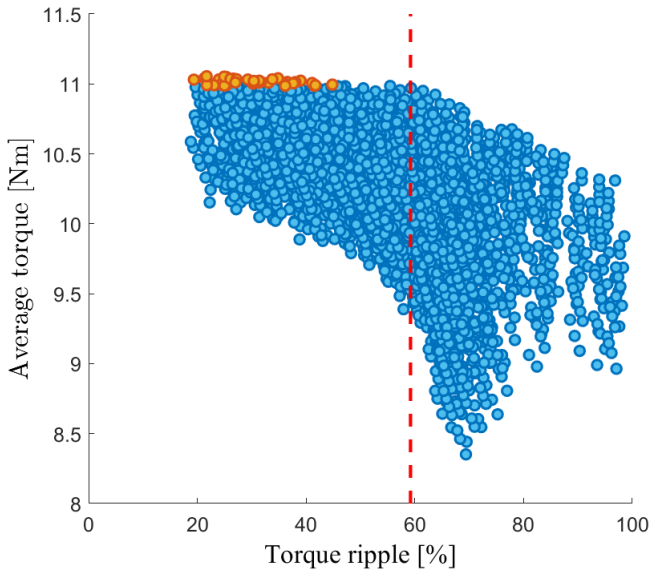

Figure C.1: Average torque and torque ripple for all investigated geometries. The copper losses in the field windings are 40 W.

Figure C.2 and Figure C.3 show the results for the 40 selected geometries with 40 W copper losses in the field windings and with 120 W copper losses in the field windings respectively. Each geometry corresponds to the same color in all plots. It should be noted that in Figure C.2 there is a very small difference in average torque for the different geometries; thus with respect to the average torque it does not matter which geometry is selected. However, for the case with 120 W copper losses in the

field windings in Figure C.3 the differences in average torque are larger between the different geometries. The geometry marked with a red circle is the chosen geometry and this geometry resulted in relatively high torque for the case with 120 W copper losses in the field windings, low torque ripple in both cases and relatively low rotor core losses. With low rotor core losses the field current can be higher before the temperature limit is reached.

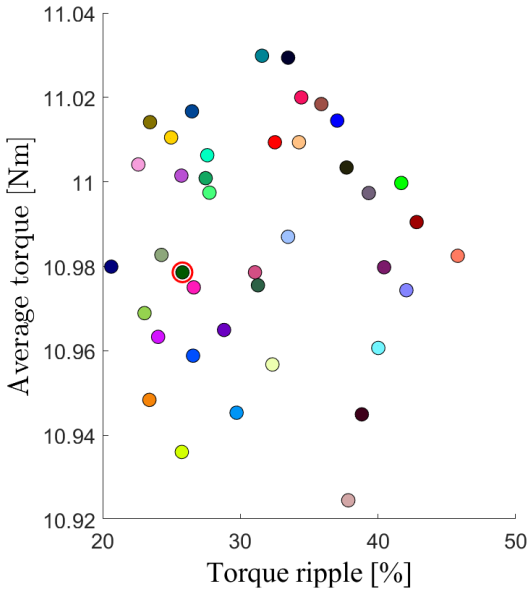

(a) Average torque and torque ripple.

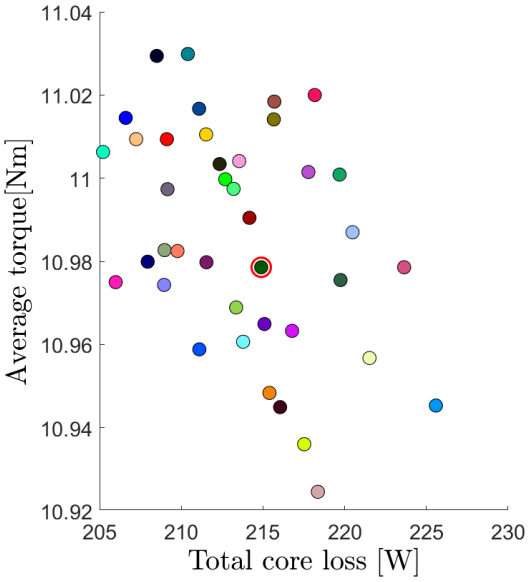

(b) Average torque and total core losses.

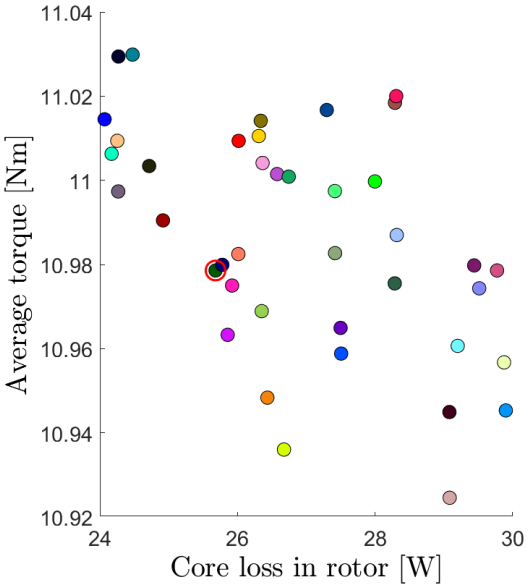

(c) Average torque and rotor core losses.

Figure C.2: Results from the 40 selected geometries with 40 W copper losses in the field windings.

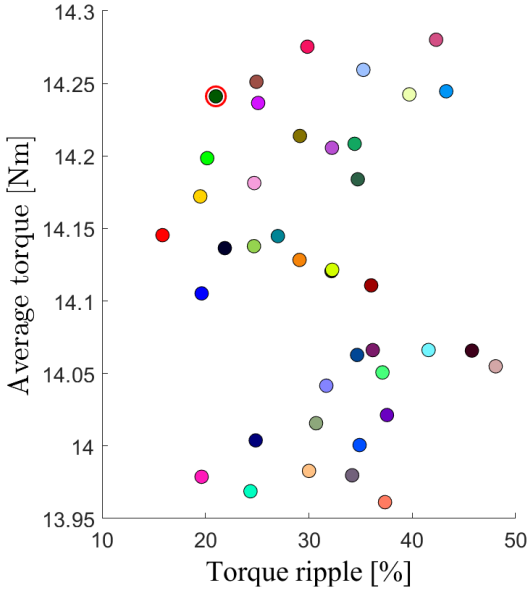

(a) Average torque and torque ripple.

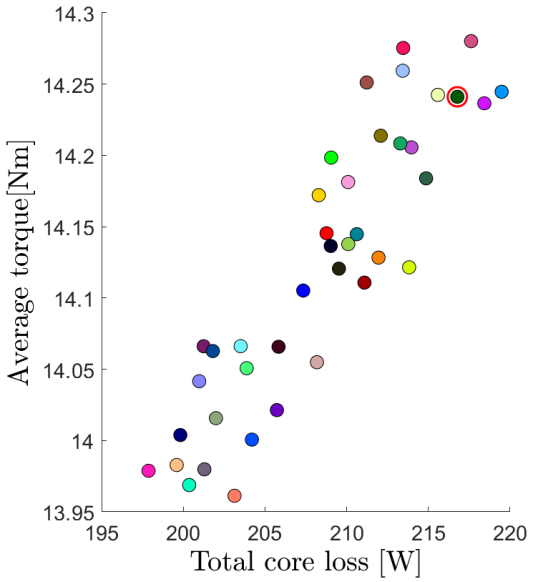

(b) Average torque and total core losses.

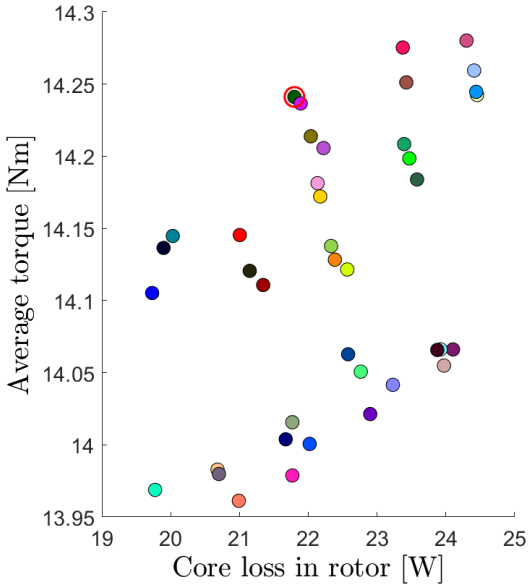

(c) Average torque and rotor core losses.

Figure C.3: Results from the 40 selected geometries with 120 W copper losses in the field windings.

DEPARTMENT OF ELECTRICAL ENGINEERING
CHALMERS UNIVERSITY OF TECHNOLOGY
Gothenburg, Sweden
www.chalmers.se

CHALMERS
UNIVERSITY OF TECHNOLOGY